

1 **Assessing Locations Susceptible to Shallow Landslide Initiation**  
2 **During Prolonged Intense Rainfall in the Lares, Utuado, and**  
3 **Naranjito Municipios of Puerto Rico**  
4

5 Rex L. Baum<sup>1</sup>, Dianne L. Brien<sup>2</sup>, Mark E. Reid<sup>2</sup>, William H. Schulz<sup>1</sup>, and Matthew J. Tello<sup>1,3</sup>

6 <sup>1</sup>U.S. Geological Survey, Golden, Colorado 80401, USA, <sup>2</sup>U.S. Geological Survey, Moffett Field, California 94035,  
7 USA

8 <sup>3</sup>Present Address, Colorado Department of Transportation, Denver, Colorado 80204, USA

9 *Correspondence to:* Rex L. Baum ([baum@usgs.gov](mailto:baum@usgs.gov))

11 **Abstract.** Hurricane María induced about 70,000 landslides throughout Puerto Rico, USA, including thousands each  
12 in three municipalities situated in Puerto Rico's rugged Cordillera Central range. By combining a nonlinear soil-depth  
13 model, presumed wettest-case pore pressures, and quasi-three-dimensional (3D) slope-stability analysis we developed  
14 a landslide susceptibility map that has very good performance and continuous susceptibility zones having smooth,  
15 buffered boundaries. Our landslide susceptibility map enables assessment of (1) potential ground-failure locations,  
16 and (2) ~~areas of potential their use as~~ landslide sources ~~to support in~~ a companion assessment of inundation and debris-  
17 flow runoff. The quasi-3D factor of safety,  $F_3$ , showed strong inverse correlation to landslide density (high density at  
18 low  $F_3$ ). Area under the curve (AUC) of True Positive Rate (TPR) versus False Positive Rate (FPR) indicated success  
19 of  $F_3$  in identifying head-scarp points (AUC=0.84) and source-area polygons ( $0.85 \leq \text{AUC} \leq 0.88$ ). The susceptibility  
20 zones enclose specific percentages of observed landslides. Thus, zone boundaries use successive  $F_3$  levels for  
21 increasing TPR of landslide head-scarp points, with zones bounded by  $F_3$  at TPR=0.75, very high;  $F_3$  at TPR=0.90,  
22 high; and the remainder moderate to low. The very high susceptibility zone, with 118 landslides/km<sup>2</sup>, covered 23% of  
23 the three municipalities. The high zone (51 landslides/km<sup>2</sup>) covered another 10%.

## 24 1 Introduction

25 ~~Heavy rainfall from Hurricane María during September 2017 produced tens of thousands of landslides on the main~~  
26 ~~island of Puerto Rico, USA (Bessette Kirton et al. 2017, 2019a; Hughes et al. 2019). Shallow, translational failures in~~  
27 ~~soil or saprolite, from decimeters to a few meters deep were the most common landslides. Deeper (up to 30 m) complex~~  
28 ~~failures in soil, saprolite, and rock, as well as rock falls and rock slides also occurred (Bessette Kirton et al. 2017).~~  
29 ~~Many landslides transformed into debris flows that commonly coalesced and flowed down channels. Landslides~~  
30 ~~caused fatalities as well as widespread damage to homes, roads, and other infrastructure.~~

31 Landslide susceptibility maps are widely used to mitigate the major hazards landslides pose to people, public and  
32 private property, lifelines, utilities, and businesses. Reliable application of physically based models to landslide  
33 susceptibility assessment has been intensively researched since the 1990s. Many models and computer codes for such  
34 assessments exist (Montgomery and Dietrich, 1994; Wu and Sidle, 1995; Pack et al. 1998; Simoni et al. 2008; Baum  
35 et al. 2010; Arnone et al. 2011; Rossi et al. 2013). Nevertheless, several scientific and technical challenges complicate  
36 the application of these models over large areas. These challenges exist, in part, because many geological,  
37 hydrological, and geotechnical details of the subsurface remain unknowable except at points of direct observation.  
38 Among others, the subsurface knowledge gaps include (1) relationships between soil thickness and shallow landslide  
39 depth, (2) model parameter spatial distribution and variability, (3) pore pressure and effective stress distributions, and  
40 (4) landslide failure modes. Research has made much progress in addressing these knowledge gaps. For example,  
41 many physically based and empirical soil-depth models are available (Roering, 2008; Pelletier and Rasmussen 2009;  
42 Ho et al. 2012; Catani et al. 2010; Nicótina et al. 2011; Gomes et al. 2016; Patton et al. 2018, Yan et al. 2021; Xiao et  
43 al., 2023), making it possible to estimate the field-distribution of soil depth in landslide prone areas (Godt et al. 2008a;  
44 Segoni et al. 2009; Ho et al. 2012). Some studies have combined field or laboratory measured properties with mapped  
45 lithologic characteristics and statistical analysis to describe the spatial distribution of soil properties (Godt et al. 2008b;  
46 Tofani et al. 2017). Many other studies have applied probabilistic approaches successfully to address parameter

47 uncertainty and improve accuracy of physically based modelling of landslide susceptibility (Raia et al. 2014; Zicher  
48 et al. 2017; Canli et al. 2018; Palacio Cordoba et al. 2020; Medina, et al. 2021). Despite these advances, accurate  
49 assessment of landslide susceptibility using physically based methods remains difficult.  
50 Most physically based landslide susceptibility models have relied on the one-dimensional (1D) infinite-slope analysis  
51 to model slope-stability. This approximation is suitable for representing shallow landslides in raster-based topography  
52 where the resolution (grid-cell spacing) is tens of meters. However, applying the 1D analysis to high-resolution (a few  
53 meters or less) topography violates the 1D assumptions of laterally uniform stress and a planar failure surface. A few  
54 spatially distributed three-dimensional (3D) (Mergilli et al. 2014a, 2014b; Reid et al. 2015) and quasi-3D (von Reutte  
55 et al. 2013; Milledge et al. 2015) methods have become available to overcome limitations of the 1D analysis. In the  
56 quasi-3D method of von Reutte et al. (2013) soil columns interact with their neighbors and load is redistributed when  
57 driving forces at the base of a column exceed basal strength. Milledge et al. (2015) used a search algorithm to identify  
58 patches of potentially unstable grid cells by assuming driving forces acting on a group of cells exceed the resisting  
59 forces at the group's margins and that cell groups act as rigid blocks with a failure surface at the soil-bedrock interface.  
60 Mergilli et al. (2014a, 2014b) assumed 3D landslide geometry based on ellipsoidal failure surfaces and used Hovland's  
61 (1977) force-equilibrium method to analyze stability across a digital landscape. Reid et al (2015) used spherical trial  
62 surfaces with moment-equilibrium analysis methods, which tend to be more accurate than methods based on force  
63 equilibrium alone.  
64 In the aftermath of the hurricane, the U.S. Geological Survey (USGS) began working with local partners to conduct  
65 detailed assessments of landslide and debris flow hazards, both island wide (Hughes and Schulz 2020a, b) and more  
66 locally (this study) for three impacted municipalities (Lares Municipio, Utuado Municipio, and Naranjito Municipio)  
67 in the central mountains of Puerto Rico. Here we describe the landslide initiation (source area) part of a landslide  
68 susceptibility assessment for these municipalities. Estimating landslide initiation potential is part of a larger effort (in  
69 progress, Brien et al. 2021) to estimate overall hazard from (1) landslide initiation (ground failure), (2) landslide  
70 runout, and (3) debris-flow inundation from future extreme rainfall, including tropical cyclones (hurricanes), as well  
71 as localized storms expected to impact these areas of Puerto Rico.  
72 One of the main objectives of this work is to produce integrated maps of potential landslide initiation and  
73 inundation areas. Secondary objectives are to integrate soil-depth modeling, consideration of parameter variability,  
74 and quasi-3D slope stability analysis into our assessments. Our approach to soil-depth modeling achieves a good  
75 compromise between swift, simple methods (constant depth or simple empirical methods, such as DeRose et al. 1991)  
76 and the most complicated and computationally intensive (Xiao et al. 2023). Likewise for our quasi-3D slope stability  
77 analysis. Although much progress has been made in methods for assessing landslide susceptibility (e.g., Carrara et al.  
78 1999; Chung and Fabri 2003; Lee et al. 2003; Godt et al. 2008; Baum et al. 2014; Canli et al. 2018) as well as debris-  
79 flow inundation (George and Iverson 2014; Reid et al. 2016; Aaron et al. 2017; Bessette-Kirton et al. 2019b),  
80 combining these two types of assessments into a single map for an area of hundreds of square kilometers remains  
81 challenging (Ellen et al. 1993; Benda et al. 2007; Fan et al. 2017; Hsu and Liu 2019; Mergili et al. 2019). As noted  
82 previously, one of the challenges is estimating potential source-area extent and depth. We addressed this challenge  
83 by modelling soil depth and using it to approximate potential source-area depth in one-dimensional (1D) and quasi-

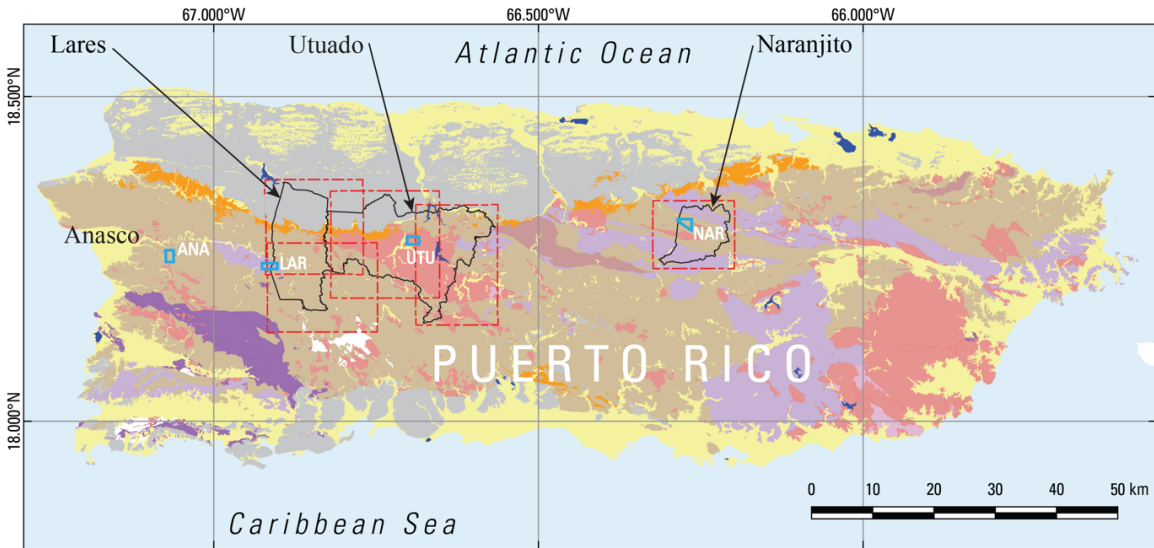
84 ~~three-dimensional (3D)~~ slope stability models for use in assessing regional shallow landslide susceptibility. Such an  
85 approach helps ensure that the susceptibility model accounts for variable failure depth across the landscape and that  
86 predicted areas of potential landslide sources are acceptable for use in assessing debris-flow inundation. We compared  
87 results of several soil-depth models to find the one that performed the best in our study area. The quasi-3D model uses  
88 a simplified limit-equilibrium analysis to estimate the stability of a slab-or goldpan-shaped trial landslide. Another  
89 challenge is establishing meaningful susceptibility categories, which we addressed by delimiting the categories at  
90 quasi-3D factor of safety values,  $F_3$ , that enclose specific percentages of landslide sources, rather than relying on  
91 theoretical or arbitrary factor of safety values to delimit the categories. By showing like outcomes (areas that capture  
92 specific percentages of observed landslides), maps based on this approach are directly comparable to each other.

93 ~~This study was conducted in stages between 2018 and 2022 and involved three study areas as well as calibration areas,~~  
94 ~~study area tiles, and validation areas. We define these here to help the reader comprehend how our presentation of the~~  
95 ~~study is organized. The study areas comprise three municipalities, Lares Municipio, Utuado Municipio, and Naranjito~~  
96 ~~Municipio, and are the focus of our landslide initiation susceptibility maps (Supplemental Figures S1 and S2; Baum~~  
97 ~~et al. 2023). These municipalities were chosen because they were severely impacted by Hurricane María landslides~~  
98 ~~and to help manage their future growth and development. We enclosed the Lares and Utuado study areas in four~~  
99 ~~overlapping rectangles and enclosed Naranjito Municipio in a fifth, separate rectangle (Fig. 1a, 1b, and 1c). The~~  
100 ~~rectangles extend beyond the drainage divides of basins that straddle municipality boundaries. The rectangles delimit~~  
101 ~~overlapping tiles of the digital elevation models (DEM) used in the susceptibility analysis. These DEM tiles helped~~  
102 ~~keep file sizes (6 gigabytes or less for ASCII input and output grids) manageable and overlap ensured that edge effects~~  
103 ~~would not degrade soil depth or slope stability computations. The extended boundaries ensured that landslide runout~~  
104 ~~and debris flow inundation models (Brien et al. in 2021) would not be impeded by municipality boundaries or other~~  
105 ~~artificial barriers. The calibration areas (Fig. 1) were placed in distinct geologic terranes where high concentrations of~~  
106 ~~landslides had occurred. Previous detailed mapping and characterization (Bessette-Kirton et al. 2019c, 2020) and field~~  
107 ~~studies (Baum et al. 2018) in these areas provided data for testing and calibrating soil depth and slope stability models~~  
108 ~~(Tello 2020). From east to west, each 2-km<sup>2</sup> calibration area was named for a nearby city: Añaseo (ANA), Lares~~  
109 ~~(LAR), Utuado (UTU), and Naranjito (NAR). Although ANA is about 15 km west of the study areas, it was included~~  
110 ~~to provide additional calibration data in an area of high landslide density for submarine volcanoclastic lithologies~~  
111 ~~because sufficient data were not available at NAR. Soils, land cover, and other characteristics (besides bedrock~~  
112 ~~lithology) that influence landslide susceptibility vary between the four calibration areas (Bessette-Kirton et al. 2020;~~  
113 ~~Hughes and Schulz 2020a, 2020b). We used six additional areas of detailed mapping (Einbund et al. 2021a, 2021b) to~~  
114 ~~help evaluate the final maps. These validation areas are designated LAR2 and UTU2, and each includes three~~  
115 ~~rectangular areas of detailed landslide mapping (Fig. 1b). We combined detailed source area mapping of NAR~~  
116 ~~(Baxstrom et al. 2021a) and UTU (Einbund et al. 2021a) with that in LAR2 and UTU2 for the validation.~~

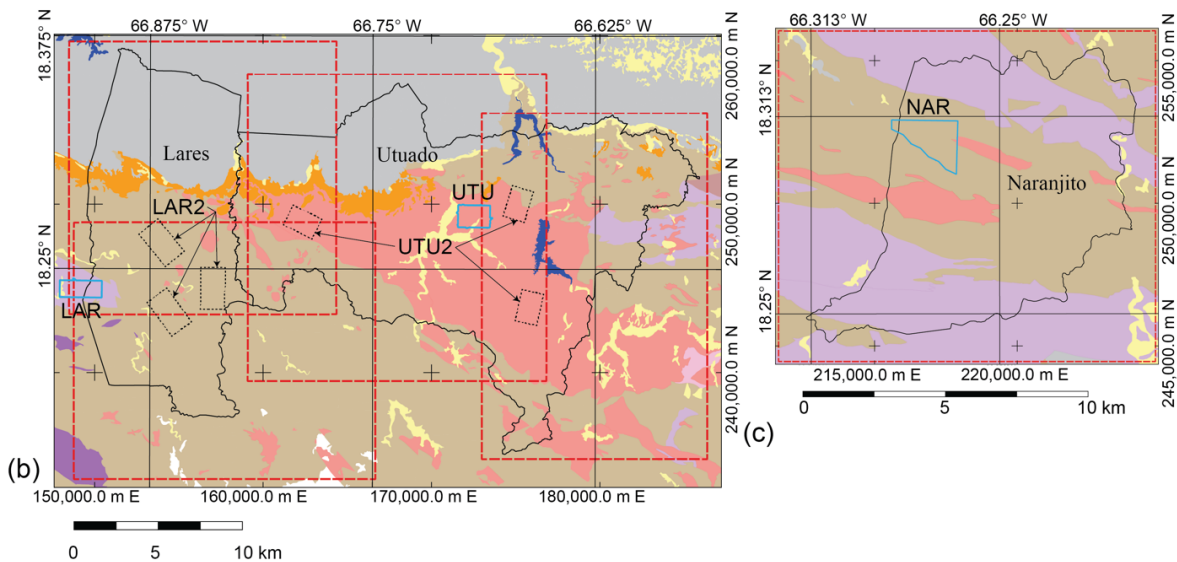
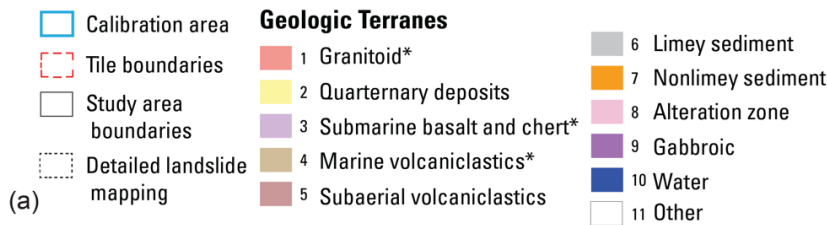
117 In the aftermath of Hurricane María, the U.S. Geological Survey (USGS) began working with local partners to conduct  
118 detailed assessments of landslide and debris-flow hazards, both island-wide (Bessette-Kirton et al. 2017; Hughes and  
119 Schulz 2020a, b) and more locally (this study) for three impacted municipalities (Lares Municipio, Utuado Municipio,  
120 and Naranjito Municipio) in the central mountains of Puerto Rico (Fig. 1). These municipalities were an ideal location

121 for testing and developing methods for such assessments. Here we describe the landslide initiation (source area) part  
122 of a landslide susceptibility assessment for these municipalities. Estimating landslide initiation potential is part of a  
123 larger effort (in progress, Brien et al. 2021) to estimate overall hazard from (1) landslide initiation (ground failure),  
124 (2) landslide runout, and (3) debris-flow inundation from future extreme rainfall, including tropical cyclones  
125 (hurricanes), as well as localized storms expected to impact these areas of Puerto Rico.

126



### Explanation



127

128 **Figure 1. Geologic map showing municipality boundaries, study areas, calibration areas, and major lithologies (geologic**  
 129 **terranes) for the main island of Puerto Rico. Simplified from Bawiec (1998) by combining submarine volcanoclastic rocks**  
 130 **of various ages into a single map unit. Primary landslide-prone lithologies indicated by \* in map explanation. Municipality**  
 131 **boundaries of Lares, Utuado, and Naranjito define study areas. Digital elevation models covering the study areas were**  
 132 **divided into five smaller tiles. Extent of Añasco (ANA), Lares (LAR), Utuado (UTU), and Naranjito (NAR) calibration areas**  
 133 **from [landslide inventories by](#) Bessette-Kirton et al. (2019c, 2020). (a) overview of entire island, (b) details of Lares and**  
 134 **Utuado study areas including outlines of areas of detailed landslide mapping in Utuado, (UTU2, Einbund et al. 2021a) and**  
 135 **Lares (LAR2, Einbund et al. 2021b), (c) details of Naranjito study area.**

136 In the following sections, we describe characteristics of the study areas, summarize our methods and results, and  
137 discuss advantages, limitations, and implications of our approach. First, we describe the setting, geology, and  
138 landslides of Puerto Rico including details specific to the study areas. Then we describe the available topographic and  
139 geotechnical data followed by a description of the workflow for assessing landslide susceptibility. Next, we describe  
140 our methods for modelling soil depth, pressure head, and slope stability along with procedures for model calibration  
141 and details of how the calibrated models were applied to and evaluated for our study areas. Then we present results of  
142 the calibration, soil-depth modelling, 1D and quasi-3D stability analyses, and the evaluation and validation of the  
143 susceptibility analysis. These results were obtained using pre-event light detection and ranging (lidar) bare-earth  
144 digital elevation models (DEM)s (U.S. Geological Survey, 2018; ~~;~~). The DEMs, with uniformly spaced elevation  
145 values, were created from ground returns of lidar point clouds. DEMs are known in some countries as digital terrain  
146 models, a term with two definitions; throughout this paper we use DEM to avoid ambiguity (Heidemann, 2018). ~~we~~  
147 We reran our models using calibrated input parameters and post-event lidar (U.S. Geological Survey 2020a, b, c) to  
148 estimate susceptibility to future landslides. We finish by discussing strengths and limitations of our approach as well  
149 as some unexpected findings and ways to simplify the workflow for application to areas where limited data are  
150 available.

## 151 **2 Study area**

152 Puerto Rico is a U.S. territory and lies at the east end of the Greater Antilles island chain in the Caribbean Sea (Fig.  
153 1). The main island is characterized by rugged topography and covers an area of 8750 km<sup>2</sup>. The study areas and  
154 calibration areas lie in the east–west-trending Cordillera Central range, which spans most of the island. The range  
155 exceeds elevations of 900 m at many places, and its highest peak reaches an elevation of 1340 m. Coastal plains and  
156 broad lowlands ring most of the island. Ongoing tectonic uplift is one of the main factors creating the rugged  
157 topography across the island (Taggart and Joyce 1991). Warm temperatures, high rainfall, and humidity contribute to  
158 deep weathering and widespread saprolite formation (Murphy et al. 2012).

159 This study was conducted in stages between 2018 and 2022 and involved three study areas as well as calibration areas,  
160 study-area tiles, and validation areas. We define these here to help the reader comprehend how our presentation of the  
161 study is organized. The study areas comprise three municipalities, Lares Municipio, Utuado Municipio, and Naranjito  
162 Municipio, and are the focus of our landslide initiation susceptibility maps (Supplemental Figures S1 and S2; Baum  
163 et al. 2023). These municipalities were chosen because they were severely impacted by Hurricane María landslides  
164 and to help manage their future growth and development. We enclosed the Lares and Utuado study areas in four  
165 overlapping rectangles and enclosed Naranjito Municipio in a fifth, separate rectangle (Fig. 1a, 1b, and 1c). The  
166 rectangles extend beyond the drainage divides of basins that straddle municipality boundaries. The rectangles delimit  
167 overlapping tiles of the ~~digital elevation models (DEM)~~ used in the susceptibility analysis. These DEM tiles helped  
168 keep file sizes (6 gigabytes or less for ASCII input and output grids) manageable and overlap ensured that edge effects  
169 would not degrade soil-depth or slope-stability computations. The extended boundaries ensured that landslide runoff  
170 and debris-flow inundation models (Brien et al. ~~in~~ 2021) would not be impeded by municipality boundaries or other  
171 artificial barriers. The calibration areas (Fig. 1) were placed in distinct geologic terranes where high concentrations of

172 landslides had occurred. Previous detailed mapping and characterization (Besette-Kirton et al. 2019c, 2020) and field  
173 studies (Baum et al. 2018) in these areas provided data for testing and calibrating soil-depth and slope-stability models  
174 (Tello 2020). From east to west, each 2-km<sup>2</sup> calibration area was named for a nearby city: Añasco (ANA), Lares  
175 (LAR), Utuado (UTU), and Naranjito (NAR). Although ANA is about 15 km west of the study areas, it was included  
176 to provide additional calibration data in an area of high landslide density for submarine volcanoclastic lithologies  
177 because sufficient data were not available at NAR. Soils, land cover, and other characteristics (besides bedrock  
178 lithology) that influence landslide susceptibility vary between the four calibration areas (Besette-Kirton et al. 2020;  
179 Hughes and Schulz 2020a, 2020b). We used six additional areas of detailed mapping (Einbund et al. 2021a, 2021b) to  
180 help evaluate the final maps. These validation areas are designated LAR2 and UTU2, and each includes three  
181 rectangular areas of detailed landslide mapping. (Fig. 1b). We combined detailed source area mapping of NAR  
182 (Baxstrom et al. 2021a) and UTU (Einbund et al. 2021a) with that in LAR2 and UTU2 for the validation.

183

## 184 **2.1 Geology and soils**

185 Heavily faulted basement rocks, consisting mainly of oceanic crust, volcanoclastic, and intrusive rocks, underlie the  
186 Cordillera Central range (Jolly et al. 1998). A cover sequence of carbonates and associated clastic sediments  
187 unconformably overlies the basement complex. The carbonates have weathered to form tropical karst in the lowlands  
188 north of the range (Monroe 1976). Bawiec (1998) generalized the geology of Puerto Rico into twelve geologic terranes  
189 having related rock types. We have simplified the terranes slightly for purposes of this study (Fig. 1). Soil mapping  
190 and databases published by the U.S. Department of Agriculture's Natural Resources Conservation Service (NRCS)  
191 indicate a wide range in the textures (particle-size distributions) and hydraulic properties of soils in the study areas  
192 (Soil Survey Staff 2018). Most hillside soils have developed by in-place chemical weathering of underlying bedrock  
193 or saprolite and locally derived colluvium. Despite the steep slopes, in many places the upper few meters of bedrock  
194 have weathered to saprolite (e.g., Jibson 1989; Larsen and Torres-Sanchez 1992).

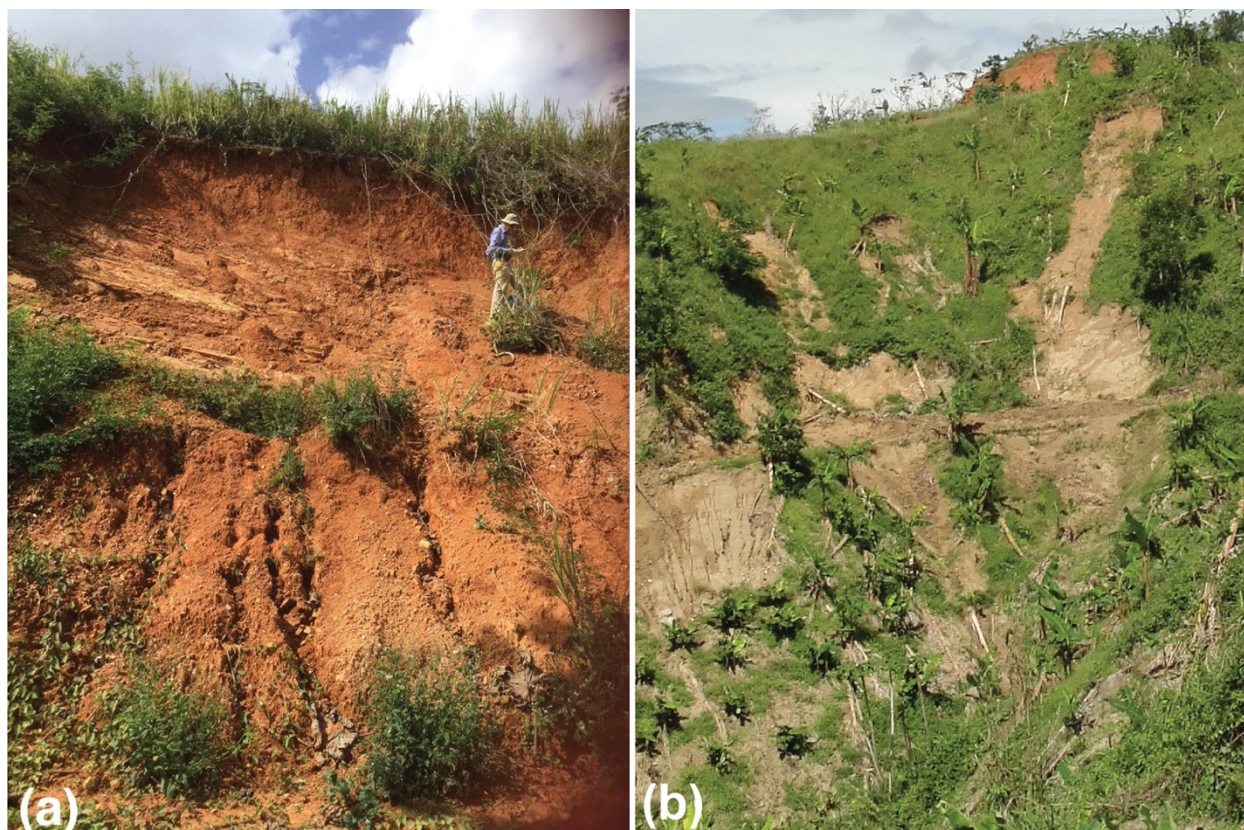
## 195 **2.2 Landslides**

196 Heavy rainfall from Hurricane María during September 2017 produced tens of thousands of landslides on the main  
197 island of Puerto Rico, USA (Besette-Kirton et al. 2017, 2019a; Hughes et al. 2019). Shallow, translational failures in  
198 soil or saprolite, from decimeters to a few meters deep were the most common landslides. Deeper (up to 30 m) complex  
199 failures in soil, saprolite, and rock, as well as rock falls and rock slides also occurred (Besette-Kirton et al. 2017).  
200 Many landslides transformed into debris flows that commonly coalesced and flowed down channels. Landslides  
201 caused fatalities as well as widespread damage to homes, roads, and other infrastructure.

202 Recent and historical studies described and characterized Puerto Rico's rainfall-induced landslides. Published studies  
203 of past landslides characterized rainfall-induced landslides in southern and eastern parts of Puerto Rico (Jibson 1989;  
204 Simon et al. 1990; Larsen and Torres-Sanchez 1992, 1998; Pando et al. 2005; Larsen 2012). Several post-Hurricane  
205 María studies documented dimensional, geologic, and topographic characteristics of landslide sources in ten  
206 representative areas of high landslide density within and near the municipality study areas (Fig. 1): Baum et al. (2018)



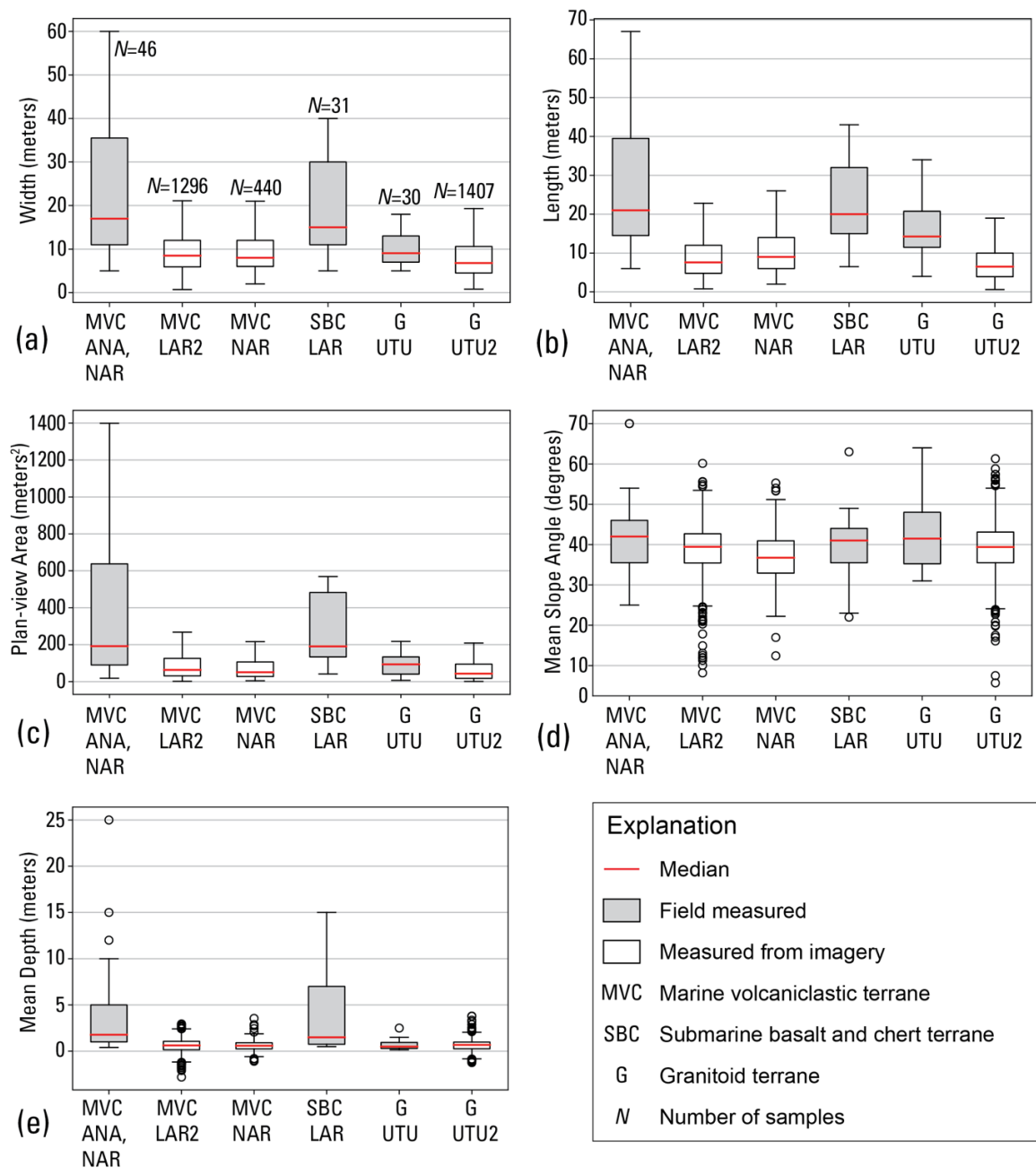
207 conducted field studies and measurements (Fig. 2), and Bessette-Kirton et al. (2019c) later mapped landslides using  
208 post-event aerial photography in the four areas denoted as ANA, LAR, NAR, and UTU (Fig. 1a). U.S. Geological  
209 Survey staff later remapped NAR (Baxstrom et al. 2021a), remapped UTU (Einbund et al. 2021a), and mapped six  
210 additional areas (UTU2 and LAR2, Fig. 1b) near UTU and LAR (Einbund et al. 2021a, 2021b). Schulz et al. (2023)  
211 expanded on earlier field studies of Baum et al. (2018). Data from some of these studies supported recent analyses of  
212 landslide susceptibility (Bessette-Kirton et al. 2019a; Hughes and Schulz 2020a) and runout characteristics (Bessette-  
213 Kirton et al. 2020).



215  
216 **Figure 2. Photographs ~~taken in May 2018~~ depicting source areas of shallow landslides in (a) volcaniclastic terrane**  
217 **(photograph by C. Cerovski-Darriau, U.S. Geological Survey, May 2018, public domain) and (b) granitoid terrane ~~eight~~**  
218 **one months after Hurricane María (photographs by ~~C. Cerovski-Darriau~~W. Schulz, U.S. Geological Survey, October 2017,**  
219 **public domain).**

220 The post-Hurricane María studies cited above indicated that most source areas were fully evacuated, and shallow  
221 translational slides appear to be the most common type of movement prior to transforming to debris flows.  
222 Nevertheless, source area shapes were consistent with translational, rotational, or complex movement. Source areas  
223 exposed soil, saprolite, and bedrock (Fig. 2). Soil matrix textures ranged from sand to clay; clast content increased  
224 with depth. Differences between the landslide source sizes and depths within the different terranes (Fig. 3) seem  
225 consistent with their different lithologies and depth of weathering (volcaniclastic rocks, weathered volcanic rocks,  
226 granitic pluton).

227



228

229 **Figure 3. Box plots summarizing landslide source dimensions obtained for three geologic terranes by field studies of 107**  
 230 **landslides (gray, Baum et al. 2018) and by mapping 3440 landslides from aerial imagery and lidar-derived digital elevation**  
 231 **models (white, Baxstrom 2021a; Einbund 2021a, 2021b). (a) width, (b) length, (c) plan-view area calculated directly by**  
 232 **geographic information system for mapped polygons and estimated from field measurements as an ellipse and projected to**  
 233 **the horizontal,  $\pi \times (\text{Length} \times \text{Width} \times \cos(\text{Slope angle}))/4$ , (d) mean slope angle, (e) mean landslide source depths. Outliers**  
 234 **of width, length and area not shown to keep 25%, 50%, and 75% quartiles legible; box length = interquartile range (IQR),**  
 235 **whiskers = 1.5 x IQR. [Locations (as shown in Fig. 1): ANA, Añasco; LAR, Lares; LAR2, Lares (Einbund et al. 2021b);**  
 236 **UTU, Utuado; UTU2, Utuado (Einbund et al. 2021b, includes UTU); NAR, Naranjito (remapped by Baxstrom et al. 2021a)].**

237 Figure 3 summarizes landslide dimensions obtained from the post-Hurricane María studies for the three main geologic  
 238 terranes in the study areas (Fig. 1). The field measurements (using laser range finder, tape, and clinometer; Baum et  
 239 al. 2018), though biased by purposely including several large landslides (1500 m<sup>2</sup> – 6600 m<sup>2</sup>), represent the range of

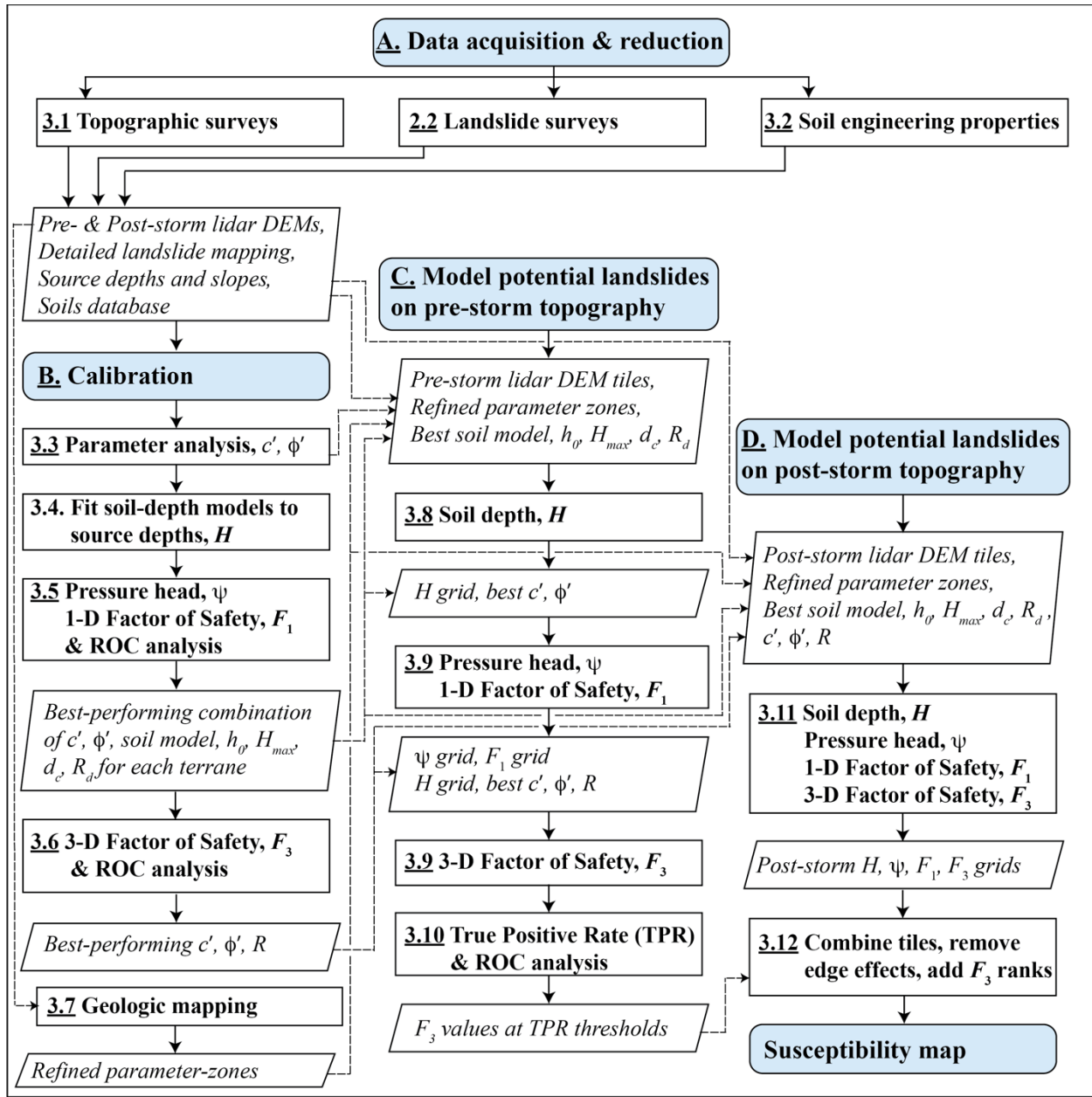
240 sizes of Hurricane María landslide sources. Mapping from imagery (Baxstrom et al. 2021a; Einbund et al. 2021a,  
241 2021b) included all landslides visible in the imagery of several 2.5-km<sup>2</sup> target areas and represent typical dimensions  
242 of landslides triggered by the hurricane on uplands and valley side slopes. Most landslide sources had lengths and  
243 widths less than 10-15 m, with median mapped length and width among the different samples in Figure 3a, 3b ranging  
244 from 6.5 m to 9 m. Many landslide sources have areas less than 100 m<sup>2</sup> (median mapped areas range from 42 m<sup>2</sup> to  
245 64 m<sup>2</sup> for the different terranes), and very few have areas greater than 1000 m<sup>2</sup> (Fig. 3c). Although landslides occurred  
246 on a wide range of slope angles, most occurred on slopes between 30° and 50° (Fig. 3d). Median DEM-derived mean  
247 slope angles of mapped landslide sources were 37° - 39° (Fig. 3d). Depths computed by differencing pre-event and  
248 post-event lidar elevation data (Baxstrom et al. 2021a; Einbund et al. 2021a, 2021b) have significant uncertainty  
249 because 14 – 19% of the landslide sources had mean and median elevation differences indicating net gain of material  
250 (Fig. 3e). In addition, undisturbed areas outside the landslide polygons showed elevation differences that varied  
251 horizontally, ~~which is~~ consistent with alignment errors between inadequate swath adjustment in the pre- and post-event  
252 lidar point clouds. Data needed to correct the resulting mismatch between pre- and post-event lidar were unavailable.  
253 However, it seems unlikely that any of the mapped landslides had a mean depth much greater than 5.8 m (the span  
254 between the greatest elevation loss and gain, MVC/LAR2, Fig. 3e). Rare, large landslides had depths as great as 25 m  
255 according to field measurements (Fig. 3e).

256 Puerto Rico's complex geology (Fig. 1), tropical soils, rugged terrain, land use, and landcover exert strong influences  
257 on landslide susceptibility. Lepore et al. (2012) in an island-wide assessment using frequency ratio and logistic  
258 regression concluded that aspect, slope, elevation, geological discontinuities, and geology, were “highly significant  
259 landslide-inducing factors”; land cover and distance from roads were also significant. Bessette-Kirton et al. (2019a)  
260 showed that antecedent soil moisture was statistically correlated to densities of Hurricane-María-induced landslides  
261 and found that high landslide densities were “especially widespread across some geologic formations,” although the  
262 degree to which rainfall characteristics resulted in this correlation remained unclear. In a later post-Hurricane María,  
263 island-wide assessment using the frequency ratio method, Hughes and Schulz (2020a) found after accounting for the  
264 effects of soil moisture, there were strong correlations between landslides and slope, curvature, geologic terrane, mean  
265 annual precipitation, land cover, soil type, event soil moisture, proximity to roads, and proximity to fluvial channels  
266 for the Hurricane María event. Previous, more localized studies considered fewer geomorphic and geographic  
267 characteristics to classify landslide susceptibility using empirical and statistical methods (Larsen and Parks 1998;  
268 Larsen et al. 2004). For example, Larsen and Parks (1998) classified landslide susceptibility of Comerío Municipality  
269 based on elevation, slope, aspect, and land use. Our current study uses physics based geotechnical models of slope  
270 stability to directly assess topographic, geologic, and soil controls on landslide potential and to indirectly assess effects  
271 of roads and land use through their impacts on topography and surface drainage as expressed in the DEM as local  
272 changes in the slope characteristics.

### 273 **3 Methods and materials**

274 To represent the aerial extent and depths of potential landslide source areas, we undertook a multistage process to  
275 acquire data, characterize the landslides, calibrate parameters, and model potential landslide sources for both pre-

276 Hurricane María and post-Hurricane María digital topography. In Figure 4, bold capital letters mark the four main  
277 stages of the study: (A) Data acquisition and reduction, (B) Calibration, (C) Susceptibility modeling on pre-storm  
278 topography, and (D) Susceptibility modeling on post-storm topography. Each stage comprises multiple steps; numbers  
279 in Fig. 4 identify the section describing each major step. Most results of Stage A were published previously, but are  
280 described briefly in sections 2.2, 3.1, and 3.2 to provide context for this study. Stages B, C, and D (Fig. 4) repeated  
281 four distinct modelling tasks: (1) soil depth,  $H$ , (2) pressure head,  $\psi$ , (3) 1D factor of safety,  $F_1$ , (4) quasi-3D factor  
282 of safety,  $F_3$ . The landscapes of the calibration and study areas were represented digitally in the models as raster grids  
283 based on 1-m-resolution pre-event lidar-derived DEMs. Each grid cell represented a column of potential landslide  
284 material of vertical depth,  $H$ , determined at soil-depth modelling steps of stages B, C, and D (Fig. 4). Computed soil  
285 depth from these steps became input for calculation of  $\psi$ , (Fig. 4); then  $H$  and  $\psi$  became inputs for computing  $F_1$  (Fig.  
286 4) and  $F_3$ .  $F_1$  was used primarily in evaluating soil-depth models and shear-strength parameters for the calibration  
287 areas depicted in Fig. 1 using receiver operating characteristic (ROC, Metz, 1978) analysis (Fig. 4). During post-  
288 calibration slope-stability modelling of the study areas,  $F_1$  served as a rough check on the computed value of  $F_3$ . The  
289 following sections outline the major steps depicted in Figure 4.



290

291 **Figure 4. Flow chart showing four major stages (enumerated by capital letters A, B, C, D) and steps of data acquisition,**  
 292 **calibration and modelling leading to the map of landslide initiation susceptibility (Susceptibility map, bottom of right**  
 293 **column). Numbers (underlined, bold) identify the corresponding sections where the steps and their outputs are described.**  
 294 **The data acquisition stage (A, top) was performed at scales ranging from island-wide to site specific. The calibration stage**  
 295 **(B, left column) was performed using digital elevation models of roughly 2.5-km<sup>2</sup> areas where detailed mapping and**  
 296 **fieldwork had been conducted (Fig. 1). Landslide source depths approximated soil depth for soil-depth model calibration.**  
 297 **The pre-Hurricane María (pre-storm) modeling stage (C, center column) was conducted using overlapping DEM tiles (Fig.**  
 298 **1) derived from pre-Hurricane María lidar data (U.S. Geological Survey, 2018). The post-Hurricane María (post-storm)**  
 299 **modeling stage (for generating map of future landslide susceptibility, D, right column) used overlapping DEM tiles (Fig. 1)**  
 300 **derived from post-Hurricane María lidar data (U.S. Geological Survey, 2020a, b, c). Post-Hurricane María steps used**  
 301 **identical input parameters to the corresponding pre-Hurricane María steps. [Chart symbols: Light-blue rounded**  
 302 **rectangles, terminals of each major stage; rectangles with bold text, technical or computational processes; parallelograms**  
 303 **with italic text, inputs or outputs; dashed lines, connections between outputs and model inputs. Model outputs:  $H$ , soil**  
 304 **depth;  $\psi$ , pressure head;  $F_1$ , 1D factor of safety;  $F_3$ , quasi-3D factor of safety; TPR, true positive rate; ROC, Receiver**  
 305 **Operating Characteristics. Model input parameters:  $h_0$ , characteristic soil depth,  $H_{max}$ , maximum soil depth;  $\delta_c$ , critical**

306 slope angle;  $R_d$ , diffusivity ratio;  $c'$ , cohesion for effective stress;  $\phi'$ , angle of internal friction for effective stress;  $R$ , radius  
307 of quasi-3D trial surface.]

### 309 **3.1 Topographic surveys and data**

310 In 2015 and 2016, the U.S. Geological Survey (2018) acquired airborne lidar covering the entire main island of Puerto  
311 Rico. These data were processed to create a 1-m resolution bare-earth DEM. Referred to hereafter as pre-event lidar,  
312 these data were acquired roughly one to two years before Hurricane María and constitute the best available  
313 representation of topographic conditions before the landslides associated with the hurricane occurred. Available at the  
314 beginning of our investigation, the pre-event lidar-derived DEMs have formed the topographic mainstay for U.S.  
315 Geological Survey studies of these recent landslides. We used these data for calibration and validation of our soil  
316 depth and slope stability models. After Hurricane María, the U.S. Geological Survey (2020a, b, c) acquired additional  
317 lidar data covering the entire island in 2018. These data, referred to hereafter as post-event lidar, constitute the  
318 (currently) best available representation of topographic conditions after the landslides and are useful for assessing  
319 susceptibility to future landslides. The 0.5-m post-event lidar DEMs were resampled to 1-m resolution for consistency  
320 with the pre-event lidar DEMs and computational efficiency of landslide susceptibility models. We used these post-  
321 event DEMs to run our models (using the previously calibrated and evaluated input parameters) to obtain our best  
322 estimate of susceptibility to future landslides.

### 323 **3.2 Engineering Data compilation**

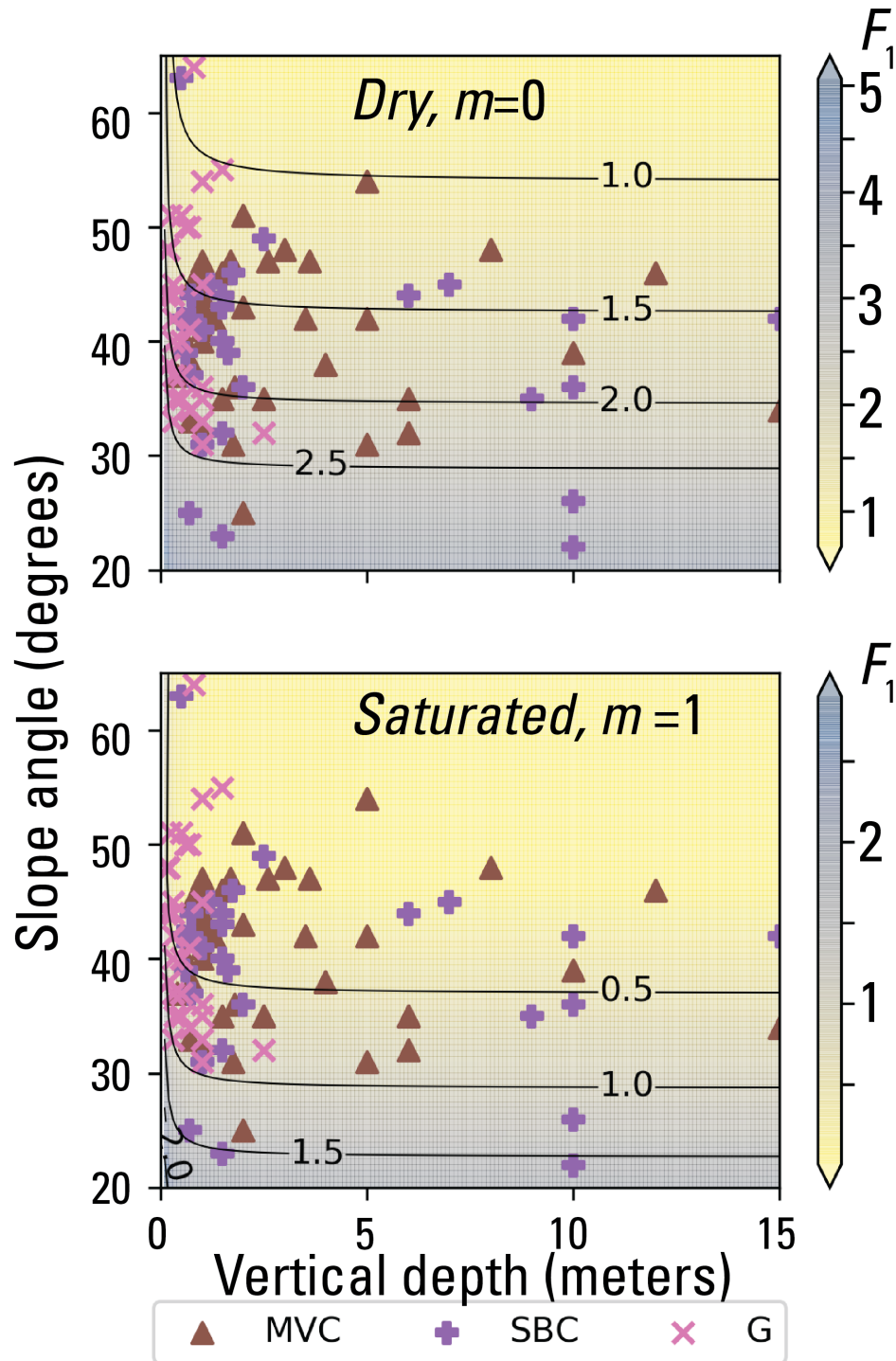
324 Based on findings by Bessette-Kirton et al. (2019a) and Hughes and Schulz (2020a, b) indicating strong correlation  
325 between landslide density and both bedrock and soil type, Baum (2021) compiled existing data on soil texture and  
326 engineering properties to create typical values for model calibration. Four different sources yielded soil and (or)  
327 engineering data: (1) published literature about past and recent landslides in Puerto Rico (Sowers 1971; Jibson 1989;  
328 Simon et al. 1990; Larsen and Torres-Sanchez 1992, 1998; Lepore et al. 2013; Thomas and Cerovski-Darriau 2019),  
329 (2) NRCS soil databases (Soil Survey Staff; 2018), (3) laboratory testing (Smith et al. 2020), and (4) geotechnical  
330 reports of recent landslides (Puerto Rico Department of Transportation, written commun. 2019). The NRCS soil data  
331 and geotechnical reports were summarized in spreadsheets and then analyzed to determine means, ranges, and other  
332 basic statistics to characterize the properties of soils and geologic formations found throughout the three municipalities  
333 (Baum and Lewis, 2023). The database compiled from these sources and measured using various protocols, though  
334 inhomogeneous, brackets the probable ranges of engineering properties. Baum (2021) identified dominant soil classes  
335 of the geologic terranes that had high landslide densities (Fig. 1) and estimated expected ranges of soil strength  
336 parameters, cohesion,  $c'$ , and angle of internal friction,  $\phi'$ , both for effective stress based on dominant Unified Soil  
337 Classification System (ASTM International, 2020) types in each terrane as follows: volcanoclastic, high-plasticity  
338 organic clay (OH),  $\phi'$  17° – 35°,  $c'$  5 – 20 kPa; submarine basalt and chert, low plasticity clay (CL) and high-plasticity  
339 silt (MH),  $\phi'$  27° – 35°,  $c'$  5 – 20 kPa; granitoid, low plasticity clay (CL) and silty sand (SM),  $\phi'$  27° – 41°,  $c'$  0 – 20  
340 kPa. Laboratory tests at low normal stress (Smith et al. 2020), relevant to shallow landslides, indicate higher friction

341 ranges: volcanoclastic, high-plasticity silt (MH) to organic clay (OH),  $\phi'$  35° – 46°,  $c'$  0 – 5.1 kPa; granitoid silty sand,  
342  $\phi'$  35° – 54°,  $c'$  0.4 – 4.6 kPa.

### 343 3.3 Strength parameter analysis

344 Using 1D slope stability analysis, Baum (2021) estimated the ranges of soil strength parameters  $\phi'$  and  $c'$  that explain  
345 the largest number of field-observed landslide slope and depth combinations in the calibration areas (Fig. 45).  
346 Computing 1D factor of safety using the infinite slope analysis (Taylor, 1948; Iverson, 2000),  $F_1$ , for 1440 possible  
347 incremental combinations of  $\phi'$  and  $c'$  over a synthetic grid in which slope angle,  $\delta$ , and landslide depth,  $H$ , varied  
348 incrementally over the observed ranges of slope (22° – 60°, in 0.5° increments) and depth (0.2 m – 15 m, in 0.1-m  
349 increments) produced  $F_1$  values for more than  $1.9 \times 10^7$  combinations of  $H$ ,  $\delta$ ,  $\phi'$ , and  $c'$ . The best fitting ranges (dark  
350 red in Fig. 65) included combinations of  $H$ ,  $\delta$ ,  $\phi'$ , and  $c'$ , where more than 75% of observed landslide scarp points  
351 were successfully predicted by  $F_1 \geq 1$  for  $\psi=0$  (dry, where  $\psi$  is the pressure head at the basal slip surface) and  $F_1 < 1$   
352 for  $\psi=H\cos^2\delta$  (water table at the ground surface with slope-parallel flow). The example depicted in Fig. 4-5 had an  
353 overall success rate of 93% for its  $c'$  –  $\phi'$  combination ( $c' = 0.75$  kPa -and  $\phi' = 54^\circ$  ) in all three geologic terranes (Figs.  
354 1, 5a). Compiling the performance of every  $c'$ - $\phi'$  pair considered in the analysis led to Fig. 65b, 5e6c, and 5d6d, which  
355 showed the better-performing ranges of  $c'$  and  $\phi'$  for the granitoid (Fig. 5b6b), volcanoclastic (Fig. 5e6c), and  
356 submarine basalt and chert (Fig. 5d6d) terranes, respectively. Those combinations of  $c'$  and  $\phi'$  with success rates  
357 exceeding 75%, were used as inputs for computing  $F_1$  with trial soil-depth maps in subsequent calibration studies to  
358 select a single combination of  $c'$  and  $\phi'$  for computing  $F_1$  in each terrane.

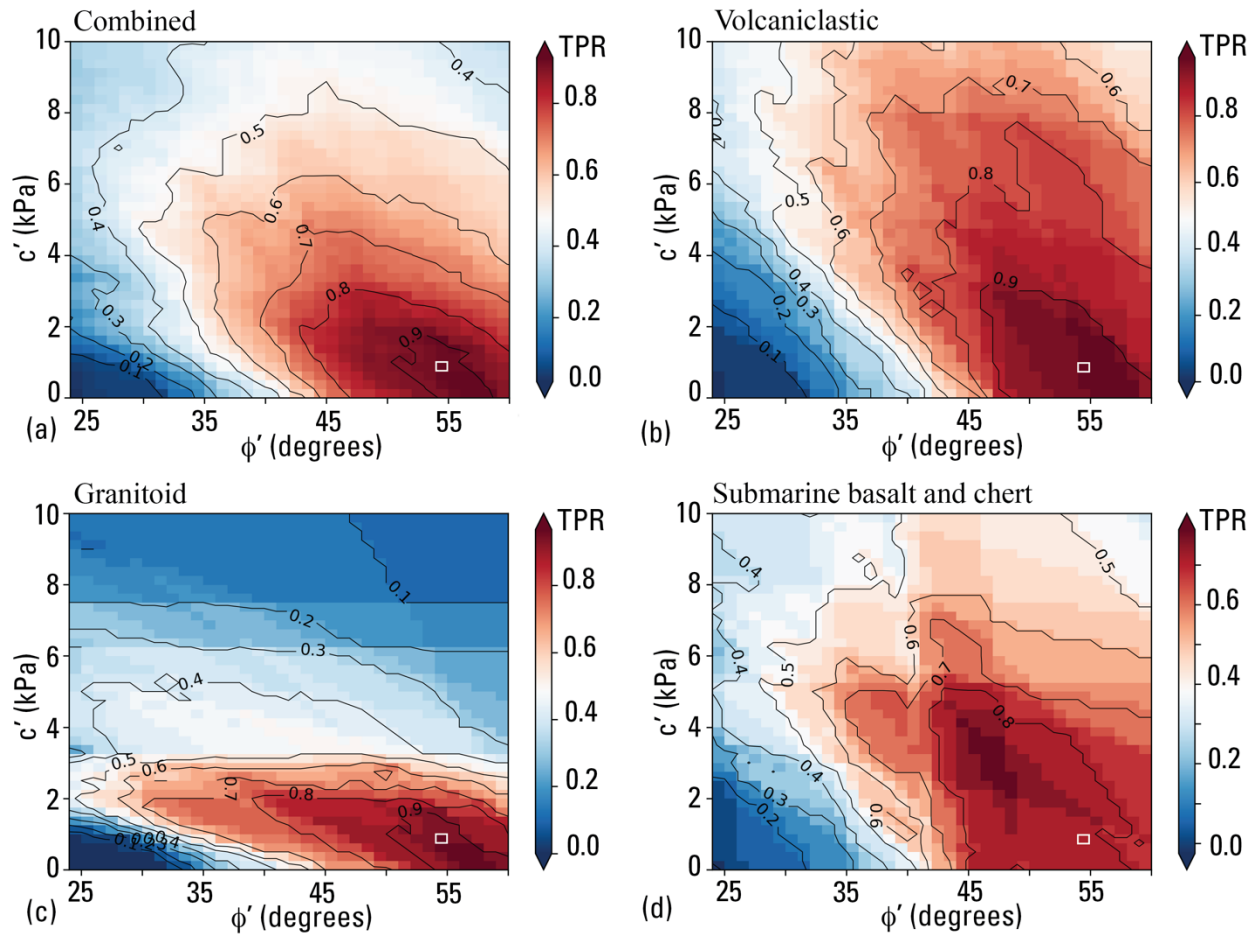
359



360

361 Figure 54. Results of strength parameter testing for observed combinations of landslide slope and depth in three geologic  
 362 terranes. Factor of safety,  $F_1$ , results (indicated by color scale and contour lines) for a selected combination of cohesion,  
 363  $c'$  ( $c' = 0.75$  kPa) and angle of internal friction,  $\phi'$  ( $\phi' = 54^\circ$ ), both for effective stress. Two scenarios for pore-pressure head  
 364 ( $m=0$  and  $m=1$ ) are shown, where  $m$  is the ratio of pressure head to soil depth. Symbols mark observed slope angle and  
 365 depth at mapped landslide sources in various geologic terranes (Fig. 1). Factor of safety,  $F_1$ , at slope and depth combinations  
 366 observed at marked landslide sources indicates model success ( $F_1 < 1$  if  $m=1$ ) or failure ( $F_1 > 1$  if  $m=1$ ). For the pair of  $c'$  and  
 367  $\phi'$  values shown,  $F_1 > 1$  for dry conditions ( $m=0$ ) at about 97% of sources and  $F_1 > 1$  at 4% of sources for water table at the  
 368 ground surface with flow parallel to the slope ( $m=1$ ). These parameters,  $c' = 0.75$  kPa and  $\phi' = 54^\circ$ , had an overall success  
 369 rate of about 93% (=97% - 4%) for all three terranes (revised from Baum 2021).





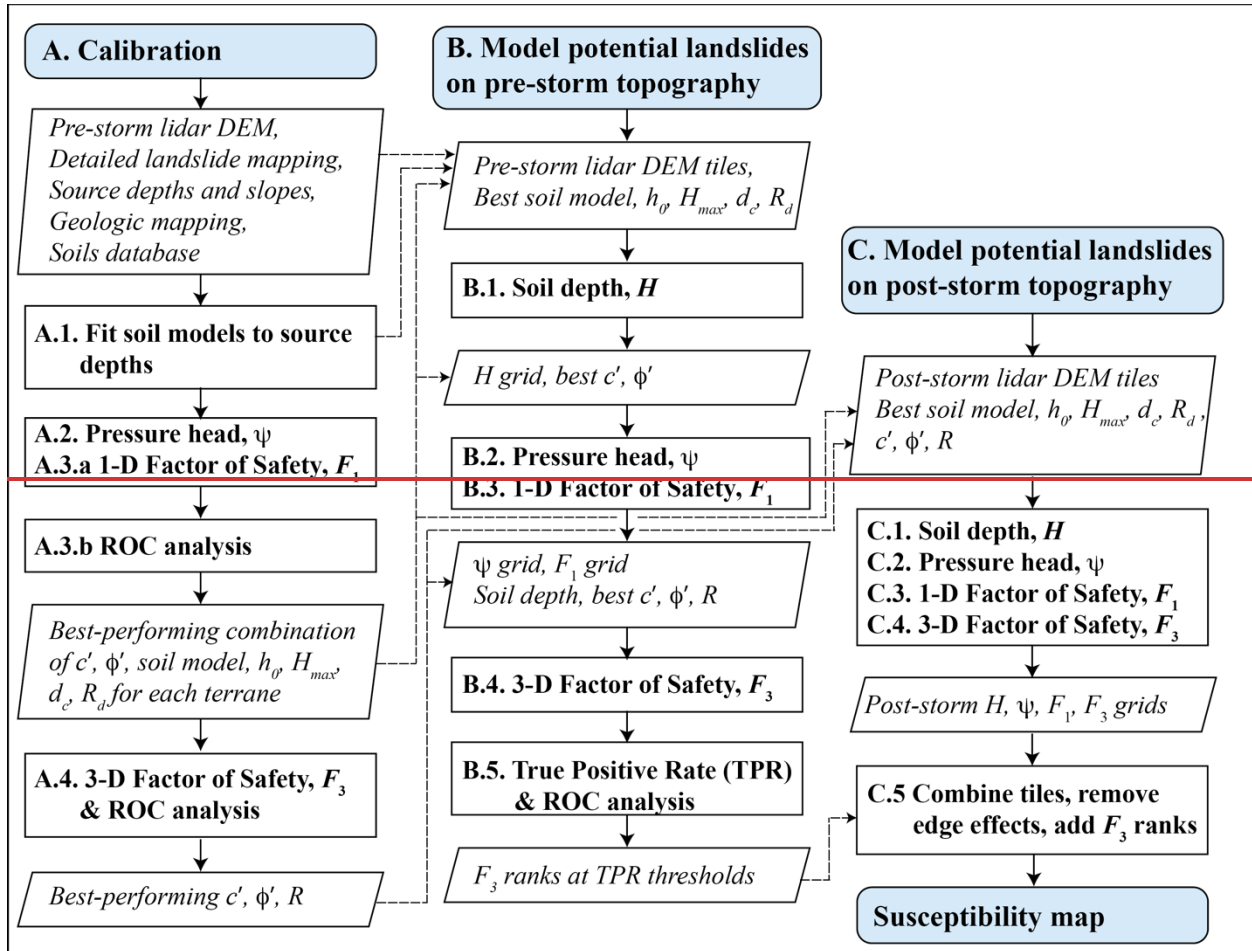
371  
 372 **Figure 56.** Fraction of field-measured landslide sources from the calibration areas (Baum et al. 2018) predicted correctly  
 373 as a function of cohesion,  $c'$ , and angle of internal friction,  $\phi'$ , for observed landslides in (a) all three terranes combined  
 374 (modified from Baum 2021); (b) the volcaniclastic terrane; (c) the granitoid terrane; (d) the submarine basalt and chert  
 375 terrane. Each pixel summarizes the net result of a pair of analyses like that in Figure 54. Pixel outlined by white rectangle  
 376 in lower right corner of panels (a), (b), (c), and (d) indicates combination for analysis shown in Figure 45. Pixel color and  
 377 contours indicate true positive rate (TPR) of predictions for each cell. Factor of safety for dry conditions is  $F_{1m=0}$ ; factor of  
 378 safety for water table at ground surface with slope-parallel flow is  $F_{1m=1}$ . Each grid cell represents the fraction  $(NF_{1m=0} -$   
 379  $NF_{1m=1})/N_i$ , where  $NF_{1m=0}$  is the number of source areas for  $F_1 \geq 1$ ,  $NF_{1m=1}$  is the number of source areas for which  $F_1 \geq 1$ ,  
 380 and  $N_i$  is the number of source areas in the geologic terrane.

381

### 382 3.4 Workflow for shallow landslide susceptibility models

383 To represent the aerial extent and depths of potential landslide source areas, we undertook a multistage process to  
 384 calibrate and model potential landslide sources for both pre-Hurricane María and post-Hurricane María digital  
 385 topography (Fig. 6). Each stage (depicted as a column in Fig. 6) repeated four distinct modelling steps: (1) soil depth,  
 386  $H$ , (2) pressure head,  $\psi$ , (3) 1D factor of safety,  $F_1$ , (4) quasi-3D factor of safety,  $F_3$ . The landscapes of the calibration  
 387 and study areas were represented digitally in the models as raster grids based on 1-m-resolution pre-event lidar-derived  
 388 DEMs. Each grid-cell represented a column of potential landslide material of vertical depth,  $H$ , determined at soil-  
 389 depth modelling steps A.1, B.1, and C.1 (Fig. 6). Computed soil depth from these steps became input for calculation

390 of  $\psi$ , (steps A.2, B.2, and C.2, respectively, Fig. 6); then  $H$  and  $\psi$  became inputs for computing  $F_1$  (steps A.3.a, B.3,  
 391 and C.3, Fig. 6) and  $F_3$  (steps A.4, B.4, and C.4, Fig. 6).  $F_1$  was used primarily in evaluating soil depth models and  
 392 shear strength parameters for the calibration areas depicted in Fig. 1 using receiver operating characteristic (ROC)  
 393 analysis (step A.3.b, Fig. 6). During post-calibration slope stability modelling of the study areas (steps B.4 and C.4,  
 394 Fig. 6),  $F_1$  served as a rough check on the computed value of  $F_3$ . In this section (Sect. 3.4.1, 3.4.2, 3.4.3, and 3.4.4),  
 395 we briefly describe the modelling steps and give details about the models. We describe the major stages (columns in  
 396 Fig. 6) of calibration, modelling, and validation in later sections (Sect. 3.5, ..., 3.11).  
 397



398  
 399 **Figure 6. Flow chart showing major stages (each column) and steps of calibration and modeling leading to the map of**  
 400 **landslide initiation susceptibility (Susceptibility map, bottom of right column). The calibration stage (left column) was**  
 401 **performed using digital elevation models of roughly 2.5 km<sup>2</sup> areas where detailed mapping and fieldwork had been**  
 402 **conducted (Fig. 1). Landslide source depths approximated soil depth for soil depth model calibration (1.1). The pre-**  
 403 **Hurricane Maria (pre-storm) modeling stage (center column) was conducted using overlapping DEM tiles (Fig. 1) derived**  
 404 **from pre-Hurricane Maria lidar (U.S. Geological Survey, 2018). The post-Hurricane Maria (post-storm) modeling stage**  
 405 **(for generating map of future landslide susceptibility, right column) used overlapping DEM tiles (Fig. 1) derived from post-**  
 406 **Hurricane Maria lidar (U.S. Geological Survey, 2020a, b, c). Post-Hurricane Maria steps 3.1, 3.2, 3.3, and 3.4 used identical**  
 407 **input parameters to the corresponding pre-Hurricane Maria steps, 2.1, 2.2, 2.3, and 2.4. [Chart symbols: Light blue**  
 408 **rounded rectangles, terminals of each major stage; rectangles with bold text, computational processes; parallelograms with**  
 409 **italic text, inputs or outputs; dashed lines, connections between calibration outputs and model inputs. Model outputs:  $H$ ,**  
 410 **soil depth;  $\psi$ , pressure head;  $F_1$ , 1D factor of safety;  $F_3$ , quasi-3D factor of safety; TPR, true positive rate; ROC, Receiver**  
 411 **Operating Characteristics. Model input parameters:  $h_0$ , characteristic soil depth,  $H_{max}$ , maximum soil depth;  $\delta_{cs}$ , critical**

412 slope angle;  $R_d$ , diffusivity ratio;  $c'$ , cohesion for effective stress;  $\phi'$ , angle of internal friction for effective stress;  $R$ , radius  
413 of quasi-3D trial surface.]

#### 415 **3.4.1 Step 1, modelling soil depth**

416 Estimating soil depth from a DEM was the first modelling step in all three stages (Fig. 6). Field observations indicated  
417 that the base of most landslide sources occurred near the top of weathered bedrock (Baum et al. 2018; Baum 2021),  
418 so we chose soil depth as a predictor of landslide source depth. We carried out soil depth estimation using new open-  
419 source software, REGOLITH (Baum et al. 2021) containing five empirical and four steady state process based soil-  
420 depth models implemented in a command line program. Each model in REGOLITH estimates soil depth from some  
421 combination of topographic variables, including slope, upslope contributing area, and curvature, as well as a few  
422 model parameters, such as characteristic depth (the soil thickness at which bedrock lowering falls to  $1/e$  of its  
423 maximum value),  $h_0$  [L]; critical slope (angle of stability at which the slope is capable of transporting the entire soil  
424 profile by mass movement),  $\delta_c$  [degrees]; and the ratio of maximum bedrock lowering rate to hillslope diffusivity,  $R_d$ .  
425 These parameters may vary with conditions that influence soil formation, including bedrock and climate. Predicted  
426 soil depth is treated as equivalent to and defines column height,  $H$ , in subsequent modelling steps. We used separate  
427 property zones with distinct parameters in REGOLITH to model adjoining areas of significantly different soil depth  
428 characteristics (tropical karst versus granitoid and volcanoclastic). We modified steady state process based models  
429 (Pelletier and Rasmussen 2009), which predict soil depth only on convex topography, to estimate soil depths in both  
430 concave and convex topography. We used a smoothing algorithm available in REGOLITH to reduce abrupt changes  
431 in soil depth that may result from DEM roughness. Further details are available in the online documentation found in  
432 the code repository (Baum et al. 2021). Our soil depth, pressure head, and slope stability models treated roads, cut  
433 slopes and embankments the same as other areas.

#### 434 **3.4.2 Step 2, modelling subsurface pressure head**

435 Step 2 was performed using the Transient Rainfall Infiltration and Grid Based Regional Slope Stability Analysis  
436 (TRIGRS) program (Baum et al. 2010; Alvioli and Baum 2016), version 2.1. In most applications, TRIGRS computes  
437 pressure head and factor of safety distributed over a digital landscape to yield a series of grids representing changes  
438 in pressure head and factor of safety through time during a rainfall event. For this work, our objective was a landslide  
439 susceptibility map that shows where landslides induced by intense rainfall are most likely, so we used a presumed  
440 wettest case pressure head, rather than simulating time varying pressure head. This approach greatly accelerated the  
441 Step 2 pressure head computations and eliminated the need to calibrate soil hydraulic parameters. Given the extreme  
442 rainfall during Hurricane María and other historical tropical storms, full saturation with the water table at the ground  
443 surface and groundwater flow sub-parallel to the ground surface (as determined by the permeability contrast at the  
444 soil saprolite or soil bedrock boundary) represented the likely wettest case hydrologic conditions for landslide  
445 initiation. This approach neglects effects of suction stress, heterogeneity, and transient pore pressures at the cost of

446 making the susceptibility map more conservative (more false positives). Thus, for this assessment we estimated  
 447 pressure head for these conditions using the following steady-state formula (Iverson 2000; Baum et al. 2010):

$$449 \psi(Z) = (Z - d) \left[ (\cos \delta)^2 - \frac{I_{ZLT}}{K_s} \right] \quad (1)$$

450  
 451 In Eq. (1),  $\psi(Z)$  [L] is the pressure head as a function of  $Z$  [L], the vertical coordinate direction (positive downward  
 452 from the ground surface);  $d$  [L] is the steady-state depth to the water table measured in the vertical direction (0 m in  
 453 this case);  $I_{ZLT}$  [ $LT^{-1}$ ] is the steady background flux;  $\delta$  is the slope angle; and  $K_s$  [ $LT^{-1}$ ] is the saturated hydraulic  
 454 conductivity. The dimensionless ratio  $I_{ZLT}/K_s$  in Eq. (1) accounts for downward percolation and reduces the pressure  
 455 head from the slope parallel case represented by  $H \cos^2 \delta$ , where  $H$  ( $=Z - d$ ) is the column height as noted previously.  
 456 The average rate of downward percolation is strongly controlled by the permeability contrast between the mobile  
 457 regolith (soil mantle) and underlying weathered bedrock or saprolite. For the problem considered here,  $I_{ZLT}/K_s = 0.028$ ,  
 458 consistent with wet initial conditions (averaging 2–25 mm/day of precipitation induced infiltration,  $I_{ZLT}$ , for  $K_s$  in the  
 459 range  $10^{-5}$ – $10^{-6}$  m/s, typical of soils in the study area). This value of  $I_{ZLT}/K_s$  directs flow slightly downward and  
 460 reduces the pressure head by less than 1% compared to slope parallel flow in the  $25^\circ$ – $55^\circ$  range of slopes where most  
 461 landslides occurred. TRIGRS computes  $\psi(Z)$  for a series of equally spaced depths between the ground surface ( $Z=0$ )  
 462 and a user-specified maximum depth,  $Z=Z_{max}$ . For this analysis,  $Z_{max} = H$  as determined by the soil depth modeled in  
 463 stage A and we used a depth increment of  $Z_{max}/10$ .

### 464 3.4.3 Step 3, 1D factor of safety

465 TRIGRS computes the 1D factor of safety,  $F_1$ , using the infinite slope analysis (Taylor 1948; Iverson 2000) according  
 466 to the following formula for the saturated case:

$$468 F_1 = \frac{\tan \phi_s}{\tan \delta} + \frac{c' - \psi(Z) \gamma_w \tan \phi_s}{Z \gamma_s \sin \delta \cos \delta} \quad (2)$$

469  
 470 In Eq. (2)  $\gamma_s$  is the saturated unit weight of soil;  $\gamma_w$  is the unit weight of water; and  $\delta$  is the true dip of the slip surface  
 471 at the base of mobile regolith (assumed parallel to the slope of the ground surface in the infinite slope analysis).  
 472 TRIGRS computes  $F_1$  at the same series of depths between the ground surface and modeled soil depth as for  $\psi(Z)$ .  
 473 Eq. (2) is strictly valid for landslides much longer than their depth on planar slopes in which lateral variation in stress  
 474 is negligible. With the advent of high-resolution topography, the depth-to-length ratios of soil columns at most grid  
 475 cells have become much greater than 0.1, such that the small depth-to-length landslide assumption of Eq. (2) is  
 476 violated. This violation reduces accuracy for nonplanar slopes and for rough DEMs (whether the roughness results  
 477 from natural surface roughness or from data collection and processing errors). A slope stability analysis that considers  
 478 multiple adjacent DEM cells can improve accuracy for nonplanar slopes and rough DEMs.

#### 3.4.4 Step 4, 3D factor of safety

To overcome the limitations of  $F_1$  for high-resolution topography and to assess the stability of potential source areas similar in size to past landslides, the computed pressure head, Eq. (2), was used in a separate computer program, Slabs3D (Baum 2023), to compute the quasi-3D factor of safety,  $F_3$ . Baum et al. (2012) described and tested a preliminary version of the program, which recently was further developed and tested for the work reported here. Slabs3D was designed to rapidly analyze stability of the soil mantle on hillsides to identify potential shallow landslide sources. By using a method of columns, Slabs3D overcomes some of the limitations of infinite slope computations on high-resolution topography. However, the current version of Slabs3D relies on force equilibrium alone (not moment equilibrium). Thus, the approximations made in computing  $F_3$  are suitable only for thin (disc- or slab-shaped) landslides, such as most landslides in the study areas (Figs. 2, 3). Potential landslides can be more thoroughly analyzed with 3D slope stability software such as Scoops3D, which considers moment equilibrium on arcuate trial surfaces (Reid et al. 2015). However, in consideration of the thin, slab-shaped landslide sources and the large area (about 1000 km<sup>2</sup>) to be analyzed, we deemed the accuracy of Slabs3D sufficient and its speed to outweigh any potential improvements in accuracy offered by Scoops3D. Slabs3D computes  $F_3$  as follows (Hovland, 1977):

$$F_3 = \frac{\sum[(H\gamma_s - \psi\gamma_w)\ell_x\ell_y \cos \delta \tan \phi' + c'A]}{\sum H\gamma_s \ell_x \ell_y \sin \delta_\alpha} \quad (3)$$

In Eq. (3), the sums are taken over all the columns within the potential landslide. The quantities  $\ell_x$  and  $\ell_y$  are the horizontal grid-cell dimensions; the column height,  $H$ , is taken as the modeled soil depth from Step 1;  $\delta_\alpha$  is the apparent dip of the basal slip surface,  $b=b(x, y)$ , along the (assumed) direction of sliding.  $A$  is the true area of the failure surface at the base of the column (Hovland 1977; Hungr et al. 1989).

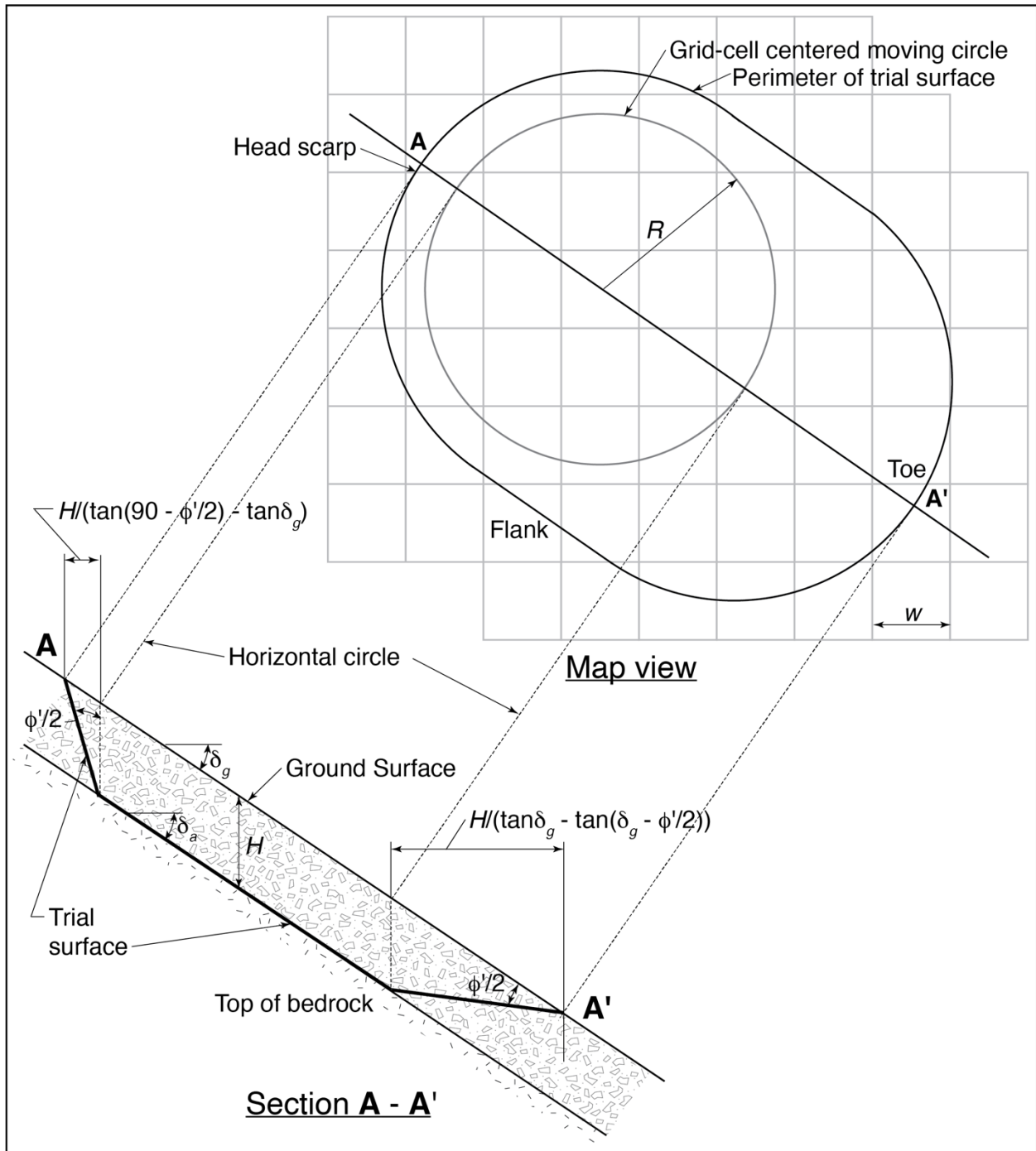
$$A = \ell_x \ell_y \sqrt{1 + \left(\frac{\partial b}{\partial x}\right)^2 + \left(\frac{\partial b}{\partial y}\right)^2} \quad (4)$$

The choice to take  $H$  as the modeled soil depth at each grid cell in Eq. (3) is consistent with field observations and previous modelling results. As noted previously, our field observations indicated that the base of most landslide sources occurred directly above a strength and permeability contrast. Except for cases of very rapid infiltration, TRIGRS computes the lowest factor of safety at  $Z_{max}$ . Smoothing the modeled soil depth reduces potential irregularities in the trial surface. Tests indicated that modest irregularities have only minor effect on  $F_3$  (Baum, 2023).

In Eq. (3), the effect of pore pressure has been computed in a manner consistent with the normal application of the principle of effective stress by subtracting the pore pressure or suction stress from the gravity induced stress rather than computing the resultants of pore pressure and gravity stress acting normal to the trial failure surface separately as in some implementations of the ordinary method of slices (Turnbull and Hvorslev 1967). Despite its limitations, Hovland's (1977) method of columns is always able to compute a factor of safety and is not subject to the convergence problems that occasionally occur with more sophisticated limit equilibrium methods.

514 As noted previously in the 1D analysis, Eq. (2) computes  $F_1$  at each grid cell for a range of depths from the ground  
515 surface down to a user specified maximum depth, which in this case is the computed soil depth,  $H$ , from step B.1  
516 (Baum et al. 2008, 2010). For the cases tested here, the minimum  $F_1$  always occurred at the base of soil, so we limited  
517 our search for 3D potential failures to those that follow the base of soil. In computing  $F_3$ , we searched the entire digital  
518 elevation model (DEM) for potential failures to a maximum depth of  $H$  using a circle of fixed diameter (in map view)  
519 centered at each grid cell to define the base of potential failure surfaces (one per grid cell, Fig. 7). Average dip direction  
520 of the base of soil within the circle determined the assumed slip direction. Potential failure surfaces enclosed by partial  
521 circles near the edges of the DEM were excluded from the analysis. Consequently, we extended the DEM grid well  
522 beyond the area needed for the final susceptibility map so that any inaccurate  $F_3$  values near the DEM grid boundaries  
523 could be discarded as described in the Sect. 3.10, "Removing edge effects." This approach of using map view circular  
524 trial failure surfaces resulted in potential landslides having the shape of an oblong slab or disc of variable thickness  
525 with tapered edges and rounded ends (Fig. 7), such that the trial surface was shaped somewhat like a gold pan. Beyond  
526 the limits of the search circle, the slab thins as the potential failure surface slopes from the approximate base of soil  
527 toward the ground surface. The failure surface at the head and flanks of the potential slides was assumed (based on  
528 Rankine theory, Lambe and Whitman 1969; Terzaghi et al. 1996) to slope  $90^\circ - \phi/2$  and beneath the toe to slope  $\delta_g -$   
529  $\phi/2$  (where  $\delta_g$  is the slope of the ground surface) from the ground surface down to the edge of the circle (Fig. 7). We  
530 estimated the contributions of wedges of material at the head, toe, and sides to total driving and resisting force by  
531 substituting formulas for height, length, width, average pressure head, and basal area ( $H$ ,  $l_x$ ,  $l_y$ ,  $\psi$ , and  $A$ ) of each side  
532 wedge, into Eq. (3) (Fig. 7), rather than subdividing the wedges into their component square columns or partial  
533 columns and summing their individual contributions. The size of these wedges is negligible with a grid resolution  
534 greater than the depth,  $H$ , as is often the case for our study areas, with soil depth commonly less than the 1-m resolution  
535 of our DEM. The wedge formulas are exact only for constant  $H$ . Although variable  $H$  across the trial surface introduces  
536 minor uncertainty into  $F_3$ , the formulas are sufficiently accurate for estimating the value of  $F_3$  for assessing stability  
537 of the soil mantle over large areas.

538



539  
 540 **Figure 7. Sketch showing moving circle search strategy and trial surface geometry used in computing approximate 3D**  
 541 **factor of safety,  $F_3$ . All grid cells whose center is inside the circle are included in the computation of  $F_3$ , and cells in**  
 542 **the head scarp, flank, and toe areas are combined to form wedges for computational purposes. The trial surface has a**  
 543 **map view radius  $R$ ;  $\delta_g$  is the slope of the ground surface;  $\delta_a$  is the apparent dip of the trial surface in the assumed**  
 544 **direction of sliding (average slope direction of grid cells centered within the horizontal circle);  $H$  is height of a grid-**  
 545 **cell centered column from the trial surface to the ground surface; and  $\phi'$  is the angle of internal friction of the soil for**  
 546 **effective stress (modified from Daum et al. 2012). For the case depicted in Section A - A' (above),  $H$  is constant and**

1.5 times the horizontal width,  $w$ , of the square grid cells. As the average value of  $H/w$  decreases and as  $R$  increases, the perimeter of the trial surface contracts toward the projection of the horizontal circle onto the ground surface. For variable soil depth models,  $H$  may vary from cell to cell and the value of  $H$  for the grid cell closest to the upslope or downslope edge of the horizontal circle is used in the formulas shown in the cross section for horizontal dimensions of the scarp and toe respectively.

### 3.5.4 Soil-depth model calibration

Field observations indicated that the base of most landslide sources occurred near the top of weathered bedrock (Baum et al. 2018; Baum 2021), so we chose soil depth as a predictor of landslide source depth. We carried out soil-depth estimation from DEMs using new open-source software, REGOLITH (Baum et al. 2021) containing five empirical and four steady-state process-based soil-depth models implemented in a command-line program. Each model in REGOLITH estimates soil depth from some combination of topographic variables, including slope, upslope contributing area, and curvature, as well as a few model parameters, such as characteristic depth (the soil thickness at which bedrock lowering falls to 1/e of its maximum value),  $h_0$  [L]; critical slope (angle of stability at which the slope is capable of transporting the entire soil profile by mass movement),  $\delta_c$  [degrees]; and the ratio of maximum bedrock lowering rate to hillslope diffusivity,  $R_d$ . These parameters may vary with conditions that influence soil formation, including bedrock and climate. Predicted soil depth is treated as equivalent to and defines column height,  $H$ , in subsequent modelling steps. We modified steady-state process-based models (Pelletier and Rasmussen 2009), which predict soil depth only on convex topography, to estimate soil depths in both concave and convex topography. We used a smoothing algorithm available in REGOLITH to reduce abrupt changes in soil depth that may result from DEM roughness. Further details are available in the online documentation found in the code repository (Baum et al. 2021). Our soil-depth, pressure head, and slope-stability models treated roads, cut slopes and embankments the same as other areas.

Soil-depth model calibration proceeded first by fitting soil-depth models to depth observations followed by checking how the best-fitting models performed as input for computing  $F_1$  to predict landslide locations (see Sect. 3.6.5). Both calibration and checking made use of pre-event 1-m bare-earth lidar digital elevation models for the four ~2-km<sup>2</sup> calibration areas representing the dominant (three) geologic terranes affected by landslides in the study areas (Fig. 1). Landslides had previously been mapped (Bessette-Kirton et al. 2019c) and characterized (Baum et al. 2018) in these four calibration areas (Sec. 2.2, Fig. 3). Tello (2020) described the soil-depth calibration procedures in detail, including parameter ranges considered in the calibration. We summarize important steps here: -Field-measured landslide scars on unmodified hillsides (no obvious cut or fill) served as calibration points for soil depth. Only about 7-8 such scars were available for each calibration area. Tello (2020) adjusted GPS location of each calibration point to the center of its corresponding landslide polygon mapped from imagery by Bessette-Kirton et al. (2019c). A 5-m buffer around each point ensured adequate sampling of model depths to be compared with the field-measured maximum depth. Tello (2020) used a provisional version of the soil-depth code, REGOLITH (Baum et al. 2021), to model trial soil-depth distributions for the calibration areas. Multiple runs to incrementally sample the parameter spaces of several different



583 soil models implemented in REGOLITH produced hundreds of trial soil depth grids for each of the four calibration  
584 areas. Soil models tested include a linear area- and slope-dependent model (LASD) (Ho et al. 2012) and modified  
585 forms of Pelletier and Rasmussen's (2009) non-linear slope- (NSD), area- and slope- (NASD), and slope- and depth-  
586 dependent (NDS) models. Testing these against the field-measured landslide-scar maximum depths resulted in  
587 optimized input parameters for each model and area (Tello 2020).

588 Tello (2020) used a range of statistical metrics identified by Gupta et al. (2009) to determine predictive success of the  
589 model outputs. Most important of these was the Euclidian distance from the ideal point,  $ED$ . The ideal point is  
590 characterized by perfect correlation between observed and simulated points and by perfect agreement between the  
591 means and standard deviations of the observed and simulated point distributions,

$$592 \quad ED = \sqrt{(r - 1)^2 + (\alpha - 1)^2 + (\beta - 1)^2} \quad (51)$$

593 where the ideal point is at  $r=1, \alpha=1, \beta=1$  so that  $ED=0$ . The linear correlation coefficient,  $r$ , relative variability,  $\alpha$ , and  
594 the bias relative to the observed sample,  $\beta$ , define the ED in eq. (15) (Gupta et al. 2009). In eq. (15) the relative  
595 variability is the ratio of the standard deviation of the simulated values,  $\sigma_s$ , to the standard deviation of the observed  
596 values,  $\sigma_o$ , ( $\alpha=\sigma_s/\sigma_o$ ). Likewise, the bias is the ratio of mean of the simulated values,  $\mu_s$ , to the mean of the observed  
597 values,  $\mu_o$  ( $\beta=\mu_s/\mu_o$ ). The linear correlation coefficient,  $r$ , indicates the quality of a least-squares fit of the simulated  
598 values to the observed values, with  $r=1$  indicating a perfect fit. The model run having the lowest ED usually had the  
599 best fit, unless  $ED > 1$  (Tello 2020). Where  $ED>1$ , we chose the model run with  $\beta$  closest to 1 so that the mean  
600 simulated depth would be as close as possible to the mean of depth observations (Gupta et al. 2009). The best-fit soil-  
601 depth distribution corresponded in turn to a best-fit parameter set for each soil-depth model type. Comparison of best  
602 scores for each model type identified the overall best fit of all models tested.

### 603 **3.6-5 Soil model evaluation and one-dimensional slope-stability model calibration**

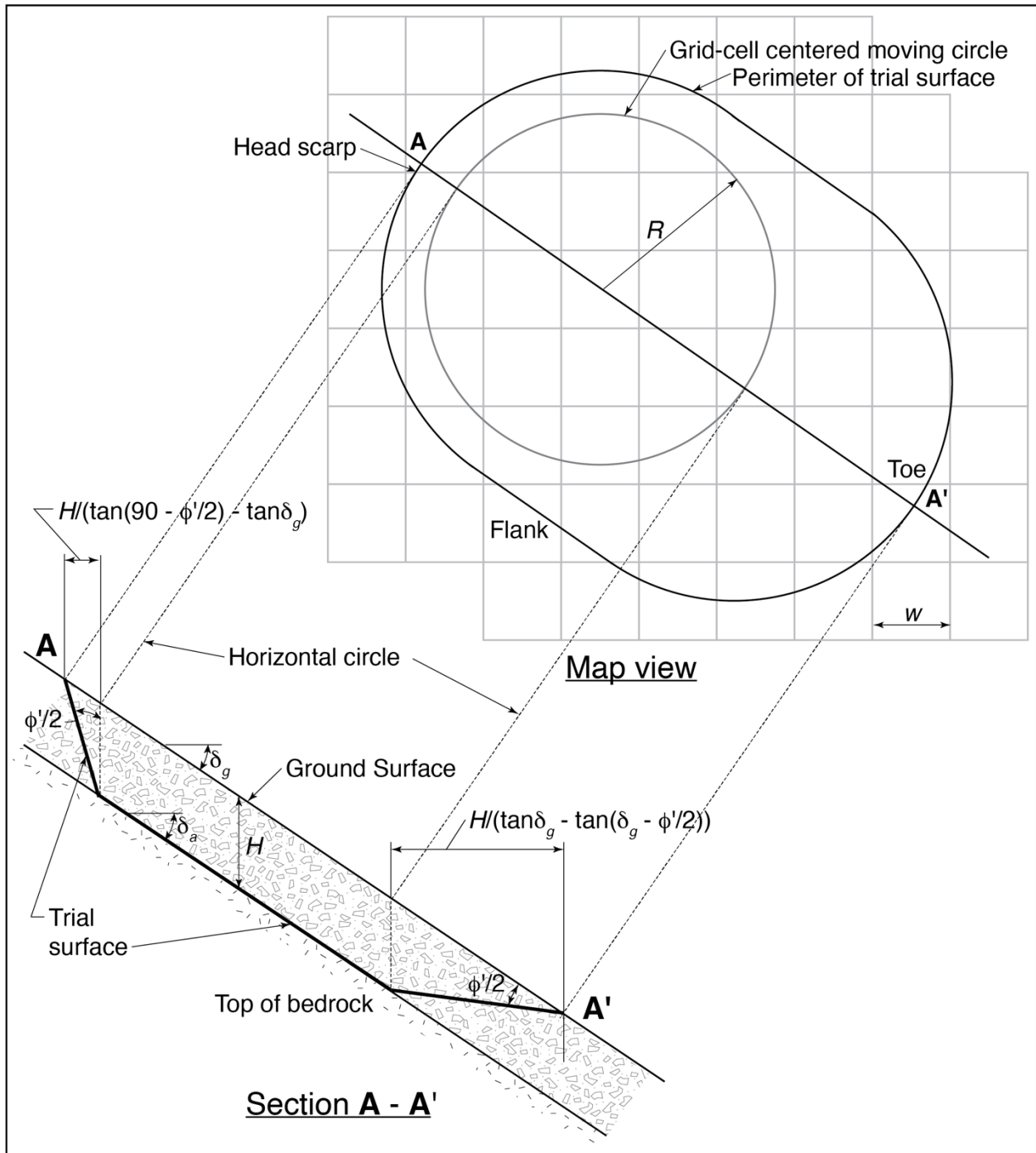
604 To further evaluate the soil-depth modelling results and finish calibrating the slope-stability model, we computed  $\psi$   
605 and  $F_1$  as implemented in TRIGRS (Baum et al. 2010; Alvioli and Baum (2016) for dry and steady saturated soil  
606 conditions (supplemental text S1 and S2) using the better performing soil-depth models for each calibration area.  
607 Previously defined better performing (TPR  $\geq 75\%$ ) ranges of  $\phi'$  (38°-60°) and  $c'$  (0-4 kPa) (Baum 2021; Fig. 65b,  
608 5e6c, 5d6d) defined the parameter space for computing  $F_1$  with a well-performing subset of trial soil-depth  
609 distributions. In addition, we required  $F_1 > 1$  in 99.9% of grid cells for  $\psi(H)=0$  to ensure slope stability under dry  
610 conditions. Computing  $F_1$  over the calibration areas using the best-fit distributions for each soil-depth model type and  
611  $\phi'$  and  $c'$  combinations produced many  $F_1$  grids. Receiver Operator Characteristics (ROC) analysis (Metz, 1978;  
612 Fawcett 2006; Begueria 2006) of these  $F_1$  grids against mapped landslide scarp points indicated which combinations  
613 of trial soil-depth distribution and strength parameters predicted the most observed landslides, based on the area under  
614 the ROC curve. Using parameters from the highest performing  $F_1$  distribution, we selected the preferred soil depth  
615 model and  $\phi'$  and  $c'$  values for modelling  $F_1$  in the large study areas enclosing Lares, Utuado, and Naranjito  
616  
617

618 municipalities. The calibration areas represented different geologic terranes having the highest densities of landslides  
619 in the study areas so that the calibration procedure yielded separate model and parameter values relevant to each of  
620 these terranes.

### 621 3.6 Quasi-three-dimensional slope stability calibration

622 After  $H$  and  $F_1$  values had been improved as much as possible by calibration, we began test calculations of  $F_3$  as  
623 implemented in the new open-source code Slabs3D (Baum, 2023; supplemental text S3) and worked to further refine  
624 potential landslide source areas. We varied the size of the trial surface from a 3.5-m radius to a 10.5-m radius (Fig. 7)  
625 and used ROC analysis along with information about observed source-area sizes to determine the optimum  $F_3$  radius.  
626 In addition to these quantitative assessments, we inspected the maps to confirm that the susceptibility zones and  
627 potential source areas made sense topographically, mechanically, and geologically. These inspections helped ensure  
628 that potential landslide source areas were consistent with observations and expectations for hillsides whether they  
629 were relatively undisturbed or modified by roads, cut slopes, and embankments. The inspections led to some minor  
630 revisions of the computer code to correct map errors (such as spurious spots of low factor of safety), followed by  
631 repeated model runs.

632 Due to insufficient data, rigorous calibration was not possible for some ~~parameter zones~~ areas, such as the karst areas  
633 of Bawiec's (1998) Limey sediment terrane. We adjusted model parameters (reduced maximum soil depth,  $H_{max}$ , and  
634 characteristic soil depth,  $h_0$ , for the soil-depth model and increased  $c'$  for computing  $F_1$  and  $F_3$ ) for the Limey sediment  
635 terrane's ~~parameter zone~~ to account for the terrane's low landslide density during Hurricane María.



636

637 Figure 7. Sketch showing moving circle search strategy and trial surface geometry used in computing approximate 3D  
 638 factor of safety,  $F_3$ . All grid cells whose center is inside the circle are included in the computation of  $F_3$ , and cells in the head  
 639 scarp, flank, and toe areas are combined to form wedges for computational purposes. The trial surface has a map-view  
 640 radius  $R$ ;  $\delta_g$  is the slope of the ground surface;  $\delta_a$  is the apparent dip of the trial surface in the assumed direction of sliding  
 641 (average slope direction of grid cells centered within the horizontal circle);  $H$  is height of a grid-cell centered column from  
 642 the trial surface to the ground surface; and  $\phi'$  is the angle of internal friction of the soil for effective stress (modified from  
 643 Baum et al. 2012). For the case depicted in Section A-A' (above),  $H$  is constant and 1.5 times the horizontal width,  $w$ , of the  
 644 square grid cells. As the average value of  $H/w$  decreases and as  $R$  increases, the perimeter of the trial surface contracts  
 645 toward the projection of the horizontal circle onto the ground surface. For variable soil-depth models,  $H$  may vary from  
 646 cell to cell and the value of  $H$  for the grid cell closest to the upslope or downslope edge of the horizontal circle is used in the  
 647 formulas shown in the cross section for horizontal dimensions of the scarp and toe respectively.

### 648 3.7 Geologic mapping and parameter zonation

649 Bawiec (1998) compiled published 1:20,000-scale geologic mapping of Puerto Rico and (as noted previously)  
650 combined related formations into geologic terranes (Fig. 1 and Bawiec 1998). Based on the results of early studies  
651 (Besette-Kirton et al. 2019a) and our calibration efforts, the geologic terranes became the basis for subdividing the  
652 study areas into parameter zones. The topographic base maps available at the time of geologic mapping lacked the  
653 detail of the pre-event lidar-derived topography used in this study. Trial computations of  $F_1$  and  $F_3$  on the study area  
654 DEM tiles indicated that a uniform soil depth model across the highly susceptible geologic terranes resulted in a more  
655 accurate susceptibility map than a zoned model using the calibrated soil-depth parameters. This was likely a  
656 consequence of (1) having few soil-depth observations available from unmodified hillsides in each zone (section 3.4)  
657 as well as (2) a high degree of land surface modification from past agricultural activities, and road and residential  
658 construction resulting in weak calibration of the volcanoclastic and submarine basalt and chert geologic terranes.  
659 Consistent with results in Fig. 6a, Uniform-uniform values of  $\phi'$  and  $c'$  for the highly susceptible geologic terranes  
660 likewise resulted in good performance so we used the same soil depth and strength parameters for all three terranes  
661 (Supplemental Figures S1 and S2). Consequently, slight uncertainty in locations of boundaries between these terranes  
662 had no effect on computed  $F_1$  and  $F_3$  values. However, a large difference in landslide susceptibility and model  
663 parameters (maximum soil depth,  $h_0$ ,  $c'$ ) existed between the Limey sediment terrane with its cone karst and the highly  
664 susceptible terranes of the basement complex (submarine basalt, volcanoclastic, and granitoid). Offsets as great as tens  
665 of meters in the contact between the Limey sediment terrane and its neighbors along a prominent escarpment in Lares  
666 and Utuado resulted in errors in  $F_1$  and  $F_3$  along the escarpment. Consequently, Perkins et al. (2022) remapped the  
667 Limey sediment contact using lidar-derived shaded relief images and optical imagery to accurately delineate the  
668 transition from high to low landslide susceptibility across the contact. The contact was discerned based on the visually  
669 distinct differences between the closed basins and rugged karst cones of the Limey sediment terrane and the steep  
670 ridges and narrow branching valleys of the basement rocks.

### 671 3.8 Soil-depth modelling

672 After completing the calibration process, we created the overlapping rectangular tiles (described previously, Sec. 1.0,  
673 3.1) from the pre-event lidar bare-earth DEMs (~~Fig. 6~~Fig. 4, stage ~~B-C~~ and Fig. 1b, 1c). We created additional input  
674 files from the lidar-derived DEM tiles: flow accumulation grids for use with the area-dependent soil-depth models and  
675 parameter-zone grids for specifying different model input parameters (Sec. 3.6, 3.7~~-and step B-1~~, ~~Fig. 6~~Fig. 4). The  
676 parameter zones ensured a thinner and less continuous modeled soil mantle in the karst (Limey sediment terrane) than  
677 in areas underlain by the landslide-prone geologic terranes (Fig. 1). For comparison with the soil-depth models, we  
678 also used constant soil depth equal to the average depth, 1.4 m, observed at landslide scars.

### 679 3.9 Pressure-head and slope-stability modelling

680 Raster grids created from the soil-depth modelling defined soil depth ( $H$ ) and slope of the ground surface at each grid  
681 cell ~~in TRIGRS~~. We computed  $\psi$  and  $F_1$  using TRIGRS (Baum et al. 2010; Alvioli and Baum 2016), version 2.1, as  
682 described previously using the same lidar-derived DEM tiles and parameter zones as for soil-depth modelling (~~steps~~

683 ~~B.2 and B.3, Fig. 6~~Fig. 4). Then, using  $\psi(H)$  computed with TRIGRS ([supplemental text S1](#)) along with the same lidar  
684 tiles, parameter zones, and  $\phi'$  and  $c'$  values used in computing  $F_1$  as input for Slabs3D, we computed  $F_3$  ([step B.4, Fig.](#)  
685 [6](#)Fig. 4). The radius of each trial surface, as constrained by earlier testing in the calibration areas (Sect. 3.6, 4.5), was  
686 held constant at 3.5 m for all model runs on study area tiles.

~~687 After modelling potential source areas on pre-event topography, we recomputed the models using post-event 1-m lidar  
688 topography (U.S. Geological Survey, 2020a, b, c). We generated new slope, zone, and flow-accumulation grids from  
689 the post-event lidar and then ran REGOLITH, TRIGRS, and Slabs3D in succession (Fig. 6, steps C.1, C.2, C.3, and  
690 C.4) to indicate our best estimate of susceptibility to future landslide initiation.~~

### 691 **3.10 Removing edge effects**

~~692 To reduce edge effects (Fig. 6, step C.5) when joining the four overlapping tiles for Lares and Utuado to create a final  
693 map (based on post-event lidar), we first removed a 100-m buffer along all edges of each tile. At grid-cells where two  
694 tiles overlapped, differences in  $F_3$  tended to be small and we retained the greater  $F_3$  value. For the single tile covering  
695 Naranjito, we removed only the 100-m buffer along all tile edges.~~

### 696 **3.11-10 Model testing and evaluation**

697 We used ROC analysis of  $F_3$  grids based on pre-event lidar topographic data compared to landslide head-scarp points  
698 mapped by Hughes et al. (2019) as a basis for testing performance and then defining susceptibility categories ([step](#)  
699 [B.5, Fig. 6](#)Fig. 4). Selecting the minimum  $F_3$  value within a 3-m radius around the scarp points accounted for  
700 uncertainty in their mapped locations. Validating  $F_3$  for pre-event topography was appropriate because it most  
701 accurately portrayed conditions at the time of Hurricane María. We computed true positive rate (TPR), false positive  
702 rate (FPR), and area under the TPR-FPR curve (AUC) and distance [to perfect classification, D2PC](#)~~from the ideal point~~  
703 ~~( $d_{HP}$ ), (0,1), ([Formetta et al. 2016](#))~~ to evaluate performance of pre-event  $F_3$  as a predictor of observed landslide scarp  
704 points. Analyzing landslide density distribution across  $F_3$  provided a further check on model accuracy. We computed  
705 landslide densities in 0.1 increments of  $F_3$  to check for a general trend of decreasing observed density with increasing  
706  $F_3$ . ~~We also continued map inspections as described in Section 3.6. In addition to these quantitative assessments, we  
707 inspected the maps to confirm that the susceptibility zones and potential source areas made sense topographically,  
708 mechanically, and geologically. These inspections helped ensure that potential landslide source areas were consistent  
709 with observations and expectations for hillsides whether they were relatively undisturbed or modified by roads, cut  
710 slopes, and embankments. The inspections led to some minor revisions of the computer code to correct errors, followed  
711 by repeated model runs.~~

712  
713 As an additional check we computed ROC statistics for minimum  $F_3$  values within source areas mapped by Baxstrom  
714 et al. (2021a) and Einbund et al. (2021a, 2021b). Their detailed landslide source mapping covers only a fraction of the  
715 study areas (Fig. 1), whereas the scarp points mapped by Hughes et al. (2019) cover the entire island. However, source  
716 area polygons enclose pixels that are more relevant to testing performance of  $F_3$  than circles centered at the scarp  
717 points.

718 Evaluating the model to address the need for a conservative landslide susceptibility map led us to select threshold  
719 values of  $F_3$  enclosing specific percentages (or TPR) of landslide points. Our reason for doing so rather than placing  
720 the category break at  $F_3 = 1$  is to account for model and parameter uncertainty. Every  $F_3$  contour on the map encloses  
721 a specific percentage of landslide points. Contours at high  $F_3$  values enclose more landslide points than low  $F_3$   
722 contours. We selected  $F_3$  contours corresponding to TPR of 0.75 and 0.90 of Hurricane María-produced landslide  
723 head-scarp points (Hughes et al. 2019) to define the limits of very high (TPR  $\leq 0.75$ ), high ( $0.75 \leq$  TPR  $\leq 0.90$ ), and  
724 moderate (TPR  $> 0.90$ ) landslide source susceptibility zones. The high and very high susceptibility zones both indicate  
725 significant danger from landslides but allow users to distinguish areas having greater potential for long runout (Brien  
726 et al. 2021). These classes include most mapped landslide points as well as the adjacent steep slopes where they  
727 occurred, while limiting the overall areal extent of the very high and high susceptibility classes. Using the same  $F_3$   
728 thresholds at TPR  $\leq 0.75$  and TPR  $\leq 0.90$  determined for the pre-event topography (step B.5, Fig. 6), we then defined  
729 landslide susceptibility zones using post-event topography across the three municipalities (step C.5, Fig. 6). These  
730 zones estimate the potential for future shallow landslides.

### 731 3.11 Modelling potential landslides on post-storm topography

732 After modelling potential source areas on pre-event topography, we recomputed the soil depth, pressure head, and  
733 factor of safety using post-event 1-m lidar topography (U.S. Geological Survey, 2020a, b, c). We generated new slope,  
734 zone, and flow-accumulation grids from the post-event lidar and then ran REGOLITH, TRIGRS, and Slabs3D in  
735 succession (Fig. 4) to indicate our best estimate of susceptibility to future landslide initiation.

### 736 3.12 Removing edge effects and applying susceptibility categories

737 We joined the four overlapping tiles for Lares and Utuado to create a final landslide susceptibility map (based on post-  
738 event lidar). To reduce edge effects (Fig. 4) when joining the four tiles, we first removed a 100-m buffer along all  
739 edges of each tile. At grid cells where two tiles overlapped, differences in  $F_3$  tended to be small and we retained the  
740 greater  $F_3$  value. For the single tile covering Naranjito, we removed only the 100-m buffer along all tile edges.

741 We then classified landslide susceptibility for post-event topography across the three municipalities using the same  
742  $F_3$  thresholds at TPR  $\leq 0.75$  and TPR  $\leq 0.90$  determined for the pre-event topography (Fig. 4). These thresholds divide  
743 the map area into zones of varying susceptibility to landslide initiation. The resulting susceptibility zones estimate the  
744 potential for future shallow landslides (Fig. S1 and S2).

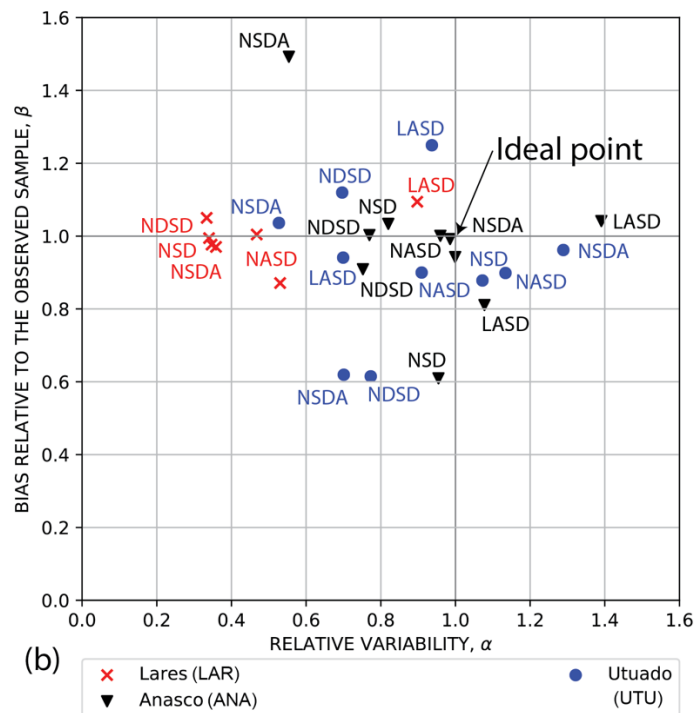
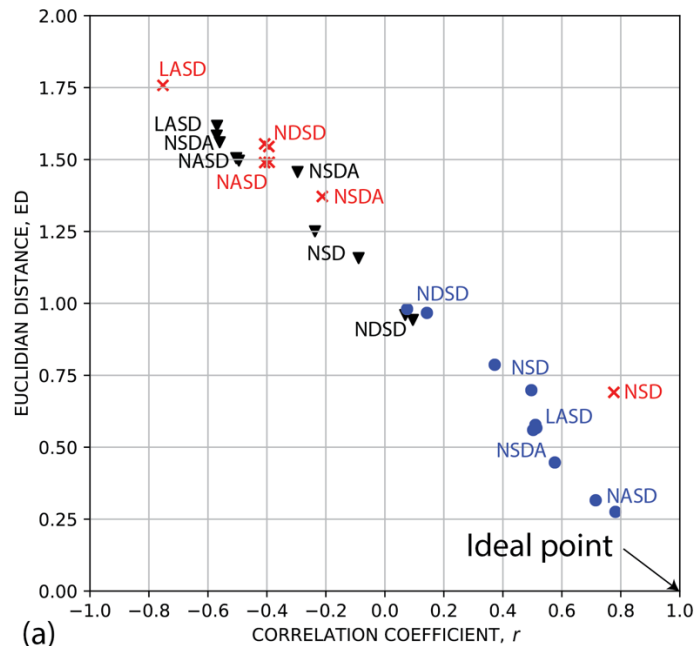
## 745 **4 Results**

### 746 **4.1 Soil-depth calibration**

747 We calibrated soil depth to field measurements (Fig. 6Fig. 4, step A.1section 3.4) for three (ANA, LAR, UTU) of the  
748 four calibration areas and calculated Euclidian distance from the ideal point, ED (Eq. 51), correlation coefficient,  $r$   
749 (and other statistical parameters as outlined in Tello 2020) to determine which models and parameter sets gave the  
750 closest match to field observations (Fig. 8a, b). No soil depth calibration was performed for NAR as depth

751 measurements in Naranjito were mainly outside the area mapped by Bessette-Kirton et al. (2019c). Limiting the  
752 observed depths to landslide scars on relatively unmodified slopes resulted in sample sizes of only seven or eight  
753 observation points (landslide sources) per calibration area. Most soil-depth models for the Utuado calibration area  
754 (UTU) had acceptable performance as indicated by positive correlation between observed and simulated depths ( $0.08$   
755  $\leq r \leq 0.78$ ), and ED ranging from 0.28 to 0.99 (Fig. 8a; Tello 2020). Of these, the modified nonlinear area and slope  
756 (NASD) model had the smallest ED, 0.28, and the largest  $r$ , 0.78 (Fig. 8a). Other better-performing models were a  
757 nonlinear slope-dependent model with linear area dependence (NSDA) and a linear area- and slope-dependent model  
758 (LASD) based on the wetness index (Ho et al. 2012). In contrast, most soil-depth models for the Añasco (ANA) and  
759 Lares (LAR) calibration areas performed poorly, with negative or small positive correlation ( $r < 0.16$ ) and  $0.69 < ED$   
760  $< 1.8$  (Fig. 8a). The poor correlation probably resulted from the small sample sizes of observed depths in these areas.  
761 At LAR, only the nonlinear slope dependent model (NSD, see Pelletier and Rasmussen 2009) had acceptable  
762 performance with  $r = 0.78$  and  $ED = 0.69$  (Fig. 8a). The NASD model had  $\alpha$  and  $\beta$  closest to 1, for both ANA and LAR  
763 (Fig. 8b).

764



765

766

767

768

769

770

771

772

773

774

Figure 8. Soil-depth model calibration measures for Anasco (ANA), Lares (LAR) and Utuado (UTU) calibration areas (Fig. 1). Performance is based on comparing maximum landslide depth at field-mapped landslide points from unmodified hillsides against modeled depths within a 5-m radius of the point for all field-mapped points in the calibration area. GPS point locations were corrected as needed by moving them to the centers of corresponding landslide polygons mapped by Bessette-Kirton et al. (2019c). (a) Primary metrics, Euclidian distance from the ideal point, ED (smaller is better), versus correlation coefficient,  $r$ , (b) bias relative to the observed sample,  $\beta$ , versus relative variability,  $\alpha$ . The ideal point is at  $r=1$ ,  $\alpha=1$ ,  $\beta=1$ . [Soil-depth models: LASD, linear area- and slope-dependent model; NASD, nonlinear area- and slope-dependent model; NDS, nonlinear slope-dependent model; NSD, nonlinear slope-dependent model; NDSA, nonlinear slope-dependent model with linear area dependence].



775

776 **4.2 Soil-depth model evaluation and slope-stability calibration results**

777 Slope stability parameter calibration compared  $F_1$  values for previously determined ranges of  $c'$  and  $\phi'$  (Fig. 65) for  
 778 each of the soil depth models to find the best-performing combination of soil model and strength parameters for  
 779 predicting landslide source locations in each calibration area (Fig. 6 Fig. 4, steps A.3.a and A.3.b section 3.5). For UTU,  
 780 the NASD model performed best with the NSDA model close behind (Tello 2020) based on area under the TPR –  
 781 FPR curve and minimum distance of the curve from the ideal point perfect classification. Parameter combinations and  
 782 ROC results for the best-performing model in each area appear in Table 1. Despite poor soil depth model performance  
 783 metrics for ANA and LAR (Fig. 8), the  $F_1$  calculations for the three calibration areas indicated that the NASD soil  
 784 depth model had the greatest predictive strength for locations of landslide source areas in ANA, LAR, and UTU with  
 785 similar results (Table 1). Despite lack of soil-depth calibration in NAR, results in this study area were like the other  
 786 three calibration areas (Table 1). Values of  $\delta_c$  near  $60^\circ$  gave the best soil-depth model results (Table 1), despite  
 787 variability in the steepest slopes where landslides occurred in the different terranes (Fig. 3d, 4).

788

789 **Table 1. Calibration results for 1D factor of safety,  $F_1$ , with soil depth models by calibration area (Fig. 1). Positives and**  
 790 **negatives in the ROC analysis based on total pixels within and outside the estimated source areas of landslide polygons**  
 791 **mapped by Bessette-Kirton et al. (2019c) and whether the pixels have  $F_1 > 1$  or  $F_1 < 1$  (Tello 2020). [Symbols and**  
 792 **abbreviations: NASD, non-linear area and slope dependent soil-depth model of Pelletier and Rasmussen (2009) as modified**  
 793 **by Baum et al. (2021);  $H_{max}$ , maximum soil depth;  $\delta_c$ , critical slope angle;  $R_d$ , diffusivity ratio;  $c'$ , soil cohesion for effective**  
 794 **stress;  $\phi'$ , angle of internal friction for effective stress; AUC, area under the curve of true-positive-rate (TPR) and false**  
 795 **positive rate (FPR) (larger is better);  $d_{TPD2PC}$ , distance from the ideal point perfect classification, (0,1), to nearest point on**  
 796 **the TPR-FPR curve (smaller is better); Best  $F_1$ , 1D factor of safety at point on the TPR-FPR curve nearest to the ideal**  
 797 **point, (0,1), and therefore the most accurate  $F_1$  classifier of landslide versus non-landslide grid cells for the particular model**  
 798 **(closer to one is better);  $^\circ$ , degrees.]**

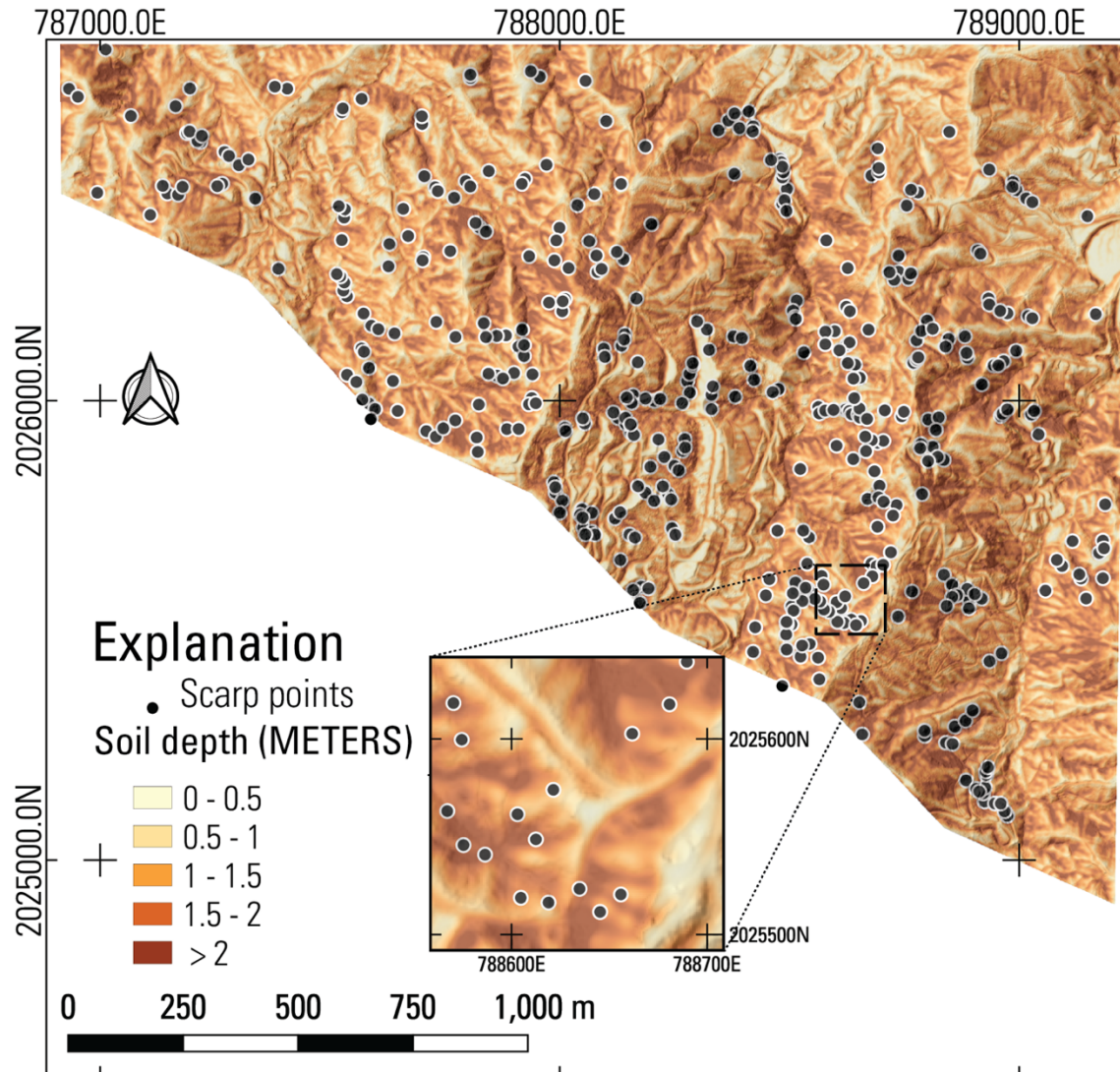
799

Calibration area	Soil Model	$H_{max}$ (m)	$\delta_c$ ( $^\circ$ )	$R_d$	$c'$ (kPa)	$\phi'$ ( $^\circ$ )	AUC	$d_{TPD2PC}$	Best $F_1$
Utuaado (UTU)	NASD	2.0	60	1.0	2.5	45 $^\circ$	0.67	0.48	1.5
Añasco (ANA)	NASD	3.0	60	0.16	4.5	45 $^\circ$	0.70	0.46	1.1
Lares (LAR)	NASD	3.0	60	0.25	4.5	45 $^\circ$	0.66	0.52	1.1
Naranjito (NAR)	NASD	3.0	60	0.2	4.0	45 $^\circ$	0.65	0.54	1.2

800

### 801 4.3 Modeled soil depth

802 Having completed the soil-depth model calibration (Sec. 4.1) and testing (Sec. 4.2), we modeled soil depth in the  
803 larger map tiles preparatory to analyzing slope stability (~~Fig. 6~~[Fig. 4, step B.1](#)[section 3.8](#)). Each tile covers hundreds  
804 of km<sup>2</sup>, so we illustrate results using the NAR area, chosen to demonstrate that our susceptibility workflow can achieve  
805 very good results even with limited landslide source depth observations. As noted previously, insufficient field-  
806 measured landslide points prevented soil-depth model calibration (Sec. 4.1), but not model evaluation and slope  
807 stability calibration (Sec. 4.2) for NAR. Figure 9 shows predicted soil depth for the best performing soil-depth model  
808 (based on the slope-stability evaluations, Sec. 4.2) in NAR (see Fig. 1 for location). The model shown in Fig. 9 predicts  
809 greater soil depth in hollows than on ridges. Other models that were tested (not shown) produced somewhat similar  
810 results. Differences in model structure produce different responses to topographic features, including flat areas, road  
811 cuts, and steep slopes. For example, the modified NASD and NSDA models predicted deep soils ( $\leq 3$  m for parameters  
812 chosen) in convergent areas, on steep slopes, including road cuts and embankments; thin soils on ridge crests, and thin  
813 or no soil on downslope flat areas (see large flat area on east edge of Fig. 9). In contrast, the LASD and NDSD models  
814 predicted deep soils ( $\leq 3$  m for parameters chosen) in convergent areas and on flats and thin soils on ridge crests and  
815 steep slopes (except where they occur in strongly convergent topography). [These topographic features](#) were more  
816 distinct in the three nonlinear models, NASD, NSDA, and NDSD, than in the linear LASD model.



817  
 818 **Figure 9.** Best-performing version of soil depth maps from soil-depth models tested for the Naranjito (NAR) calibration  
 819 area in volcaniclastic terrane (Fig. 1). Topographic base derived from lidar by U.S. Geological Survey (2018), scarp points  
 820 from Bessette-Kirton et al. (2019c). The modified Nonlinear Area- and Slope-dependent (NASD) model (modified from  
 821 Pelletier and Rasmussen 2009, as implemented by Baum et al. 2021) depicted here, was the overall best-fitting soil-depth  
 822 model for this terrane. Inset shows details of a 150 m by 150 m area, with thicker soil accumulation in concave areas.

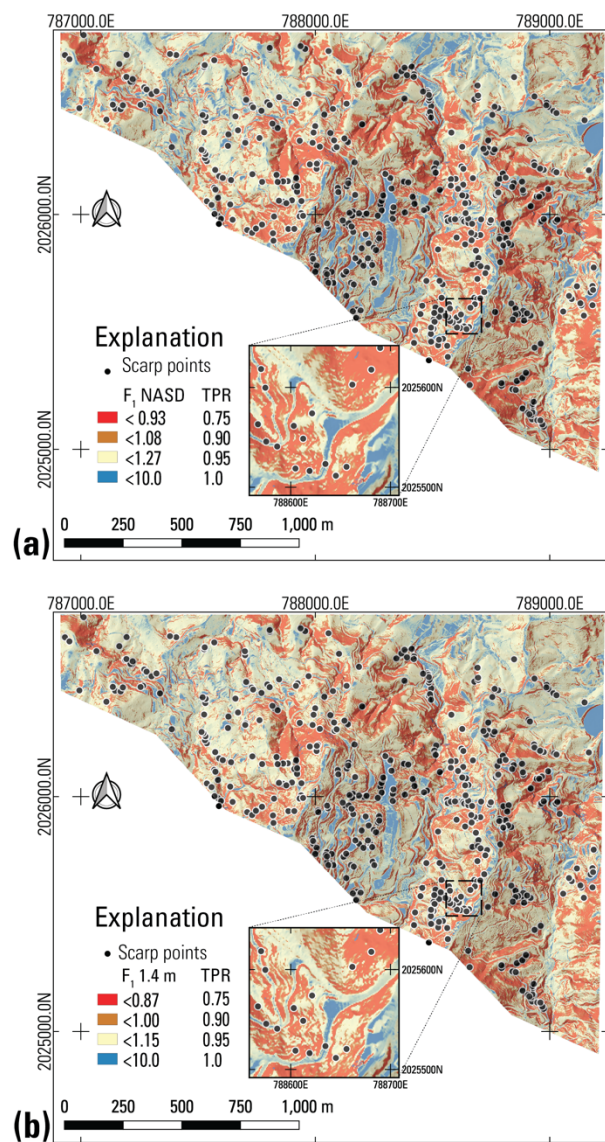
823

#### 824 4.4 One-dimensional factor of safety

825 Figure 10 shows  $F_1$  optimized for NAR and calculated using TRIGRS and the soil model results in Fig. 9, as well as  
 826  $F_1$  for constant soil depth. Slopes steeper than  $60^\circ$ , the estimated critical slope angle, were treated as barren (zero or  
 827 negligible soil thickness) and stable because landslides were very rare on slopes steeper than  $60^\circ$  (Fig. 3d). On slopes  
 828 flatter than  $60^\circ$ , Soil-soil strength parameters are within the ranges obtained by sensitivity analysis of  $F_1$  parameters  
 829  $\phi'$  and  $c'$  over observed ranges of slope and depth of landslides characterized in the field at ANA, LAR, UTU, and  
 830 NAR (Fig. 65). The only landslide source locations available throughout the three municipalities are the scarp points

831 of Hughes et al. (2019). Due to location uncertainty, we used a 3-m radius around the scarp points for defining true  
 832 positives. Color thresholds on the maps (Fig. 10) are based on  $F_1$  at TPR of 0.75, 0.90, and 0.95. Consequently,  
 833 thresholds for  $F_1$  differ for each panel in Fig. 10. The same TPR values (0.75, 0.90, 0.95) were used for picking  $F_3$   
 834 thresholds for landslide initiation susceptibility across the entire study area covering Naranjito, Utuado, and Lares  
 835 Municipalities in the final maps (Supplemental Figures S1 and S2).

836



837  
 838 **Figure 10. Maps of Naranjito (NAR) calibration area in volcanoclastic terrane (Fig. 1) showing 1D factor of safety ( $F_1$ )**  
 839 **results for a) soil-depth model shown in Figure 9 as well as b) constant average soil depth. Topographic base derived from**  
 840 **lidar by U.S. Geological Survey (2018), scarp points from Bessette-Kirton et al. (2019c). True positives determined by**  
 841 **minimum  $F_1$  within a 3-m radius of the scarp points. (a)  $F_1$  for NASD, the modified nonlinear area- and slope-dependent**  
 842 **soil-depth model depicted in Fig. 9, (b)  $F_1$  for constant soil depth of 1.4 m. Inset shows details of a 150 m by 150 m area.**

843

844 Areas of low  $F_1$  are similar in overall pattern between the two maps shown in Fig. 10 but differ in detail. These details  
 845 include small areas of low  $F_1$  unique to each model as well as variation in the extent of major areas of low  $F_1$ . Many  
 846 boundaries of the areas of low  $F_1$  are ragged and small patches of yellow, indicating higher  $F_1$ , occur within the larger  
 847 red and orange areas of low  $F_1$ . Differences in  $F_1$  between the maps are attributable mainly to variation in soil depth  
 848 and partly to variation in  $c'$ . The optimum value of  $c'$  varied depending on the characteristics of each soil model (Table  
 849 2). The results shown in Fig. 10 are for the best-performing combination of  $c'$  and  $\phi'$  for the soil-depth model at NAR  
 850 (Fig. 9 and Sec. 4.2) and for constant average depth of 1.4 m.

851  
 852 The different  $F_1$  patterns shown in Fig. 10 correspond to slightly different levels of predictive success. The AUC and  
 853 distance from the ideal point perfect classification (0,1) to the nearest point on the TPR-FPR curve,  $\#_{HPD2PC}$  indicate  
 854 that  $F_1$  for constant depth has the highest predictive skill (AUC=0.88,  $\#_{HPD2PC}$ =0.26,  $F_1$  value nearest the ideal  
 855 point perfect classification,  $F_1$ =0.9). Next,  $F_1$  for the NASD model performed almost as well (AUC=0.86,  
 856  $\#_{HPD2PC}$ =0.30,  $F_1$  value nearest the ideal point perfect classification,  $F_1$ =1.0). When applied to the entire DEM tile  
 857 covering Naranjito municipality,  $F_1$  for constant depth and NASD tied with AUC = 0.86 and  $\#_{HPD2PC}$  = 0.30 (constant  
 858 depth) and  $\#_{HPD2PC}$  = 0.29 (NASD). Thus, the performance edge of constant depth is localized at NAR and does not  
 859 extend across the entire Naranjito DEM tile. Other soil-depth models performed slightly worse (Table 2) consistent  
 860 with results obtained by Tello (2020) for UTU. The slightly higher performance for  $F_1$  with constant depth at NAR  
 861 comes at the cost of the area classified as very high, high, or moderate susceptibility (TPR = 0.95) being more diffuse,  
 862 with more ragged boundaries, than for  $F_1$  with NASD (Fig. 10a, b). Varying the amount of cohesion used with a  
 863 particular soil model caused small changes in the AUC,  $\#_{HPD2PC}$ , and best  $F_1$  as shown by the two entries for NDS  
 864 in Table 2.

865  
 866 **Table 2. Key inputs and performance measures for factor of safety calculations based on the infinite slope model ( $F_1$ ), as**  
 867 **implemented by TRIGRS, in the Naranjito calibration area (NAR). Performance is based on minimum  $F_1$  within a 3-m**  
 868 **radius of landslide scarp points mapped by Hughes et al. (2019). [Symbols and abbreviations: NASD, non-linear area and**  
 869 **slope dependent soil-depth model of Pelletier and Rasmussen (2009) as modified by Baum et al. (2021); NSDA, non-linear**  
 870 **slope dependent model of Pelletier and Rasmussen (2009) modified by Baum et al. (2021) to include linear area dependence;**  
 871 **NDS, non-linear slope and depth dependent model of Pelletier and Rasmussen (2009); LASD, linear area and slope**  
 872 **dependent model of Ho et al. (2012);  $H_{max}$ , maximum soil depth;  $\delta_c$ , critical slope angle;  $R_d$ , diffusivity ratio;  $C_0$ , empirical**  
 873 **constant used in LASD;  $c'$ , soil cohesion for effective stress;  $\phi'$ , angle of internal friction for effective stress; AUC, area**  
 874 **under the curve of true-positive-rate (TPR) and false positive rate (FPR) (higher is better);  $\#_{HPD2PC}$ , distance from the**  
 875 **ideal point perfect classification, (0,1), to nearest point on the TPR-FPR curve (smaller is better); Best  $F_1$ , 1D factor of safety**  
 876 **at point nearest to the ideal point perfect classification, (0,1), and therefore the most accurate  $F_1$  classifier of landslide versus**  
 877 **non-landslide grid cells for the particular model (closer to 1.0 is better); °, degrees ; -- not applicable.]**

Soil Model	$H_{max}$ (m)	$\delta_c$ (°)	$R_d$ or $C_0$	$c'$ (kPa)	$\phi'$ (°)	AUC	$\#_{HPD2PC}$	Best $F_1$	TPR at $\#_{HPD2PC}$
NASD	3.0	60	0.20	4.0	45°	0.86	0.30	1.0	0.82
LASD	3.0	60	0.45	3.5	45°	0.85	0.31	1.1	0.84
NDS	3.0	60	0.10	4.5	45°	0.82	0.36	1.2	0.75
NDS	3.0	60	0.10	2.5	45°	0.86	0.32	1.0	0.89
NSDA	3.0	60	0.10	4.5	45°	0.85	0.30	1.1	0.80

Constant	1.4	60	--	4.0	45°	0.88	0.26	0.9	0.79
----------	-----	----	----	-----	-----	------	------	-----	------

878

#### 879 4.5 Quasi-three-dimensional factor of safety

880 Figure 11 shows  $F_3$  computed using the soil-depth model in Fig. 9 and constant soil depth of 1.4 m. Predictive skill  
881 for  $F_3$  is somewhat less than  $F_1$ ; AUC is 0.05 – 0.08 less for  $F_3$  than corresponding  $F_1$  (Tables 2 and 3). The only  
882 exception is for the constant soil depth model results where  $F_3$  has the highest AUC, 0.94, of all cases tested (Fig. 12a  
883 and 12b). Despite the overall slightly worse performance of  $F_3$  it provided smoother boundaries on the landslide  
884 susceptible areas (Fig. 11a, b), which also are more continuous than corresponding  $F_1$  landslide susceptible areas (Fig.  
885 10). The lower AUC values resulted from the  $F_3$  susceptible areas covering slightly more land area than the  
886 corresponding  $F_1$  areas at the same TPR. Therefore, the  $F_3$  susceptibility maps are more conservative than their  $F_1$   
887 counterparts.

888

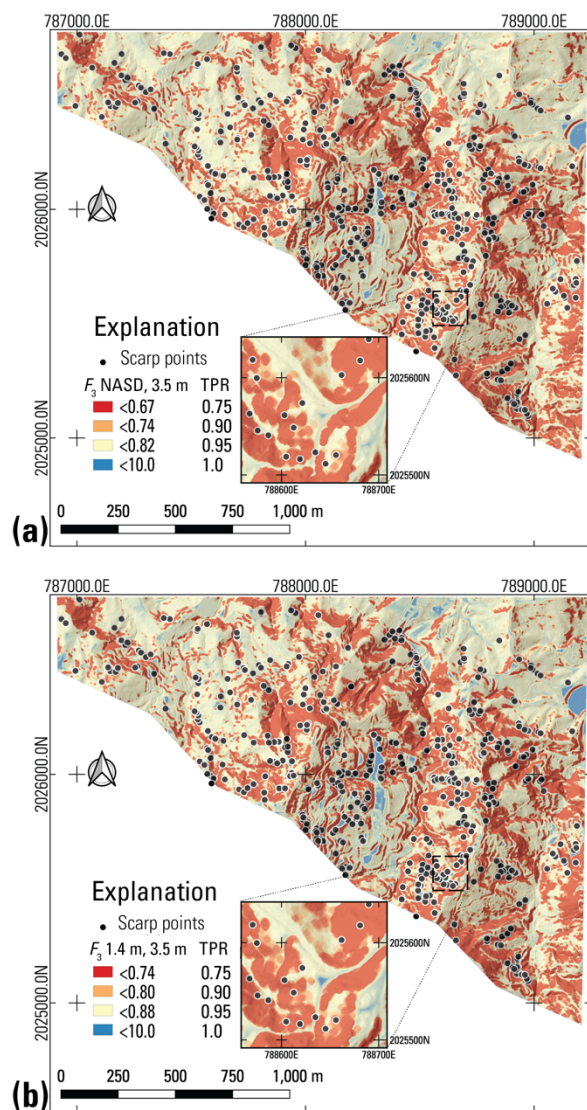
889 **Table 3. Key inputs and performance measures for factor of safety calculations based on a quasi-3D limit-equilibrium slope**  
890 **stability model ( $F_3$ ) in the Naranjito calibration area (NAR). Performance is based on minimum  $F_3$  within a 3-m radius of**  
891 **landslide scarp points mapped by Hughes et al. (2019). [Symbols and abbreviations: NASD, non-linear area and slope**  
892 **dependent soil-depth model of Pelletier and Rasmussen (2009) as modified by Baum et al. (2021); NSDA, non-linear slope**  
893 **dependent model of Pelletier and Rasmussen (2009) modified by Baum et al. (2021) to include linear area dependence;**  
894 **NDSD, non-linear slope and depth dependent model of Pelletier and Rasmussen (2009); LASD, linear area and slope**  
895 **dependent model of Ho et al. (2012);  $H_{max}$ , maximum soil depth;  $\delta_c$ , critical slope angle;  $R_d$ , diffusivity ratio;  $C_0$ , empirical**  
896 **constant used in LASD;  $c'$ , soil cohesion for effective stress;  $\phi'$ , angle of internal friction for effective stress; AUC, area**  
897 **under the curve of true-positive-rate (TPR) and false positive rate (FPR);  $\#_{HPD2PC}$ , distance from the ideal-point-perfect**  
898 **classification, (0,1), to nearest point on the TPR-FPR curve; Best  $F_3$ , 3D factor of safety at point nearest to the ideal**  
899 **point-perfect classification, (0,1), and therefore the most accurate  $F_1$  classifier of landslide versus non-landslide grid cells**  
900 **for the particular model (closer to 1.0 is better); °, degrees.]**

Soil Model	$H_{max}$ (m)	$\delta_c$ (°)	$R_d$ or $C_0$	$c'$ (kPa)	$\phi'$ (°)	Trial surface radius (m)	AUC	$\#_{HPD2PC}$	Best $F_3$	TPR at $\#_{HPD2PC}$
NASD	3.0	60	0.20	0.5	45°	3.5	0.80	0.38	0.9	0.86
NASD	3.0	60	0.20	0.5	45°	6.5	0.75	0.45	0.9	0.66
NASD	3.0	60	0.20	0.5	45°	9.5	0.71	0.50	1.0	0.86
LASD	3.0	60	0.45	0.5	45°	3.5	0.78	0.44	1.0	0.89
NDSD	3.0	60	0.10	0.5	45°	3.5	0.78	0.40	0.9	0.71
NSDA	3.0	60	0.10	0.5	45°	3.5	0.80	0.37	0.9	0.78
Constant	1.4	60	--	0.5	45°	3.5	0.92	0.23	1.0	0.94

901

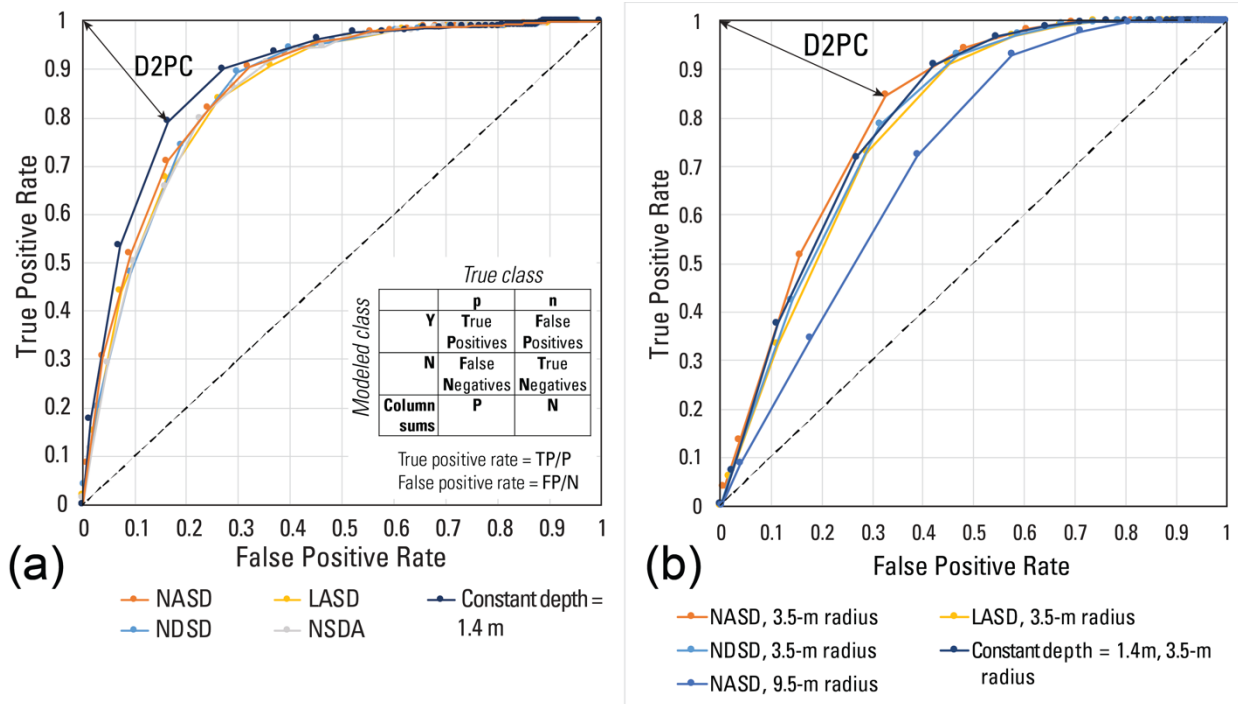
902 Tests indicated that trial surfaces having a map-view radius of 3.5 m provided more accurate estimates of susceptible  
903 areas than larger trial surfaces (6.5-m and 9.5-m radius). Other things being equal, larger trial surfaces resulted in  
904 smaller AUC and larger  $\#_{HPD2PC}$  (Table 3, Fig. 12b). The larger trial surfaces tended to widen the susceptible areas  
905 and smooth their boundaries, with the result that a larger percentage of the calibration area was classified as susceptible

906 (9.5-m radius, 85%; 6.5-m radius, 83%; 3-m radius, 78% for examples in Table 3). In addition, the 3.5-m radius  
 907 produced a trial surface close in size (7.5 – 7.9 m wide, with an area of 46 – 48 m<sup>2</sup> at the ground surface for 1-m depth  
 908 on 30° – 40° slopes) to the median horizontal areas of landslide sources mapped in NAR, 51 m<sup>2</sup>, in UTU2, 42 m<sup>2</sup>, and  
 909 in LAR2 64 m<sup>2</sup> (Fig. 3c).  
 910



911  
 912 **Figure 11. Maps of Naranjito (NAR) calibration area in volcanoclastic terrane (Fig. 1) showing quasi-3D factor of safety,**  
 913  **$F_3$ , results for the soil depth models shown in Figure 9. (a)  $F_3$  for the modified nonlinear area and slope dependent (NASD)**  
 914 **soil-depth model depicted in Fig. 9, (b)  $F_3$  for constant soil depth of 1.4 m. Inset shows details of a 150 m by 150 m area. The**  
 915 **calculation of  $F_3$  used a trial surface of 3.5-m map-view radius (Fig. 7). Topographic base derived from lidar by U.S.**  
 916 **Geological Survey (2018), scarp points from Bessette-Kirton et al. (2019c).**

917



918

919 **Figure 12. Graphs of true positive rate (TPR) versus false positive rate (FPR) for factor of safety maps in Naranjito**  
 920 **calibration area (NAR in Fig. 1a, 1c). Inset shows confusion matrix and formulas defining true positive rate and false**  
 921 **positive rate. Double-headed arrow indicates distance from ideal point to perfect classification ( $d_{TPD2PC}$ ) for the results of**  
 922 **the factor of safety with the smallest  $d_{TPD2PC}$ . (a) TPR-FPR results for 1D factor of safety ( $F_1$ ) in Fig. 10, as well as results**  
 923 **for  $F_1$  using other soil-depth models that were tested during the calibration process. (b) TPR-FPR results for quasi-3D**  
 924 **factor of safety ( $F_3$ ) in Fig. 11, as well as results for  $F_3$  using other soil depth models and one with a larger (NASD, 9.5-m**  
 925 **radius) trial surface. [Soil-depth models: LASD, linear area- and slope-dependent model (Ho et al. 2012); NASD, modified**  
 926 **nonlinear area- and slope-dependent model (modified from Pelletier and Rasmussen 2009); NDS, nonlinear depth- and**  
 927 **slope-dependent model (Pelletier and Rasmussen 2009); NSD, nonlinear slope-dependent model (Pelletier and Rasmussen**  
 928 **2009); NSDA, nonlinear slope-dependent model with linear area dependence (modified by Baum et al. 2021 from NSD**  
 929 **model of Pelletier and Rasmussen 2009)].**

930

#### 931 4.6 Susceptibility categories and predictive strength

932 Computing  $F_3$  over the combined study areas of Lares, Utuado, and Naranjito municipalities produced somewhat  
 933 different results than in the calibration areas. Calibration areas have very high landslide densities, with average density  
 934 of 182 scarps/km<sup>2</sup> at NAR. However, landslide density varies considerably across each municipality. Based on positive  
 935 correlation between low  $F_3$  and landslide scarp points mapped by Hughes et al. (2019), we established susceptibility  
 936 categories based on percentages of landslides enclosed by successive susceptibility categories as noted previously and  
 937 as shown in Table 4. Increasing density of observed landslides is consistent with increasing susceptibility. Very high  
 938 susceptibility (typically > 118 scarp points/km<sup>2</sup>) characterizes 23% of the total study area and 21%, 43%, and 45% of  
 939 the area underlain by marine volcanoclastic, submarine basalt, and granitoid rocks, respectively. Almost all karst areas  
 940 underlain by limey sediments had low susceptibility (< 2 scarp points/km<sup>2</sup>) (Baxstrom et al. 2021b). Based on the  
 941 information in Table 4, the AUC for the entire map area is 0.84, and  $d_{TPD2PC}$  is 0.34.



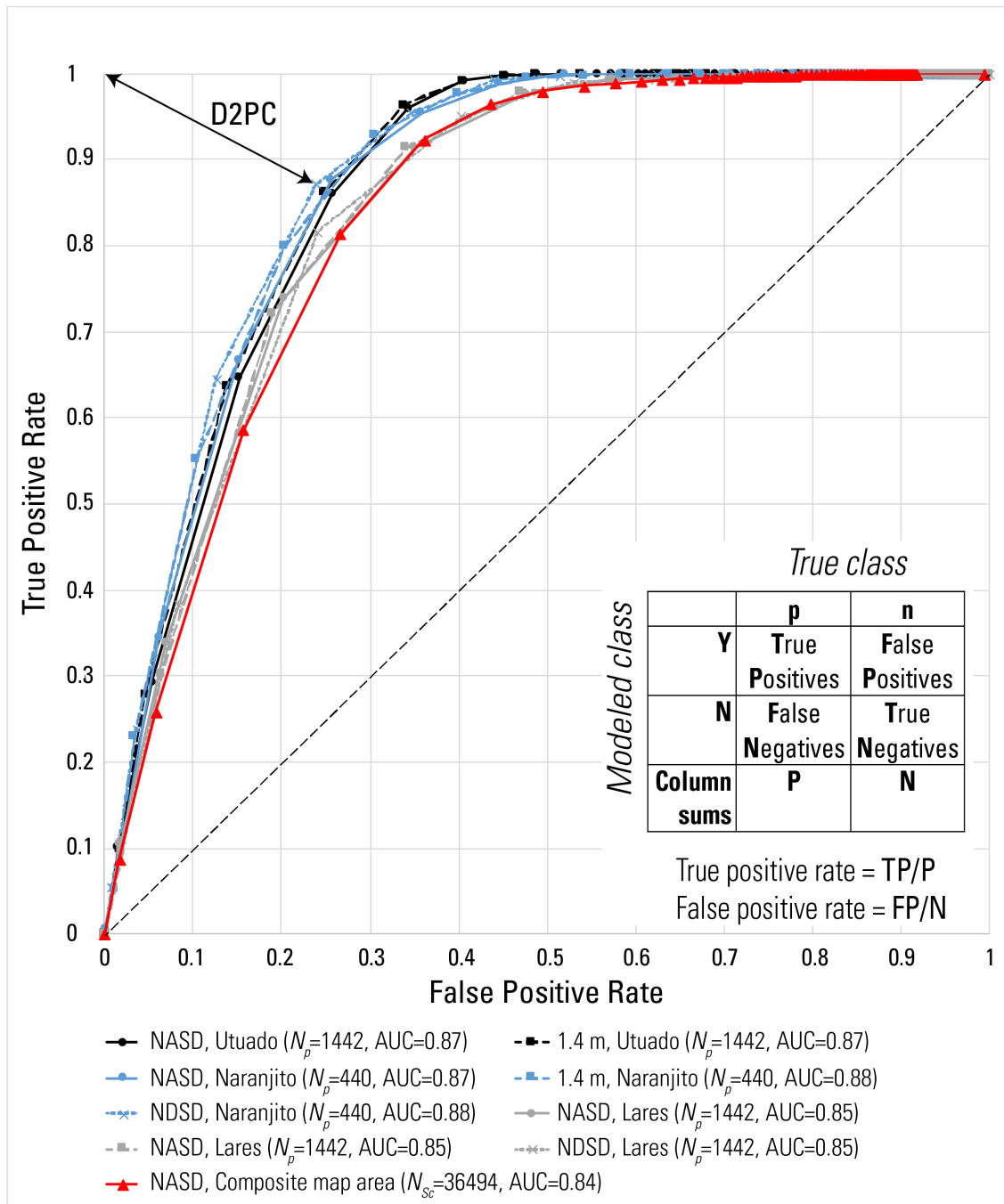
942 ~~Due to physical (subsurface conditions, ground failure mechanisms) and conceptual (parameters, models)~~  
 943 ~~uncertainties, the  $F_3$  value at the boundary between high and moderate susceptibility is slightly less than 1 (0.97, Table~~  
 944 ~~4). Although the strength parameters could be increased to achieve  $F_3 = 1.0$  at TPR = 0.90, we also wanted to keep  $F_3$~~   
 945 ~~at TPR = 0.95 relatively low while keeping  $F_3 > 1$  under dry conditions for as much area as possible. Our final model~~  
 946 ~~parameters represent a compromise between stable slopes ( $F_3 \geq 1$ ) under dry conditions and low factor of safety ( $F_3$~~   
 947  ~~$\leq 1$ ) for highly susceptible slopes under presumed wettest conditions.~~

948  
 949 Recent, detailed mapping of source areas provided an opportunity to further test performance of the pre-Hurricane  
 950 María  $F_3$  map (output from step B.5 section 3.9, Fig. 6 Fig. 4). Figure 13 shows TPR-FPR curves for the pre-Hurricane  
 951 María  $F_3$  map tested against Hurricane María landslide source polygons (Baxstrom et al. 2021a; Einbund et al. 2021a,  
 952 2021b) and against scarp points (Table 4). The AUC range, 0.85 – 0.88, is somewhat greater than obtained by testing  
 953 within a 3-m radius of the scarp points, 0.84.

954  
 955 **Table 4. Landslide susceptibility categories based on minimum value of quasi-3D factor of safety,  $F_3$ , within a 3-m radius**  
 956 **of landslide scarp points mapped by Hughes et al. (2019) for all three municipalities. For consistency,  $F_3$  thresholds below**  
 957 **are based on  $F_3$  calculated using pre-Hurricane María lidar topography and scarp locations of landslides induced by**  
 958 **Hurricane María.**

Landslide Susceptibility	$F_3$ threshold	Landslide scarp points enclosed (percent)	Landslide scarp points enclosed within increment (number)	Area within increment (km <sup>2</sup> )	Landslide points within increment (percent)	Incremental Landslide density (scarps/km <sup>2</sup> )
Very High	$\leq 0.87$	75	27370	232	75	118
High	$\leq 0.97$	90	5474	108	15	51
Moderate	$\leq 1.05$	95	1825	68	5	27
Low	$> 1.05$	100	1824	610	5	3
Total	$0 < F_3 \leq 10$	100	36493	1018	100	36

959



960  
 961 **Figure 13.** Graph of true positive rate versus false positive rate for pre-Hurricane María susceptibility models across the  
 962 study area tiles tested against head-scarp points (Hughes et al. 2019) and source polygons for Lares (Einbund et al. 2021b),  
 963 Naranjito (Baxstrom et al. 2021a), and Utuado (Einbund et al. 2021a) with confusion matrix and formulas defining true  
 964 positive rate (TPR) and false positive rate (FPR). Double-headed arrow indicates distance ~~from ideal point to perfect~~  
 965 **classification (#pD2PC)** for Naranjito source polygons and  $F_3$  computed using NDS soil depth. True positive rates are  
 966 based on minimum value of the quasi-3D factor of safety,  $F_3$ , within the mapped source polygons or within a 3-m radius of  
 967 the scarp points. Results for scarp points cover the final pre-Hurricane María susceptibility maps of Lares, Utuado, and  
 968 Naranjito municipalities. Results for the landslide source polygons cover parts of the component tiles (Fig. 1). Landslide  
 969 source mapping for Lares and Utuado (Einbund et al. 2021a, b) are near LAR and UTU (LAR2, UTU2, Fig. 1b). The graph  
 970 compares  $F_3$  performance based on the modified nonlinear area- and slope-dependent (NASD, modified from Pelletier and  
 971 Rasmussen 2009) soil-depth model and two alternates: constant depth of 1.4 m, and the nonlinear depth- and slope-  
 972 dependent soil-depth model (NDS, Pelletier and Rasmussen 2009), with strength parameters and other inputs held

973 constant. AUC denotes area under the curve of TPR versus FPR,  $N_p$  is the number of landslide source polygons, and  $N_{sc}$  is  
974 the number of scarp points.

975

## 976 5 Discussion

977 Our analyses presented in the previous section (Sect. 4.6) indicate that the landslide susceptibility assessment  
978 successfully identifies areas where high percentages of Hurricane María landslides occurred. In succeeding  
979 paragraphs, we discuss some of the strengths, limitations, and unexpected findings of our approach and results.

980 Optimum ranges of internal friction angles for all three terranes (Fig. 65) are higher than commonly reported, but  
981 consistent with measured values of  $\phi'$  for low normal stress (Likos et al. 2010). Most reported values of  $\phi'$  for soils  
982 like those in the study area range from  $17^\circ$  to  $41^\circ$  as noted previously (Sec. 3.2) and are usually based on tests at  
983 normal stress greater than 100 kPa. In contrast, samples collected at two field monitoring sites tested at low and  
984 moderate normal stresses (Smith et al. 2020) using equipment and procedures described by Likos et al. (2010) had  
985 high friction angles for low normal stress. Smith et al. (2020) reported  $\phi' = 34.8^\circ - 35.5^\circ$  ( $c' = 0 - 4.4$  kPa) for two  
986 samples tested at effective normal stress,  $\sigma'_n$ , less than 120 kPa,  $\phi' = 45.6^\circ$  for a sample tested at  $\sigma'_n \leq 30$  kPa, and  $\phi'$   
987  $= 53.9^\circ$  for another sample tested at  $\sigma'_n \leq 7$  kPa. Significantly, shear stress was considerably higher than normal stress  
988 for nearly all individual tests at  $\sigma'_n \leq 15$  kPa, and many at  $\sigma'_n \leq 30$ , consistent with  $\phi' > 45^\circ$  at low normal stress. In  
989 addition to evidence for high internal friction angles at low normal stress, which is particularly relevant to abundant  
990 thin ( $< 0.5$  m) landslides in Utuado, three other factors could contribute to stability and reduce the magnitude of  $\phi'$   
991 required to explain stability during dry conditions: (1) Soil suction measured at the sites between rainfall (Smith et al.  
992 2020) indicates that suction stress probably contributes to stability. Preliminary tests indicate that considering modest  
993 amounts of suction stress (less than a few tens of kilopascals) during dry conditions in the analysis depicted by Fig.  
994 65 shifts the cells having high TPR toward lower ranges of  $\phi'$ . For example, increasing initial suction stress by -1 kPa  
995 shifts the optimum range of  $\phi'$  to  $35^\circ - 40^\circ$  for the submarine basalt and chert landslides compared to the  $45^\circ - 50^\circ$   
996 range in Fig. 546d. (2) Root resistance also likely contributes to slope stability to depths of about 0.5 – 0.6 m. Due to  
997 high annual rainfall, vegetation in the study areas tends to be shallow-rooted so that significant root resistance would  
998 decline rapidly below about 0.4 – 1.1 m depth (Simon et al. 1990; Larsen 2012). (3) Lateral stress variation also  
999 contributes to slope stability. Even in quasi-3D limit-equilibrium as used in computing  $F_3$ , combined resistance of  
1000 neighboring grid cells (columns) and toe wedge contributes to stability and reduces the values of  $\phi'$  and (or)  $c'$  needed  
1001 to achieve stability of a potential landslide under dry conditions (Tables 2 and 3). Quantifying the contributions of  
1002 these three factors (soil suction, root resistance, and lateral stress) to slope stability could lead to greater refinement  
1003 of our approach to mapping landslide susceptibility.

1004 Our modelling workflow makes a few trade-offs to create a relatively conservative map of potential landslide sources  
1005 that accounts for uncertainties. These trade-offs are between speed and simplicity of the assessment, statistical  
1006 accuracy, and continuity of susceptibility zones. Some of the modelling steps (soil depth and  $F_3$ ) add complexity,  
1007 increase time needed to model susceptibility, and slightly reduce performance metrics (AUC and ~~HP~~D2PC) compared

1008 to  $F_1$  with constant soil depth. In exchange, soil depth and  $F_3$  create more continuous susceptibility zones, join  
1009 neighboring groups of high-susceptibility pixels, and eliminate isolated, commonly errant, pixels of high landslide  
1010 susceptibility (Fig. 10 and 11). The increased continuity of the susceptibility zones makes them easier to implement  
1011 in land use and emergency management. In addition, the potential source areas delineated on the map by the high and  
1012 very high susceptibility areas provide areas susceptible to shallow landslides for estimating potential landslide runoff  
1013 and debris-flow inundation (Brien et al. 2021). Much of the reduction in AUC for  $F_3$  results from using the minimum  
1014 factor of safety value computed for any trial landslide that includes a grid cell. Consequently, very high and high  
1015 susceptibility zones for  $F_3$  are broader than for  $F_1$  and thereby have a buffer along their edges. Nevertheless, as  
1016 indicated by various performance metrics and landslide densities in the susceptibility classes, the landslide assessment  
1017 successfully distinguishes areas having different levels of susceptibility to landslide initiation (Tables 3, 4) despite  
1018 these trade-offs.

1019 Although  $F_1$  for constant depth has slightly better performance metrics (the highest AUC and smallest ~~RMSE~~  $D2PC$ ) than  
1020  $F_1$  for any of the soil depth models calibrated to landslide source depths (Table 2, Fig. 12a) at NAR, its performance  
1021 metrics are comparable to the nonlinear soil-depth models elsewhere. Our field observations indicate that depth of  
1022 shallow, rainfall-induced landslides is well correlated to depth of mobile regolith ("soil") due to strength and  
1023 permeability contrasts at its base. Soil-depth models represent the distribution of soil depth more consistently with  
1024 field conditions than constant depth in many settings (Pelletier and Rasmussen 2009; Ho et al. 2012; Catani et al.  
1025 2010; Nicótina et al. 2011; Gomes et al. 2016; Patton et al. 2018). Performance metrics ( $ED = \sqrt{2}$ ; mean-squared error,  
1026  $MSE = \sigma_o^2$ ) indicate average depth was a poorer predictor of observed landslide depth than any of the models Tello  
1027 (2020) tested for Utuado. Despite odd differences in how the models estimate soil depth on mid-slope benches and  
1028 flat valley bottoms, the models we tested (NASD, NSDA, NDS, LASD) predict thinner soils on ridge crests and  
1029 thicker soils in hillside hollows, consistent with patterns observed in Puerto Rico and elsewhere for dissected  
1030 topography (Roering 2008). For example, mean depths of landslide sources from field mapping in Puerto Rico were  
1031 3.25 m (for concave slopes), 2.5 m (for convex slopes), 2.7 m (for planar slopes; Schulz et al. 2023). The unexpected,  
1032 good performance of  $F_1$  for constant soil depth at NAR points out limitations of soil depth models and may result in  
1033 part from widespread modifications to the landscape resulting from agriculture, road (e.g., Ramos-Scharrón et al.  
1034 2021) and building construction, and other activities. Effects of these activities may have influenced the locations of  
1035 shallow landslides sufficiently to weaken correlation between landslide location and topographic features that  
1036 influence soil depth (as at LAR and ANA, Fig. 8a). The high degree of slope modification (roads and terraces) in the  
1037 NAR calibration area is likely a determining factor in  $F_1$  performance there (Fig. 10). Identifying specific areas or  
1038 features where constant-depth  $F_1$  classifies susceptibility differently than  $F_1$  with other soil-depth models might reveal  
1039 potential improvements.

1040 Computing  $F_1$  using the modified NASD soil-depth model resulted in the areas assigned to the moderate, high, and  
1041 very high susceptibility classes being more clearly delineated with little or no loss of performance compared to using  
1042 constant depth. The susceptibility zones in the constant-depth  $F_1$  susceptibility map (Fig. 10b) are more diffuse or  
1043 fragmented (less continuous) than for the NASD soil depth (Fig. 10a) and other soil models we tested. Fragmentation  
1044 also occurred for susceptibility zones defined by slope categories (Fig. S3a). As noted previously, this improved

1045 delineation came with only a slight reduction in AUC (0.88 to 0.86) and small increase in  $\#_{\text{D2PC}}$  (0.26 to 0.30) for  
1046 NAR. When applied to the entire DEM tile covering Naranjito municipality, performance of  $F_1$  for constant depth and  
1047  $F_1$  for NASD tied with each other and with slope categories (AUC = 0.87,  $\#_{\text{D2PC}}$  = 0.29 - 0.30). As noted previously,  
1048 when checked against detailed source mapping, the performance metrics for  $F_3$  are better than when compared against  
1049 the scarp points (Fig. 13). In addition, differences in performance metrics between constant depth and the NDS  
1050 model and modified NASD model are negligible.

1051 Due to physical (subsurface conditions, ground-failure mechanisms) and conceptual (parameters, models)  
1052 uncertainties, the  $F_3$  value at the boundary between high and moderate susceptibility is slightly less than 1 (0.97, Table  
1053 4). Although the strength parameters could be increased to achieve  $F_3 = 1.0$  at TPR = 0.90, we also wanted to keep  $F_3$   
1054 at TPR = 0.95 relatively low while keeping  $F_3 > 1$  under dry conditions for as much area as possible. Our final model  
1055 parameters represent a compromise between stable slopes ( $F_3 > 1$ ) under dry conditions and low factor of safety ( $F_3$   
1056  $\leq 1$ ) for highly susceptible slopes under presumed wettest conditions.

1057 Other things being equal, the quasi-3D stability analysis,  $F_3$ , has a somewhat smaller AUC and larger  $\#_{\text{D2PC}}$ ,  
1058 compared to  $F_1$  (Tables 2 and 3), but improves the final map. The improvements are better separation between the  
1059 different susceptibility classes (Fig. 10 and 11) and a slightly more conservative map compared to  $F_1$ , which is helpful  
1060 for life-safety based land use planning and emergency response scenarios. With AUC=0.80 and  $\#_{\text{D2PC}}$ =0.38 for  $F_3$   
1061 based on the modified NASD soil-depth and 3.5 m radius for the trial surface (Table 3),  $F_3$  successfully identifies  
1062 potential landslide sources at NAR. For the entire map area, the AUC (0.84) and  $\#_{\text{D2PC}}$  (0.33) scores are slightly  
1063 better (Table 4, Fig. 13), due in part to the large area of low landslide susceptibility that is underlain by limey sediments  
1064 and characterized by cone karst. By considering slope stability at the scale of representative landslide sources (median  
1065 area, Fig. 3c),  $F_3$  eliminates isolated grid cells and tiny clusters of 2 – 4 cells that likely are classified incorrectly by  
1066  $F_1$  as highly or very highly susceptible due to locally steep slopes at the pixel scale (1 m). Such isolated cells and  
1067 clusters could be eliminated after analysis, but boundaries of susceptible areas would remain somewhat ragged. In  
1068 contrast our approach provides an objective method for eliminating the isolated pixels and smoothing the boundaries.  
1069  $F_3$  bridges gaps between neighboring areas of low  $F_1$  and thereby maps susceptible areas that are more continuous and  
1070 with smoother, more definite boundaries than  $F_1$ . Thus,  $F_3$  further improves delineation of susceptible areas beyond  
1071 improvements achieved by using the modified NASD soil-depth model with  $F_1$ . Maps having continuous, clearly  
1072 delineated areas assigned to each susceptibility class such as those obtained by using  $F_3$  reduce guesswork in making  
1073 land use and emergency management decisions by eliminating the ragged, transitional boundaries obtained with  $F_1$ .  
1074 For example, to compare the insets in Figs. 10 and 11 to each other as well as slope categories (Fig. S3a) and  $F_3$  based  
1075 on the NDS soil-depth model (Fig. S3d), see Fig. S3b, c, e and f. Alternately continuous, clear delineation can be  
1076 achieved by aggregating raster maps to slope units (Alvioli et al. 2016; Woodard et al. 2024).-Nevertheless, an added  
1077 benefit of using  $F_3$  is creation of Wellwell-defined potential landslide source areas ~~also that~~ allow estimation of areas  
1078 susceptible to potential downslope runoff and downstream inundation (Brien et al. 2021). Performance metrics for  $F_3$   
1079 considering detailed source mapping (Fig. 13) are sufficiently high ( $0.85 \leq \text{AUC} \leq 0.88$ ) to consider  $F_3$  a very  
1080 successful indicator of landslide susceptibility in our study area. As the basis for our final susceptibility maps, we  
1081 selected the  $F_3$  map derived from the modified NASD soil depth model (Fig. 11a) because of its high AUC combined

1082 with its well-defined source areas and the realistic modeled soil depths for estimating potential landslide volumes.  
1083 Visual comparison indicates only slight differences between  $F_3$  maps based on pre-event and post-event DEMs (Fig.  
1084 S4). Model input parameters for the final maps are summarized in Supplemental Figures S1 and S2.

1085 The susceptibility analysis portrayed in Fig. 11 and our final maps (Supplemental Figures S1 and S2) are valid  
1086 throughout the three municipalities despite the variable density of Hurricane María landslides throughout the map area  
1087 (Bessette-Kirton et al. 2017; Hughes et al. 2019) and within each susceptibility class. High landslide density generally  
1088 corresponds to low  $F_3$  (Table 4); however, not all susceptible areas were equally affected by Hurricane María. Thus,  
1089 although some areas of low  $F_3$ , particularly in Naranjito, had low landslide density, the low density does not invalidate  
1090 the susceptibility assessment of the potential for future landslides. Factors such as antecedent soil moisture are known  
1091 to have affected the density of landslides induced by Hurricane María (Bessette-Kirton et al. 2019a) and were  
1092 addressed in the statistically based island-wide landslide susceptibility assessment of Hughes and Schulz (2020a).  
1093 Notably Naranjito had much lower root-zone soil moisture immediately after the hurricane than Utuado and Lares  
1094 (Fig. 26 of Hughes and Schulz 2020a). Variable rainfall intensity and duration are also known to affect landslide  
1095 response of susceptible areas (Larsen and Simon 1993; Pando et al. 2005). Intensity and duration are known to have  
1096 varied during Hurricane María, causing further differences in landslide density. Our assessment considered fully  
1097 saturated conditions with the water table at the ground surface to depict likely wettest-case soil moisture effects,  
1098 including high antecedent soil wetness, as well as high intensity and long-duration rainfall. Thus, it was not necessary  
1099 to specifically model antecedent soil moisture conditions. Less-severe conditions may produce landslides in the same  
1100 general areas as predicted by our assessment, however, in lower numbers than observed following Hurricane María.

1101 Setting the boundaries between susceptibility classes based on  $F_1$  or  $F_3$  corresponding to specific values of TPR rather  
1102 than setting boundaries based on theoretical values of  $F_1$  or  $F_3$  (such as  $F_3 = 1.0$ ) reduces uncertainty and ensures  
1103 correspondence between landslide density and degree of landslide susceptibility. Soil, saprolite, and bedrock are  
1104 inherently heterogenous. Their hydraulic and strength properties (and corresponding parameters) vary spatially at all  
1105 scales (Terzaghi et al. 1996). Other studies have applied probabilistic approaches and sensitivity analyses have been  
1106 applied successfully to address parameter uncertainty and improve accuracy of physically based modelling of landslide  
1107 susceptibility (Raia et al. 2014; Zieher et al. 2017; Canli et al. 2018). Many parameter combinations ( $c'$  and  $\phi'$ ) can  
1108 achieve similar levels of predictive accuracy in computing  $F_1$  for observed distributions of landslide slope and depth  
1109 (Baum et al. 2019; Baum 2021). These and other uncertainties such as transient pore-water pressures, subsurface  
1110 features, heterogeneity, and other factors, weaken the link between theoretical values of  $F_1$  or  $F_3$  and estimated  
1111 likelihood of failure for site-specific cases when applying limit-equilibrium slope stability analysis over wide areas.

1112 On the other hand, maps classified based on TPR have a strong link to susceptibility. Such maps are readily comparable  
1113 to each other when  $F_1$  or  $F_3$  values are computed with different parameters, as they show like outcomes (areas that  
1114 capture 75%, 90% and 95% of observed landslides in this study). Comparing like outcomes focuses on differences  
1115 and uncertainties that affect the quality of the susceptibility assessment that might be masked by comparing the maps  
1116 when classified using the same  $F_1$  or  $F_3$  values. In this study, low values of  $F_1$  and  $F_3$  correspond to high observed  
1117 Hurricane María landslide density (Table 4), as would be expected. The selected boundaries for susceptibility classes  
1118 ensure a meaningful distinction between average landslide density in the successive classes (Table 4).

1119 The susceptibility map correctly predicts locations of most landslides that are deeper than 3 m, despite the maximum  
1120 modeled soil depth of 3 m more typical of shallow landslides. Ten of the landslides summarized in Fig. 3e are deeper  
1121 than 3 m. Most (nine) are within the Naranjito tile (Fig. 1), and the other is in Lares. The mapped point on each  
1122 landslide headscarp and adjoining or surrounding slope was within the high or very high susceptibility zone for seven  
1123 of the ten deep landslides. The other three had head scarps on a gently sloping area (road or pad) that was set back a  
1124 few meters from the steep slope, but the adjoining slope with the landslide body was within the high and very high  
1125 susceptibility zones. Although the predicted locations might be right for the wrong reason (predicting a shallow  
1126 translational landslide rather than a deeper, translational, or rotational landslide), it is nevertheless encouraging that  
1127 the locations of even the deep landslides are identified for the sake of hazard assessment and planning. This probably  
1128 occurred because the deep landslides occurred well within the same slope range as other mapped landslides (Fig. 3,  
1129 4).

1130 Despite the simplicity of soil and water parameters, the maps successfully predicted the effects from Hurricane María.  
1131 Calibrating with field data from the small calibration areas (ANA, LAR, UTU, and NAR, Fig. 1) and then testing with  
1132 the island-wide scarp points (Hughes et al. 2019) confirmed the successes of our approach (Supplemental Figures S1  
1133 and S2). Testing with detailed landslide source maps (Baxstrom et al. 2021a; Einbund et al. 2021a, 2021b) strengthens  
1134 our results even though they cover only a fraction of the study area.

1135 The workflow outlined in Fig. 4 can be simplified in areas where few data are available. An accurate digital  
1136 elevation model and accurate landslide inventory with measurements of source area size, depth, and slope (Fig. 3) are  
1137 the most critical data for a landslide susceptibility analysis. Strength parameter ranges can be estimated from landslide  
1138 source depth and slope (Fig. 54, 56). Soil model calibration can be bypassed by assuming constant average landslide  
1139 source depth. Strength parameters can then be refined using the procedure described in Sect. 3.5. Alternately a soil  
1140 model and strength parameters can be calibrated simultaneously to the inventory as we did for the NAR calibration  
1141 area. Calculation of pressure head,  $F_1$  and  $F_3$  can then proceed as outlined in Sect. 3.4.2, 3.4.3, 3.4.4, and 3.9, followed  
1142 by validation and evaluation (Sect. 3.11). Compared to a map based on the simplest of landslide susceptibility  
1143 approach, slope ranges with its ragged, fragmented susceptibility zones, our procedure creates cohesive landslide  
1144 susceptibility zones that have smooth, buffered boundaries with only a slightly lower AUC score (0.84) than for slope  
1145 (0.87) across the entire study area.

## 1146 **6 Conclusions**

1147 We defined a workflow for assessing landslide susceptibility using multiple modelling stages and successfully applied  
1148 it using high-resolution (1-m) topography over a large (about 1000 km<sup>2</sup>) geographic area in the central mountains of  
1149 Puerto Rico (Fig. 1). The workflow includes modelling soil depth, pressure head, and limit-equilibrium slope stability  
1150 (Fig. 4). Although calibration studies showed that assuming constant average soil depth as input for 1D (infinite-  
1151 slope) factor of safety against landsliding,  $F_1$ , gave the best performance metrics in a 2.5 km<sup>2</sup> calibration area, use of  
1152 a soil-depth model more clearly delineated areas susceptible to landslide initiation with only a modest reduction in the  
1153 AUC from 0.88 to 0.86. Using a quasi-3D limit-equilibrium slope stability analysis, the factor of safety,  $F_3$ , further  
1154 refined the susceptibility assessment by more clearly delineating boundaries between the different susceptibility

1155 classes and by assessing stability at the scale of the observed median-sized landslides. Despite further reduction in  
1156 AUC to 0.80 for the NAR calibration area, the map based on  $F_3$  is more readily usable in certain applications than a  
1157 map based on  $F_1$ , and it still performs well as a classifier of landslide susceptibility. Performance metrics for the  $F_3$   
1158 map of the entire ~1000 km<sup>2</sup> study area, AUC = 0.84 and  $d_{AP}D2PC = 0.34$ , are slightly better than results at the NAR  
1159 calibration area. Performance measured against detailed source mapping of selected areas is even better:  $0.85 \leq AUC$   
1160  $\leq 0.88$  and  $0.27 \leq d_{AP}D2PC \leq 0.33$ . These metrics indicate the map is suitable for planning, regulation, and emergency  
1161 preparedness decisions at the municipality scale. The map may also be used to assess hazards, such as ground collapse,  
1162 resulting from landslide initiation. Source area delineation as shown on maps may also be used for defining landslide  
1163 starting locations and surface area needed to assess areas with potential downslope movement of sediment mobilized  
1164 by future landslides.

#### 1165 **Code availability**

1166 Computer codes used in this study are available from the U.S. Geological Survey software repository as follows:  
1167 TRIGRS 2.1, <https://doi.org/10.5066/F7M044QS>; REGOLITH, <https://doi.org/10.5066/P9U2RDWJ>; and Slabs3D,  
1168 <https://doi.org/10.5066/P9G4I8IU>.

#### 1169 **Data availability**

1170 The pre-event (2015) and post-event (2018) lidar topographic data used in this study are available through the National  
1171 Map at <https://apps.nationalmap.gov/lidar-explorer/#/>. Soil mapping databases used to estimate soil properties are  
1172 available from the Natural Resources Conservation Service at [https://www.nrcs.usda.gov/resources/data-and-](https://www.nrcs.usda.gov/resources/data-and-reports/web-soil-survey)  
1173 [reports/web-soil-survey](https://www.nrcs.usda.gov/resources/data-and-reports/web-soil-survey). Other data are available from the U.S. Geological Survey ScienceBase digital repository as  
1174 follows: Summaries of geotechnical data, <https://doi.org/10.5066/P9UXTQ4B>; model input and output raster grids  
1175 and model parameter input files used to produce the large maps (Supplemental Figures S1 and S2),  
1176 <https://doi.org/10.5066/P9C1U0LP>; Landslide head scarp points, <https://doi.org/10.5066/P9BVMD74>; landslide  
1177 polygons, <https://doi.org/10.5066/F7JD4VRF>, <https://doi.org/10.5066/P9GBGA4I>,  
1178 <https://doi.org/10.5066/P9YYU7W1>, <https://doi.org/10.5066/P9EASZZ7>, and <https://doi.org/10.5066/P9ZNUR1P>.

#### 1179 **Author contribution**

1180 RB, WS, MR and DB planned the study. WS managed the project. MT carried out model calibrations. RB developed  
1181 the model code, carried out the simulations, and computed the model performance statistics. DB, WS, MR, MT, and  
1182 RB analyzed the data. RB wrote the manuscript draft; DB, MR, and WS reviewed and edited the manuscript.

#### 1183 **Competing interests**

1184 The authors declare that they have no conflict of interest.



1185 **Disclaimer**

1186 Any use of trade, firm, or product names is for descriptive purposes only and does not imply endorsement by the U.S.  
1187 Government.

1188 **Acknowledgements**

1189 Adrian Lewis compiled and summarized geotechnical data from published and publicly available sources. Mason  
1190 Einbund extracted statistics on landslide true positives and density from pre-Hurricane María factor of safety grids.  
1191 Emily Bedinger generated flow-accumulation raster grids and edited the model output grids to remove edge effects.  
1192 Brian Collins and Lauren Schaefer reviewed an earlier version of this manuscript. This work was supported in part by  
1193 the Additional Supplemental Appropriations for Disaster Relief Requirements Act, 2018 (P.L. 115-123)

1194 **References**

1195 Aaron, J., McDougall, S., Moore, J.R., Coe, J.A., and Hungr, O.: The role of initial coherence and path materials in  
1196 the dynamics of three rock avalanche case histories, *Geoenvironmental Disasters*, 4, 5. [https://doi.org/10.1186/s40677-](https://doi.org/10.1186/s40677-017-0070-4)  
1197 [017-0070-4](https://doi.org/10.1186/s40677-017-0070-4), 2017.

1198 Alvioli, M., and Baum, R.L.: Parallelization of the TRIGRS model for rainfall-induced landslides using the message  
1199 passing interface. *Environ. Modell. Softw.* 81, 122–135. <https://doi.org/10.1016/j.envsoft.2016.04.002>, 2016.

1200 [Alvioli, M., Marchesini, I., Reichenbach, P., Rossi, M., Ardizzone, F., Fiorucci, F., and Guzzetti, F.: Automatic](#)  
1201 [delineation of geomorphological slope units with r.slopeunits v1.0 and their optimization for landslide susceptibility](#)  
1202 [modeling, \*Geosci. Model Dev.\*, 9, 3975–3991, <https://doi.org/10.5194/gmd-9-3975-2016>, 2016.](#)

1203 [Arnone, E., Noto, L., Lepore, C., Bras, R.: Physically-based and distributed approach to analyze rainfall-triggered](#)  
1204 [landslides at watershed scale, \*Geomorphology\*, 133, 121–131, <https://doi.org/10.1016/j.geomorph.2011.03.019>, 2011.](#)

1205 ASTM International: D2487-17e1, Standard Practice for Classification of Soils for Engineering Purposes (Unified  
1206 Soil Classification System), <https://doi.org/10.1520/D2487-17E01>, 2020.

1207 Baum, R.L.: Rapid sensitivity analysis for reducing uncertainty in landslide hazard assessments, in: *Understanding*  
1208 *and Reducing Landslide Disaster Risk*, edited by: Guzzetti, F., Mihalić Arbanas, S., Reichenbach, P., Sassa, K.,  
1209 Bobrowsky, P.T., and Takara, K., Springer, Cham, Switzerland, 329–335, [https://doi.org/10.1007/978-3-030-60227-](https://doi.org/10.1007/978-3-030-60227-7_37)  
1210 [7\\_37](https://doi.org/10.1007/978-3-030-60227-7_37), 2021.

1211 Baum, R.L.: Slabs3D—A Fortran 95 program for analyzing potential shallow landslides in a digital landscape, U.S.  
1212 Geol. Surv. software release [code], <https://doi.org/10.5066/P9G4I8IU>, 2023.

1213 Baum, R.L., and Lewis, A.C.: Engineering soil classification and geotechnical measurements in Lares, Naranjito, and  
1214 Utuado, Puerto Rico: U.S. Geol. Surv. data release [data set], <https://doi.org/10.5066/P9UXTQ4B>, 2023.

1215 Baum, R.L., Brien, D.L., Reid, M.E., Schulz, W.H., Tello, M.J., and Bedinger, E.C.: Model input and output data  
1216 covering Lares Municipio, Utuado Municipio, and Naranjito Municipio, Puerto Rico, for landslide initiation  
1217 susceptibility assessment after Hurricane Maria: U.S. Geol. Surv. data release [data set],  
1218 <https://doi.org/10.5066/P9C1U0LP>, 2023.

1219 Baum, R.L., Savage, W.Z., and Godt, J.W.: TRIGRS—A Fortran program for transient rainfall infiltration and grid-  
1220 based regional slope-stability analysis, version 2.0, U.S. Geol. Surv. Open-File Report 2008-1159, 75 pp.  
1221 <https://doi.org/10.3133/ofr20081159>, 2008.

1222 Baum, R.L., Godt, J.W., and Savage, W.Z.: Estimating the timing and location of shallow rainfall-induced landslides  
1223 using a model for transient, unsaturated infiltration. *Journal of Geophysical Research: Earth Surface*, 115(F3), F03013.  
1224 <https://doi.org/10.1029/2009JF001321>, 2010.

1225 Baum, R.L., Godt, J.W., Coe, J.A., and Reid, M.E.: Assessment of shallow landslide potential using 1D and 3D slope  
1226 stability analysis, in: *Landslides and Engineered Slopes: Protecting Society through Improved Understanding*, edited  
1227 by: Eberhardt, E., Froese, C., Turner, A.K., and Leroueil, S., Taylor & Francis Group, London, pp. 1667–1672, ISBN  
1228 978-0-415-62123-6, 2012.

1229 Baum, R.L., Schulz, W.H., Brien, D.L., Burns, W.L., Reid, M.E., and Godt, J.W.: Progress in regional landslide hazard  
1230 assessment—Examples from the USA, in: *Landslide Science for a Safer Geoenvironment*, edited by: Sassa, K.,  
1231 Canuti, P., and Yin, Y., Springer, Cham, Switzerland, pp. 21–36. [https://doi.org/10.1007/978-3-319-04999-1\\_2](https://doi.org/10.1007/978-3-319-04999-1_2), 2014.

1232 Baum, R.L., Cerovski-Darriau, C., Schulz, W.H., Bessette-Kirton, E., Coe, J.A., Smith, J.B., and Smoczyk, G.M.:  
1233 Variability of hurricane María debris-flow source areas in Puerto Rico—Implications for hazard assessment, AGU  
1234 Fall Meeting, Washington, DC 2018, NH14A-02, <https://agu.confex.com/agu/fm18/meetingapp.cgi/Paper/412740>,  
1235 2018.

1236 Baum, R.L., Scheevel, C.R., and Jones, E.S.: Constraining parameter uncertainty in modeling debris-flow initiation  
1237 during the September 2013 Colorado Front Range storm, in: *Debris-flow Hazards Mitigation: Mechanics, Monitoring,*  
1238 *Modeling, and Assessment*, edited by: Kean, J.W., Coe, J.A., Santi, P.M., and Guillen, B.K., Association of  
1239 Environmental and Engineering, Brunswick, Ohio, pp. 249–256, <https://doi.org/10.25676/11124/173212>, 2019.

1240 Baum, R.L., Bedinger, E.C., and Tello, M.J.: REGOLITH--A Fortran 95 program for estimating soil mantle thickness  
1241 in a digital landscape for landslide and debris-flow hazard assessment, U.S. Geol. Surv. software release [code],  
1242 <https://doi.org/10.5066/P9U2RDWJ>, 2021.

1243 Bawiec, W.J.: Geologic terranes of Puerto Rico, in: *Geology, geochemistry, geophysics, mineral occurrences, and*  
1244 *mineral resource assessment for the commonwealth of Puerto Rico*, edited by: Bawiec W.J., U.S. Geol. Surv. Open-  
1245 File Rep. 98–38. <https://doi.org/10.3133/ofr9838>, 1998.

1246 Baxstrom, K.W., Einbund, M.M., and Schulz, W.H.: Map data from landslides triggered by Hurricane María in a  
1247 section of Naranjito, Puerto Rico, U.S. Geol. Surv. data release [data set], <https://doi.org/10.5066/P9GBGA4I>, 2021a.

1248 Baxstrom, K.W., Einbund, M.M., and Schulz, W.H.: Map data from landslides triggered by Hurricane María in the  
1249 greater karst region of northwest Puerto Rico, U.S. Geol. Surv. data release [data set],  
1250 <https://doi.org/10.5066/P9YYU7W1>, 2021b.

1251 Begueria, S.: Validation and evaluation of predictive models in hazard assessment and risk management. *Nat. Hazards*,  
1252 37, 315–329. <https://doi.org/10.1007/s11069-005-5182-6>, 2006.

1253 Benda, L., Miller, D., Andras, K., Bigelow, P., Reeves, G., and Michael, D.: NetMap: A new tool in support of  
1254 watershed science and resource management, *Forest Sci.*, 53(2), 206-219.  
1255 <https://doi.org/10.1093/forestscience/53.2.206>, 2007.

1256 Bessette-Kirton, E.K., Coe, J.A., Godt, J.W., Kean, J.W., Rengers, F.K., Schulz, W.H., Baum, R.L., Jones, E.S., and  
1257 Staley, D.M.: Map data showing concentration of landslides caused by hurricane María in Puerto Rico. U.S. Geol.  
1258 Surv. data release [data set], <https://doi.org/10.5066/F7JD4VRF>, 2017.

1259 Bessette-Kirton, E.K., Cerovski-Darriau, C., Schulz, W.H., Coe, J.A., Kean, J.W., Godt, J.W., Thomas, M.A., and  
1260 Hughes, K.S.: Landslides triggered by Hurricane María: Assessment of an extreme event in Puerto Rico, *GSA Today*,  
1261 29, 4–10. <https://doi.org/10.1130/GSATG383A.1>, 2019a.

1262 Bessette-Kirton, E.K., Kean, J.W., Coe, J.A., Rengers, F.K., and Staley, D.M.: An evaluation of debris-flow runout  
1263 model accuracy and complexity in Montecito, California: Towards a framework for regional inundation-hazard  
1264 forecasting, in: *Debris-flow Hazards Mitigation: Mechanics, Monitoring, Modeling, and Assessment*, edited by: Kean,  
1265 J.W., Coe, J.A., Santi, P.M., Guillen, B.K., Association of Environmental and Engineering Geologists, Brunswick,  
1266 Ohio, pp. 257–264. <https://doi.org/10.25676/11124/173211>, 2019b.

1267 Bessette-Kirton, E.K., Coe, J.A., Kelly, M.A., Cerovski-Darriau, C., and Schulz, W.H.: Map data from landslides  
1268 triggered by Hurricane María in four study areas of Puerto Rico. U.S. Geol. Surv. data release [data set].  
1269 <https://doi.org/10.5066/P9OW4SLX>, 2019c.

1270 Bessette-Kirton, E.K., Coe, J.A., Schulz, W.H., Cerovski-Darriau, C., and Einbund, M.M.: Mobility characteristics of  
1271 debris slides and flows triggered by Hurricane María in Puerto Rico, *Landslides* 17, 2795–2809,  
1272 <https://doi.org/10.1007/s10346-020-01445-z>, 2020.

1273 Brien, D.L., Reid, M.E., Cronkite-Ratcliff, C., and Perkins, J.P.: Portraying runout and inundation from hurricane-  
1274 induced landslides in Puerto Rico, *Geological Society of America Abstracts with Programs*. 53(6), 85-4,  
1275 <https://doi.org/10.1130/abs/2021AM-368632>, 2021.

1276 Catani, F., Segoni, S., and Falorni, G.: An empirical geomorphology-based approach to the spatial prediction of soil  
1277 thickness at catchment scale, *Water Resour. Res.*, 46(5), W05508, <https://doi.org/10.1029/2008WR007450>, 2010.

1278 Canli, E., Mergili, M., Thiebes, B., and Glade, T.: Probabilistic landslide ensemble prediction systems: Lessons to be  
1279 learned from hydrology, *Nat. Hazard. Earth Sys.*, 18(8), 2183–2202, <https://doi.org/10.5194/nhess-18-2183-2018>,  
1280 2018.

1281 Carrara, A., Guzzetti, F., Cardinali, M., and Reichenbach, P.: Use of GIS technology in the prediction and monitoring  
1282 of landslide hazard, *Nat. Hazards*, 20, 117–135, <https://doi.org/10.1023/A:1008097111310>, 1999.

1283 Chung, C.F., and Fabbri, A.G.: Validation of spatial prediction models for landslide hazard mapping, *Nat. Hazards*,  
1284 30, 451–472, <https://doi.org/10.1023/B:NHAZ.0000007172.62651.2b>, 2003.

1285 [DeRose, R.C., Trustrum, N.A., and Blaschke, P.M.: Geomorphic change implied by regolith-slope relationships on](https://doi.org/10.1016/0341-8162(91)90051-X)  
1286 [steep land hillslopes, Taranaki, New Zealand, \*Catena\*, 18, 489-514, \[https://doi.org/10.1016/0341-8162\\(91\\)90051-X\]\(https://doi.org/10.1016/0341-8162\(91\)90051-X\),](https://doi.org/10.1016/0341-8162(91)90051-X)  
1287 [1991.](https://doi.org/10.1016/0341-8162(91)90051-X)

1288 Einbund, M.M., Baxstrom, K.S., and Schulz, W.H.: Map data from landslides triggered by Hurricane María in four  
1289 study areas in the Utuado municipality, Puerto Rico, U.S. Geol. Surv. data release [data set],  
1290 <https://doi.org/10.5066/P9ZNUR1P>, 2021a.

1291 Einbund, M.M., Baxstrom, K.S., and Schulz, W.H.: Map data from landslides triggered by Hurricane María in four  
1292 study areas in the Lares municipality, Puerto Rico. U.S. Geol. Surv. data release [data set],  
1293 <https://doi.org/10.5066/P9EASZZ7>, 2021b.

1294 Ellen, S.D., Mark, R.K., Cannon, S.H., and Knifong, D.L.: Map of debris-flow hazard in the Honolulu District of  
1295 Oahu, Hawaii, U.S. Geol. Surv. Open-File Rep. 93-213, 28 pp., <https://doi.org/10.3133/ofr93213>, 1993.

1296 Fan, L., Lehmann, P., McArdeell, B., and Or, D.: Linking rainfall-induced landslides with debris flows runout patterns  
1297 towards catchment scale hazard assessment, *Geomorphology* 280, 1-15.  
1298 <https://doi.org/10.1016/j.geomorph.2016.10.007>, 2017.

1299 Fawcett, T.: An introduction to ROC analysis, *Pattern Recogn. Lett.*, 27(8), 861–874,  
1300 <https://doi.org/10.1016/j.patrec.2005.10.010>, 2006.

1301 [Formetta, G., Capparelli, G., and Versace, P.: Evaluating performance of simplified physically based models for](#)  
1302 [shallow landslide susceptibility, \*Hydrol. Earth Syst. Sci.\*, 20, 4585–4603, <https://doi.org/10.5194/hess-20-4585-2016>,](#)  
1303 [2016.](#)

1304 George, D.L., and Iverson, R.M.: A depth-averaged debris-flow model that includes the effects of evolving dilatancy:  
1305 2. Numerical predictions and experimental tests, *P. Roy. Soc. A-Math. Phys.*, 470(2170), 20130820,  
1306 <https://doi.org/10.1098/rspa.2013.0820>, 2014.

1307 Godt, J.W., Schulz, W.H., Baum, R.L., and Savage, W.Z.: Modeling rainfall conditions for shallow landsliding in  
1308 Seattle, Washington, in: *Landslides and Engineering Geology of the Seattle, Washington, Area*, edited by: Baum,  
1309 R.L., Godt, J.W., Highland, L.M., Geological Society of America, Boulder, Colorado, 137–152,  
1310 [https://doi.org/10.1130/2008.4020\(08\)](https://doi.org/10.1130/2008.4020(08)), 2008a.

1311 [Godt, J.W., Baum, R.L., Savage, W.Z., Salciarini, D., Schulz, W.H., and Harp, E. L.: Transient deterministic shallow](#)  
1312 [landslide modeling: Requirements for susceptibility and hazard assessments in a GIS framework, \*Eng. Geol.\*, 102,](#)  
1313 [214–226, <https://doi.org/10.1016/j.enggeo.2008.03.019>, 2008b.](#)

1314 Gomes, G.J.C., Vrugt, J.A., and Vargas, Jr., E.A.: Toward improved prediction of the bedrock depth underneath  
1315 hillslopes: Bayesian inference of the bottom-up control hypothesis using high-resolution topographic data, *Water*  
1316 *Resour. Res.*, 52(4), 3085–3112, <https://doi.org/10.1002/2015WR018147>, 2016.

1317 Gupta, H.V., Kling, H., Yilmaz, K.K., and Martinez, G.F.: Decomposition of the mean squared error and NSE  
1318 performance criteria: Implications for improving hydrological modeling. *J. Hydrol.*, 377(1-2), 80–91.  
1319 <https://doi.org/10.1016/j.jhydrol.2009.08.003>, 2009.

1320 [Heidemann, H.K.: Lidar base specification \(ver. 1.3, February 2018\), U.S. Geological Survey Techniques and](#)  
1321 [Methods, 11, B4, 101 p., <https://doi.org/10.3133/tm11b4>, 2018.](#)

1322 Ho, J.-Y., Lee, K.T., Chang, T.-C., Wang, Z.-Y., and Liao, Y.-H.: Influences of spatial distribution of soil thickness  
1323 on shallow landslide prediction. *Eng. Geol.*, 124, 38–46. <https://doi.org/10.1016/j.enggeo.2011.09.013>, 2012.

1324 Hovland, H.J.: Three-dimensional slope stability analysis method. *J. Geotech. Eng.-ASCE*, 103(GT9), 971–986.  
1325 <https://doi.org/10.1061/AJGEB6.0000493>, 1977.

1326 Hsu, Y.C., and Liu, K.F.: Combining TRIGRS and DEBRIS-2D models for the simulation of a rainfall infiltration  
1327 induced shallow landslide and subsequent debris flow, *Water*, 11(5), 890, <https://doi.org/10.3390/w11050890>, 2019.

1328 Hughes, K.S., Bayouth-García, D., Martínez-Milian, G.O., Schulz, W.H., and Baum, R.L.: Map of slope-failure  
1329 locations in Puerto Rico after Hurricane María. U.S. Geol. Surv. data release [data set],  
1330 <https://doi.org/10.5066/P9BVMD74>, 2019.

1331 Hughes, K.S., and Schulz, W.H.: Map depicting susceptibility to landslides triggered by intense rainfall, Puerto Rico,  
1332 U.S. Geol. Surv. Open-File Rep. 2020–1022, 91 pp., 1 plate, scale 1:150,000. <https://doi.org/10.3133/ofr20201022>,  
1333 2020a.

1334 Hughes, K.S., Schulz, W.H.: Results from frequency-ratio analyses of soil classification and land use related to  
1335 landslide locations in Puerto Rico following Hurricane María. U.S. Geol. Surv. data release [data set],  
1336 <https://doi.org/10.5066/P9VK2FAL>, 2020b.

1337 Hungr, O., Salgado, F.M., and Byrne, P.M.: Evaluation of a three-dimensional method of slope-stability analysis, *Can.*  
1338 *Geotech. J.*, 26(4), 679–686, <https://doi.org/10.1139/t89-079>, 1989.

1339 Iverson, R.M.: Landslide triggering by rain infiltration, *Water Resour. Res.*, 36(7), 1897–1910,  
1340 <https://doi.org/10.1029/2000WR900090>, 2000.

1341 Jibson, R.W.: Debris flows in southern Puerto Rico, in: *Landslide processes of the eastern United States and Puerto*  
1342 *Rico*, edited by: Schultz A.P., and Jibson R.W., *Geol. S. Am. S.*, 236, 29–55, <https://doi.org/10.1130/SPE236-p29>,  
1343 1989.

1344 Jolly, W.T., Lidiak, E.G., Dickin, A.P., and Wu, T.-W.: Geochemical diversity of Mesozoic island arc tectonic blocks  
1345 in eastern Puerto Rico, in: *Tectonics and Geochemistry of the Northeastern Caribbean*, edited by: Likiak, E.G., Larue,  
1346 D.K., *Geol. S. Am. S.*, 322, 67–98, <https://doi.org/10.1130/0-8137-2322-1.67>, 1998.

1347 Lambe, T.W., and Whitman, R.V.: *Soil Mechanics*, John Wiley & Sons, New York, 553 pp., ISBN 0471511927, 1969.

1348 Larsen, M.C., and Torres-Sanchez, A.J.: Landslides triggered by hurricane Hugo in eastern Puerto Rico, September  
1349 1989. *Caribb. J. Sci.*, 28(3-4), 113–125, 1992.

1350 Larsen, M.C., and Simon, A.: A rainfall intensity-duration threshold for landslides in a humid-tropical environment,  
1351 *Puerto Rico*, *Geogr. Ann. A*, 75(1-2), 13-23, <https://doi.org/10.1080/04353676.1993.11880379>, 1993.

1352 Larsen, M.C., and Parks, J.E.: Map showing landslide susceptibility in the Comerio municipality, Puerto Rico, U.S.  
1353 *Geol. Surv. Open-File Rep.* 98-566, 1 plate, scale 1:20,000. <https://doi.org/10.3133/ofr98566>, 1998.

1354 Larsen, M.C., and Torres-Sanchez, A.J.: The frequency and distribution of recent landslides in three montane tropical  
1355 regions of Puerto Rico, *Geomorphology*, 24(4), 309–331, [https://doi.org/10.1016/S0169-555X\(98\)00023-3](https://doi.org/10.1016/S0169-555X(98)00023-3), 1998.

1356 Larsen M.C., Santiago, M., Jibson, R., and Questell, E.: Map showing susceptibility to rainfall-triggered landslides in  
1357 the municipality of Ponce, Puerto Rico, U.S. Geol. Surv. Scientific Investigations Map 2818, 1 plate, scale 1:30,000,  
1358 <https://doi.org/10.3133/sim2818>, 2004.

1359 Larsen, M.C.: Landslides and sediment budgets in four watersheds in eastern Puerto Rico, in: *Water Quality and*  
1360 *Landscape Processes of Four Watersheds in Eastern Puerto Rico*, edited by: Murphy, S.F., and Stallard, R.F., U.S.  
1361 *Geol. Surv. Prof. Paper* 1789, 153–178, <https://doi.org/10.3133/pp1789>, 2012.

1362 Lee, S., Ryu, J.-H., Min, K., and Won, J.-S.: Landslide susceptibility analysis using GIS and artificial neural network,  
1363 *Earth Surf. Proc. Land.*, 28(12), 1361–1376, <https://doi.org/10.1002/esp.593>, 2003.

1364 Lepore, C., Kamal, S.A., Shanahan, P., and Bras, R.L.: Rainfall-induced landslide susceptibility zonation of Puerto  
1365 Rico, *Environ. Earth Sci.*, 66, 1667–1681, <https://doi.org/10.1007/s12665-011-0976-1>, 2012.

1366 Lepore, C., Arnone, E., Noto, L.V., Sivandran, G., and Bras, R.L.: Physically based modeling of rainfall-triggered  
1367 landslides: A case study in the Luquillo forest, Puerto Rico, *Hydrol. Earth Syst. Sci.*, 17(9), 3371–3387,  
1368 <https://doi.org/10.5194/hess-17-3371-2013>, 2013.

1369 Likos, W.J., Wayllace, A., Godt, J., and Lu, N.: Modified direct shear apparatus for unsaturated sands at low suction  
1370 and stress, *Geotech. Test. J.*, 33(4), 286–298, <https://doi.org/10.1520/GTJ102927>, 2010.

1371 [Medina, V., Hürlimann, M., Guo, Z., Lloret, A., & Vaunat, J.: Fast physically based model for rainfall-induced](https://doi.org/10.1016/j.catena.2021.105213)  
1372 [landslide susceptibility assessment at regional scale, \*Catena\*, 201, 105213,](https://doi.org/10.1016/j.catena.2021.105213)  
1373 <https://doi.org/10.1016/j.catena.2021.105213>, 2021.

1374 [Mergili, M., Marchesini, I., Rossi, M., Guzzetti, F., and Fellin, W.: Spatially distributed three-dimensional slope](https://doi.org/10.1016/j.geomorph.2013.10.008)  
1375 [stability modelling in a raster GIS, \*Geomorph.\*, 206, 178-195, https://doi.org/10.1016/j.geomorph.2013.10.008](https://doi.org/10.1016/j.geomorph.2013.10.008), 2014a.

1376 [Mergili, M., Marchesini, I., Alvioli, M., Metz, M., Schneider-Muntau, B., Rossi, M., and Guzzetti, F.: A strategy for](https://doi.org/10.5194/gmd-7-2969-2014)  
1377 [GIS-based 3-D slope stability modelling over large areas, \*Geosci. Model Dev.\*, 7, 2969–2982,](https://doi.org/10.5194/gmd-7-2969-2014)  
1378 <https://doi.org/10.5194/gmd-7-2969-2014>, 2014b.

1379 Mergili, M., Schwarz, L., and Kociu, A.: Combining release and runout in statistical landslide susceptibility modeling,  
1380 *Landslides*, 16(11), 2151–2165, <https://doi.org/10.1007/s10346-019-01222-7>, 2019.

1381 [Metz, C.E.: Basic principles of ROC analysis, \*Seminars in Nuclear Medicine\*, 8\(4\), 283-298,](https://doi.org/10.1016/S0001-2998(78)80014-2)  
1382 [https://doi.org/10.1016/S0001-2998\(78\)80014-2](https://doi.org/10.1016/S0001-2998(78)80014-2), 1978.

1383 [Milledge, D.G., Bellugi, D., McKean, J.A., Densmore, A.L., and Dietrich, W.E.: \(2015\), A multi-dimensional stability](https://doi.org/10.1002/2014JF003135)  
1384 [model for predicting shallow landslide size and shape across landscapes, \*J. Geophys. Res. Earth Surf.\*,](https://doi.org/10.1002/2014JF003135)  
1385 <https://doi.org/10.1002/2014JF003135>, 2015.

1386 [Montgomery, D.R., and Dietrich, W.E.: A physically-based model for the topographic control on shallow landsliding,](https://doi.org/10.1029/93WR02979)  
1387 [Water Resour. Res.](https://doi.org/10.1029/93WR02979), 30, 1153–1171, <https://doi.org/10.1029/93WR02979>, 1994.

1388 Murphy, S.F., Stallard, R.F., Larsen, M.C., and Gould, W.A.: Physiography, geology, and land cover of four  
1389 watersheds in eastern Puerto Rico, U.S. Geol. Surv. Prof. Paper 1789-A, 24 pp., <https://doi.org/10.3133/pp1789A>,  
1390 2012.

1391 Monroe, W.H.: The karst landforms of Puerto Rico, U.S. Geol. Surv. Prof. Paper 899, 69 pp.,  
1392 <https://doi.org/10.3133/pp899>, 1976.

1393 Nicótina, L., Tarboton, D.G., Tesfa, T.K., and Rinaldo, A.: Hydrologic controls on equilibrium soil depths, *Water*  
1394 *Resour. Res.*, 47(4), W04517, <https://doi.org/10.1029/2010WR009538>, 2011.

1395 [Pack, R.T., Tarboton, D.G., and Goodwin, C.N.: The SINMAP approach to terrain stability mapping, in: \*International\*](https://digitalcommons.usu.edu/cee_facpub/2583/1998)  
1396 [Congress of the International Association of Engineering Geology and the Environment Proceedings, 8th, September](https://digitalcommons.usu.edu/cee_facpub/2583/1998)  
1397 [21–25, 1998, Vancouver, British Columbia, Canada, A. A. Balkema, Rotterdam, Netherlands.](https://digitalcommons.usu.edu/cee_facpub/2583/1998), 2, 1157–1165,  
1398 [https://digitalcommons.usu.edu/cee\\_facpub/2583/1998](https://digitalcommons.usu.edu/cee_facpub/2583/1998).

1399 [Palacio Cordoba, J., Mergili, M., and Aristizábal, E.: Probabilistic landslide susceptibility analysis in tropical](#)  
1400 [mountainous terrain using the physically based r.slope.stability model, Nat. Hazards Earth Syst. Sci., 20, 815–829,](#)  
1401 <https://doi.org/10.5194/nhess-20-815-2020>, 2020.

1402 Pando, M.A., Ruiz, M.E., and Larsen, M.C.: Rainfall-induced landslides in Puerto Rico: An overview, in: Slopes and  
1403 Retaining Structures Under Seismic and Static Conditions, edited by Gabr, M.A., Bowders, J.J., Elton, D., and  
1404 Zornberg, J.G., ASCE Geotech. SP., 140, 2911–2925, [https://doi.org/10.1061/40787\(166\)25](https://doi.org/10.1061/40787(166)25), 2005.

1405 Patton, N.R., Lohse, K.A., Godsey, S.E., Crosby, B.T., and Seyfried, M.S.: Predicting soil thickness on soil mantled  
1406 hillslopes, Nat. Commun., 9, 3329, <https://doi.org/10.1038/s41467-018-05743-y>, 2018.

1407 Pelletier, J.D., and Rasmussen, C.: Geomorphically based predictive mapping of soil thickness in upland watersheds,  
1408 Water Resour. Res., 45(9):W09417. <https://doi.org/10.1029/2008WR007319>, 2009.

1409 Perkins, J.P., Baxstrom, K.W., Einbund, M.M, and Schulz, W.H: Modified basal contact of the Tertiary Lares  
1410 Limestone in the vicinity of Utuado, Puerto Rico, USA, derived from USGS Open-File Report 98-038, U.S. Geol.  
1411 Surv. data release [data set], <https://doi.org/10.5066/P9NL9EZG>, 2022.

1412 Raia, S., Alvioli, M., Rossi, M., Baum, R.L., Godt, J.W., and Guzzetti F.: Improving predictive power of physically  
1413 based rainfall-induced shallow landslide models: A probabilistic approach, Geosci. Model Dev., 7(2), 495–514,  
1414 <https://doi.org/10.5194/gmd-7-495-2014>, 2014.

1415 Ramos-Scharrón, C.E., Arima, E.Y., Guidry, A., Ruffe, D., and Vest B.: Sediment mobilization by hurricane-driven  
1416 shallow landsliding in a wet subtropical watershed, J. Geophys. Res.-Earth, 126(5), e2020JF006054,  
1417 <https://doi.org/10.1029/2020JF006054>, 2021.

1418 Reid, M.E., Christian, S.B., Brien, D.L., and Henderson, S.T.: Scoops3D—Software to analyze 3D slope stability  
1419 throughout a digital landscape, U.S. Geol. Surv. Techniques and Methods 14-A1 [code], 218 pp.  
1420 <https://doi.org/10.3133/tm14A1>, 2015.

1421 Reid, M.E., Coe, J.A., and Brien, D.L.: Forecasting inundation from debris flows that grow volumetrically during  
1422 travel, with application to the Oregon coast range, USA, Geomorphology, 273, 396–411.  
1423 <https://doi.org/10.1016/j.geomorph.2016.07.039>, 2016.

1424 Roering, J.J.: How well can hillslope evolution models “explain” topography? Geol. Soc. Am. Bull., 120(9-10), 1248–  
1425 1262, <https://doi.org/10.1130/B26283.1>, 2008.

1426 [Rossi, G., Catani, F., Leoni, L., Segoni, S., and Tofani, V.: HIRESSS: a physically based slope stability simulator for](#)  
1427 [HPC applications, Nat. Hazards Earth Syst. Sci., 13, 151–166, doi:10.5194/nhess-13-151-2013, 2013.](#)

1428 Schulz, W.H., Jensen, E.K., Cerovski-Darriau, C.R., Baum, R.L., Thomas, M.A., and Coe, J.A.: Field observations of  
1429 landslides and related materials following Hurricane Maria, Puerto Rico, U.S. Geol. Surv. data release [data set],  
1430 <https://doi.org/10.5066/P9T9KZ6T>, 2023.

1431 [Segoni, S., Leoni, L., Benedetti, A. I., Catani, F., Righini, G., Falorni, G., Gabellani, S., Rudari, R., Silvestro, F., and](#)  
1432 [Rebora, N.: Towards a definition of a real-time forecasting network for rainfall induced shallow landslides, Nat.](#)  
1433 [Hazards Earth Syst. Sci., 9, 2119–2133, https://doi.org/10.5194/nhess-9-2119-2009, 2009.](#)

1434 Simon, A., Larsen, M.C., and Hupp, C.R.: The role of soil processes in determining mechanisms of slope failure and  
1435 hillslope development in a humid-tropical forest eastern Puerto Rico, *Geomorphology*, 3(3-4), 263–286,  
1436 [https://doi.org/10.1016/0169-555X\(90\)90007-D](https://doi.org/10.1016/0169-555X(90)90007-D), 1990.

1437 [Simoni, S., Zanotti, F., Bertoldi, G., and Rigon, R.: Modelling the probability of occurrence of shallow landslides and](#)  
1438 [channelized debris flows using GEOTop-FS, \*Hydrol. Processes\*, 22\(4\), 532–545, doi:10.1002/hyp.6886, 2008.](#)

1439 Smith, J.B., Thomas, M.A., Ashland, F., Michel, A.R., Wayllace, A., and Mirus, B.B.: Hillslope hydrologic  
1440 monitoring data following Hurricane María in 2017, Puerto Rico, July 2018 to June 2020, U.S. Geol. Surv. data release  
1441 [data set], <https://doi.org/10.5066/P9548YK2>, 2020.

1442 Soil Survey Staff: Soil Survey Geographic (SSURGO) Database for Puerto Rico, all regions. U.S. Department of  
1443 Agriculture Natural Resources Conservation Service [data set], <https://websoilsurvey.sc.egov.usda.gov/app/> (last  
1444 access: 10 August 2023), 2018.

1445 Sowers, G.F.: Landslides in weathered volcanics in Puerto Rico, in: *Proceedings of the Fourth Pan-American*  
1446 *Conference on Soil Mechanics and Foundation Engineering*, American Society of Civil Engineers, New York, 105–  
1447 115, 1971.

1448 Taggart, B.E., and Joyce, J.: Radiometrically dated marine terraces on northwestern Puerto Rico, in: *Transactions of*  
1449 *the 12th Caribbean Geological Conference*, St. Croix, U.S. Virgin Islands, August 7th-11th, 1989, Miami Geological  
1450 Society, South Miami, Florida, 248–258, 1991.

1451 Taylor, D.W.: *Fundamentals of Soil Mechanics*, John Wiley & Sons, New York, 700 pp., 1948.

1452 Thomas, M.A., and Cerovski-Darriau, C.: Infiltration data collected post-Hurricane María across landslide source area  
1453 materials, Puerto Rico, USA, U.S. Geol. Surv. data release [data set], <https://doi.org/10.5066/P9SCGVF7>, 2019.

1454 Tello, M.: Optimization of landslide susceptibility modeling: A Puerto Rico case study, Master of Science Thesis,  
1455 Colorado School of Mines, Golden, Colorado, <https://hdl.handle.net/11124/174137>, 2020.

1456 Terzaghi, K., Peck, R.B., and Mesri, G.: *Soil Mechanics in Engineering Practice*, 3rd ed. John Wiley & Sons: New  
1457 York, 549 pp., ISBN: 978-0-471-08658-1, 1996.

1458 [Tofani, V., Bicocchi, G., Rossi, G., Segoni, S., D’Ambrosio, M., Casagli, N., & Catani, F.: Soil characterization for](#)  
1459 [shallow landslides modeling: a case study in the Northern Apennines \(Central Italy\), \*Landslides\*, 14, 755-770,](#)  
1460 <https://doi.org/10.1007/s10346-017-0809-8>, 2017.

1461 Turnbull, W.J., and Hvorslev, M.J.: Special problems in slope stability, *Journal of the Soil Mechanics and Foundations*  
1462 *Division*, 93(SM4), 499–528, <https://doi.org/10.1061/JSFEAQ.0001004>, 1967.

1463 U.S. Geological Survey: 2015–2016 USGS Puerto Rico LiDAR (project PR\_PuertoRico\_2015) [data set], at  
1464 <https://apps.nationalmap.gov/lidar-explorer/#/> (last access: 10 August 2023), 2018.

1465 U.S. Geological Survey: 2018 USGS Puerto Rico – Virgin Islands LiDAR (project PR\_PRVI\_A\_2018),  
1466 <https://apps.nationalmap.gov/lidar-explorer/#/> (last access: 10 August 2023), 2020a.

1467 U.S. Geological Survey: 2018 USGS Puerto Rico – Virgin Islands LiDAR (project PR\_PRVI\_D\_2018),  
1468 <https://apps.nationalmap.gov/lidar-explorer/#/> (last access: 10 August 2023), 2020b.

1469 U.S. Geological Survey: 2018 USGS Puerto Rico – Virgin Islands LiDAR (project PR\_PRVI\_H\_2018),  
1470 <https://apps.nationalmap.gov/lidar-explorer/#/> (last access: 10 August 2023), 2020c.



471 [von Ruetze, J., Lehmann, P. Or, D.: Rainfall-triggered shallow landslides at catchment scale: Threshold mechanics-](#)  
472 [based modeling for abruptness and localization, \*Water Resour. Res.\*, 49, 6266–6285,](#)  
473 <https://doi.org/10.1002/wrcr.20418>, 2013.

474 [Wang, S., Zhang K., van Beek, L.P.H., Tian, X., Bogaard, T.A.: Physically-based landslide prediction over a large](#)  
475 [region: Scaling low-resolution hydrological model results for high-resolution slope stability assessment,](#)  
476 [Environmental Modelling & Software, 124, 104607, https://doi.org/10.1016/j.envsoft.2019.104607, 2020.](#)

477 [Woodard, J. B., Mirus, B. B., Wood, N. J., Allstadt, K. E., Leshchinsky, B. A., and Crawford, M. M.: Slope Unit](#)  
478 [Maker \(SUMak\): an efficient and parameter-free algorithm for delineating slope units to improve landslide modeling,](#)  
479 [Nat. Hazards Earth Syst. Sci., 24, 1–12, https://doi.org/10.5194/nhess-24-1-2024, 2024.](#)

480 [Wu, W., and Sidle, R.C.: A distributed slope stability model for steep forested hillslopes, \*Water Resour. Res.\*, 31,](#)  
481 [2097–2110, https://doi.org/10.1029/95WR01136](https://doi.org/10.1029/95WR01136), 1995.

482 [Xiao, T., Segoni, S., Liang, X., Yin, K., & Casagli, N.: Generating soil thickness maps by means of geomorphological-](#)  
483 [empirical approach and random forest algorithm in Wanzhou County, Three Gorges Reservoir, \*Geoscience Frontiers\*,](#)  
484 [14\(2\), 101514, https://doi.org/10.1016/j.gsf.2022.101514, 2023.](#)

485 [Yan, Q., Wainwright, H., Dafflon, B., Uhlemann, S., Steefel, C.I., Falco, N., Kwang, J. and Hubbard, S.S.: Hybrid](#)  
486 [data-model-based mapping of soil thickness in a mountainous watershed, \*Earth Surf. Dynam. Discuss.\*, 1–23,](#)  
487 [doi:10.5194/esurf-2020-110](https://doi.org/10.5194/esurf-2020-110), 2021.

1488 [Zicher, T., Rutzinger, M., Schneider-Muntau, B., Perzl, F., Leidinger, D., Formayer, H., and Geitner, C.: Sensitivity](#)  
1489 [analysis and calibration of a dynamic physically based slope stability model, \*Nat. Hazard. Earth Sys.\*, 17\(6\), 971–992.](#)  
1490 <https://doi.org/10.5194/nhess-17-971-2017>, 2017.

1491